UNIVERSITÄT BONN
Physikalisches Institut

Development and Characterization of Diamond and 3D-Silicon Pixel Detectors with ATLAS-Pixel Readout Electronics

von
Markus Mathes

Abstract: Hybrid pixel detectors are used for particle tracking in the innermost layers of current high energy experiments like ATLAS. After the proposed luminosity upgrade of the LHC, they will have to survive very high radiation fluences of up to 10^{16} particles per cm^2 per life time. New sensor concepts and materials are required, which promise to be more radiation tolerant than the currently used planar silicon sensors. Most prominent candidates are so-called 3D-silicon and single crystal or poly-crystalline diamond sensors. Using the ATLAS pixel electronics different detector prototypes with a pixel geometry of $400 \times 50\,\mu\mathrm{m}^2$ have been built. In particular three devices have been studied in detail: a 3D-silicon and a single crystal diamond detector with an active area of about $1\,\mathrm{cm}^2$ and a poly-crystalline diamond detector of the same size as a current ATLAS pixel detector module ($2 \times 6\,\mathrm{cm}^2$). To characterize the devices regarding their particle detection efficiency and spatial resolution, the charge collection inside a pixel cell as well as the charge sharing between adjacent pixels was studied using a high energy particle beam.

Post address:
Nussallee 12
53115 Bonn
Germany

BONN-IR-2008-15
Bonn University
December 2008
ISSN-0172-8741

UNIVERSITÄT BONN
Physikalisches Institut

Development and Characterization of Diamond and 3D-Silicon Pixel Detectors with ATLAS-Pixel Readout Electronics

von
Markus Mathes

Dieser Forschungsbericht wurde als Dissertation von der Mathematisch-Naturwissenschaftlichen Fakultät der Universität Bonn angenommen und ist auf dem Hochschulschriftenserver der ULB Bonn http://hss.ulb.uni-bonn.de/diss_online elektronisch publiziert.

Angenommen am: 18. Dezember 2008
Referent: Prof. Dr. N. Wermes
Korreferent: Prof. Dr. H. Schmieden

Contents

1 Introduction **1**

2 The Large Hadron Collider and the ATLAS Experiment **3**
2.1 The Large Hadron Collider (LHC) 3
2.2 The ATLAS Experiment 4

3 Operation Principles of Semiconductor Detectors **13**
3.1 Energy deposition by particles 13
3.2 Energy deposition by photons 17
3.3 Sensors principles 18
3.4 Basic characteristics of silicon and diamond sensors 23

4 Motivation for Pixel Detectors using New Materials **27**
4.1 Radiation damage 30
4.2 Radiation hard sensor designs 34

5 The ATLAS Pixel Modules **39**

6 The Testbeam Reference System **47**
6.1 Track reconstruction and alignment 48
6.2 The telescope modules 58

7 Characterization and Calibration of ATLAS Pixel Devices **65**
7.1 The TurboDAQ test system 65
7.2 Calibration and adjustment of the front-end chip 66
7.3 Measurements for sensor characterization 67

8 Diamond Pixel Sensors **73**
8.1 scCVD diamond single chip assembly 75
8.2 pCVD diamond module 85

9 3D-Silicon Pixel Sensors **95**
9.1 3D single chip assemblies 97

10 Summary **111**

1 Introduction

"The real voyage of discovery consists not in seeking new landscapes, but in having new eyes"

Marcel Proust, French novelist, essayist and critic (1871-1922)

Experiments where particles are brought to collision or are scattered of each other are used to explore the fundamental structure of matter, their properties and interactions. It began with the discovery of the nucleus by Rutherford in 1911 by measuring the directional distribution of α-particles scattered on a gold foil. Similar experiments at colliders lead to our present understanding of matter and its interactions, the "Standard Model" of particle physics. It says that everything around us is made of particles called quarks and leptons with four kinds of forces acting on them. The forces are gravity, the electromagnetic force, the strong force, which binds atomic nuclei together and the weak force, which causes nuclear reactions.

But there are open issues. The origin of mass is still a mystery. To explain it the theory has to be expanded by introducing the so called Higgs boson, which has not yet been discovered. There are more unanswered questions: Why is the weak force 10^{32} times stronger than gravity? Is it possible to derive all four forces from one principle? In addition, the recently confirmed mass of the neutrino is not explainable at all within the standard model. Hence, there must be physics beyond the standard model. It could be supersymmetry (SUSY) or string theory, but no evidences for either has been found until now.

To get answers new experiments like ATLAS at the Large Hadron Collider at CERN in Geneva have been prepared. They are now in the phase of going to operation. More than a decade of research, development and construction was needed to solve the technological challenges coming along with such a project. To extend our knowledge and test the present theories, colliders have to reach higher and higher energies as otherwise the physics of interest will not become accessible. At the origin of the collision, the primary vertex, extremely high temperatures and densities are obtained, such as might have occurred in the first moments after the Big Bang. Looking at the particles produced and the processes happening there is looking back at the early universe.

The processes one is hoping to observe are rare and will be buried below a vast amount of others, less interesting. To make the interesting ones still happen often enough in a reasonable amount of time, several collisions have to occur simultaneously and be repeated at high rate. Some of the created particles are stable, some live for a long time while others decay immediately. The particles living

long enough to travel a few 100 µm before decaying in a new cascade of particles are of special interest. By tracing back the trajectories of the decay products to these so-called second vertices, they can be tagged. Some decay channels of the Higgs boson and from SUSY-events leave signatures separable by tagging long lived particles, making tagging secondary vertices a powerful tool to select events of interest.

For the identification of the secondary vertices detectors with µm precision are needed. This precision can only be obtained if the detectors are placed as close as possible to the interaction point. For the current ATLAS detector this means as close as 5 cm. At this distance the equivalence of 10^{15} 1 MeV neutrons will cross each cm^2 of the detector during the lifetime of the experiment. For the planned upgrade to LHC the radiation dose will be even higher. It will increase by at least one order of magnitude. Thus another aspect, namely the radiation tolerance of the detector components and especially of the particle sensors comes into play.

At present silicon is the standard sensor material of choice. It is the best understood semiconductor material, quite cheap even if used for large areas and the available photolitographic processes allow to structure the sensors fine enough to reach the required resolution and granularity to individually identify the tracks without ambiguities. But at the mentioned radiation levels state of the art silicon sensors stop operating. The penetrating particles damage the crystalline structure and alter the materials properties. Research and development is needed to find sensor concepts surviving the conditions found at the planned experiments.

The topic of this thesis is to study two sensor concepts with respect to their applicability for a next generation pixel detector. The first one is using diamond, which is more radiation hard mainly because of its wider bandgap and stronger inter-atomic bonds. The other one is a silicon 3D detector, where the problems of radiation damaged silicon are reduced by a special design of the electrode geometry.

For an introduction to the context of LHC and ATLAS chapter 2 gives a technical overview of this experiment. Chapter 3 summarizes the principles of semiconductor sensors and the interaction processes responsible for the signal generation. To motivate the need for new sensor concepts, the challenges of the harsh radiation environment and its implications for the sensor are presented in chapter 4 together with an overview of the sensor material candidates. Chapter 5 introduces the ATLAS pixel assemblies and explains the details of the readout electronics as far as needed for the characterization of the new sensors concepts.

The characterization of the tested structures was carried out in a particle beam. The test system is introduced in chapter 6. The methods used to characterize the prototype devices in the lab and in the particle beam are summarized in chapter 7. The results of the characterization of the diamond devices is the topic of chapter 8, while the outcomes for the 3D-devices are discussed in chapter 9 correspondingly. Chapter 10 summarizes the obtained results and points out the most important aspects observed for the two detector concepts.

2 The Large Hadron Collider and the ATLAS Experiment

2.1 The Large Hadron Collider (LHC)

At the TeV energy range one expects to observe physics of fundamental interest. The constraints derived from theory and previous experiments show that the higgs boson, if it exists, must manifest itself at collider experiments in this energy range. But as the TeV energy range has not been explored before one also hopes to find evidences for new physics phenomena like supersymmetry as a new symmetry of nature or the appearance of extra space-time dimensions. The plans to make the TeV energy regime accessible in the laboratory with the Large Hadron Collider (LHC) started to take shape already in the beginning of the 1990s. Now, at the moment of writing the installation of the LHC has just finished and the LHC is entering the state of commissioning. The LHC reuses most of the existing underground structures and pre-accelerator stages available from its predecessor LEP. It is located in a circular tunnel of 27 km circumference, about 100 m below surface, crossing the border between Switzerland and France (fig. 2.1).

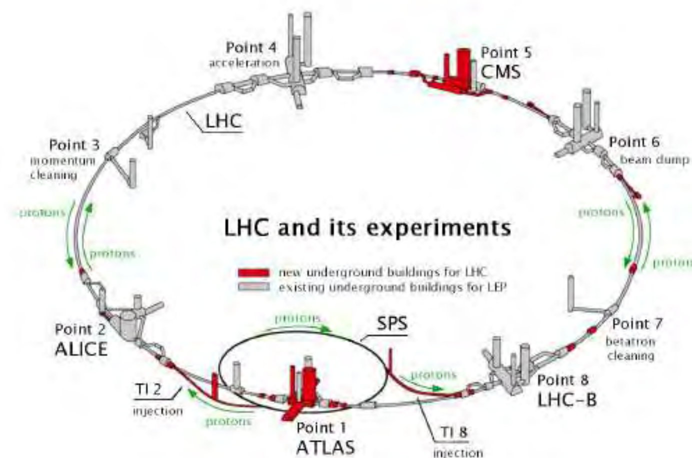

Figure 2.1: LHC and its four experiments ALICE, ATLAS, CMS and LHCb. The underground cavities shown in red are newly build, while the others are reused from the previous LEP experiments [1].

To reach particles energies in the TeV range LHC collides protons instead of the lighter electrons/positrons like it was the case at LEP. The use of protons, however,

bears the disadvantage that they are not elementary particles. Only the collisions of their constituents, the quarks and the gluons, are of fundamental interest to the scientists. On the other hand, the use of protons instead of electrons reduces the energy loss due to synchrotron radiation significantly. The protons are accelerated to an energy of 7 TeV in bunches of about 10^{11} particles each, spaced in time by 25 ns. Superconducting magnets of 8 T guide the beams around the accelerator ring. The magnets, as well as the RF acceleration cavities are operated at cryogenic temperatures of 4.5 K. The focusing magnets are operated at a lower temperature of 1.9 K to allow for higher magnetic fields. Two beams are counter-rotating in two separate vacuum pipes, but are brought into collision at the points of the four main experiments. The two experiments ATLAS and CMS are designed as general purpose experiments to be sensitive to physics in and beyond the standard model (SM). LHCb is specialized to address questions in CP-violation and ALICE is a dedicated experiment to study heavy ion collisions at high energies reaching the regime of a quark-gluon plasma. For the latter LHC is able to accelerate lead ions instead of protons to energies in the 1000 TeV range.

The first proton beams have just circulated in the LHC. In the beginning of 2009 the beam energy will be ramped up to its final value. Collisions at high energy are expected later in 2009 with primary results from the experiments soon after. For the first years the luminosity is expected to reach $10^{-33}\,\mathrm{cm}^{-2}\mathrm{s}^{-1}$ and to increase after three years to $10^{-34}\,\mathrm{cm}^{-2}\mathrm{s}^{-1}$, equivalent to an integrated luminosity of $100\,\mathrm{fb}^{-1}$ per year [1].

2.2 The ATLAS Experiment

ATLAS is the abbreviation of "A Toriodial Lhc ApparatuS". The detector is designed to detect and survey the new phenomena that one hopes to observe at the TeV scale. To identify the most promising ones the design is driven by the following demands [2][3]:

- Precise momentum and energy measurements of all particles, with almost full angular coverage is crucial to indirectly detect the presence of weakly interacting particles.
- Identifying the type of a particle. Especially to distinguish photons, leptons and hadrons/jets, is essential to find the channels of interest. For this also the identification of secondary vertices is important, requiring high resolution tracking possibilities.
- To cope with the generated datarate a highly selective trigger system is needed to reject background, while selecting signals of interest.
- The vast amount of particles produced by LHC collisions require detector systems functioning at the given radiation level, particle density and repetition rate.

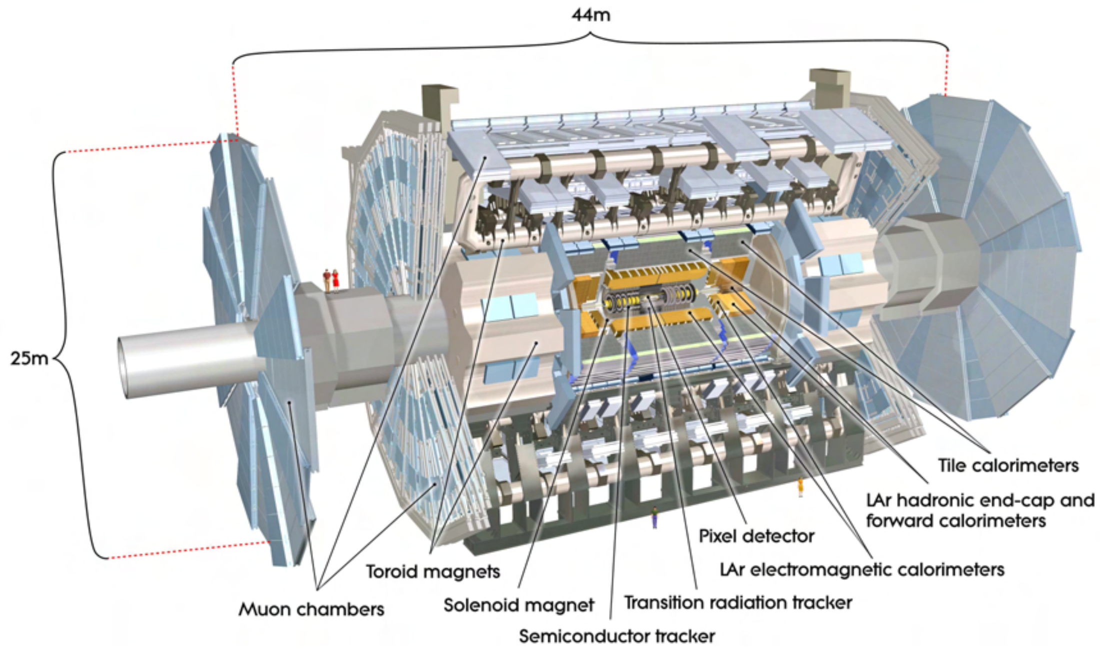

Figure 2.2: Overview of the ATLAS detector showing the different subdetector systems [3].

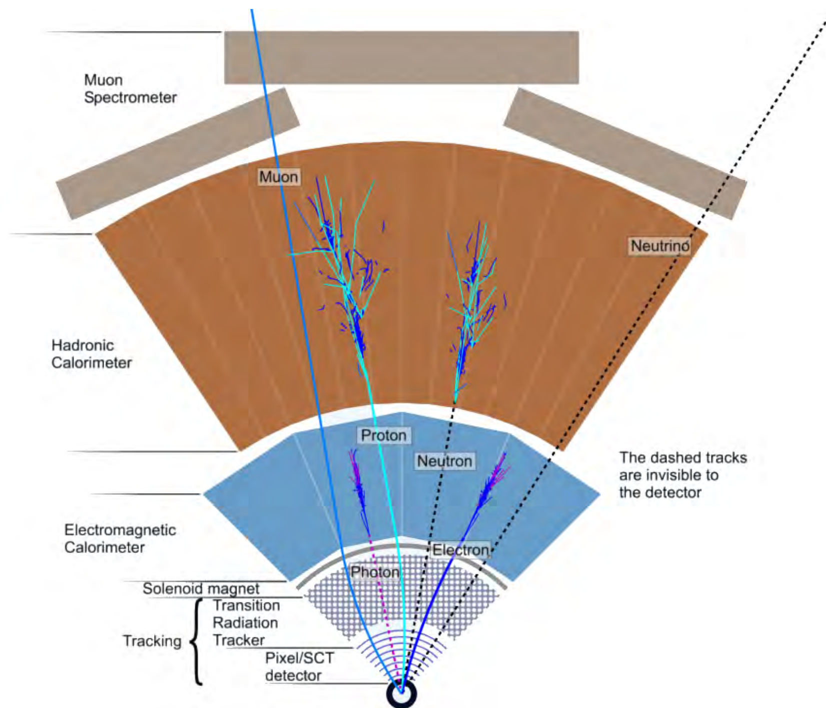

Figure 2.3: Cross section through the ATLAS detector. The signatures created in the subdetectors by different kinds of particles are shown [1].

The overall layout of ATLAS is shown in fig. 2.2. The detector is composed of subdetectors, each specialized to one main aspect of the requirements. The inner detectors are mainly specialized to determine the momenta of the particles while the outer are used to measure the energy. The subdetector systems are arranged in a Matrjoschka style, enclosing each time the previous ones. The basic design is a composition of a barrel structure to cover the central region and discs to both sides in forward and backward direction. In fig. 2.3 the tasks performed by the different subdetector systems are illustrated. The next sections describe the detector starting from the interaction point on outwards. Further information can be found in [3].

2.2.1 The Inner Detector

The purpose of the inner detector is to individually trace the charged particles created, identify their origin and measure their momenta. In addition it helps in the particle identification. The particles are tracked by detecting their interaction with material at discrete points. The momentum is revealed by determining the track curvature in a magnetic field. For this reason the whole inner detector is enclosed in a solenoidal magnetic field of 2T. The inner detector itself is split in three separate and independent subdetectors, namely the pixel detector, the silicon strip tracker (SCT) and the transition radiation tracker (TRT) (fig. 2.4).

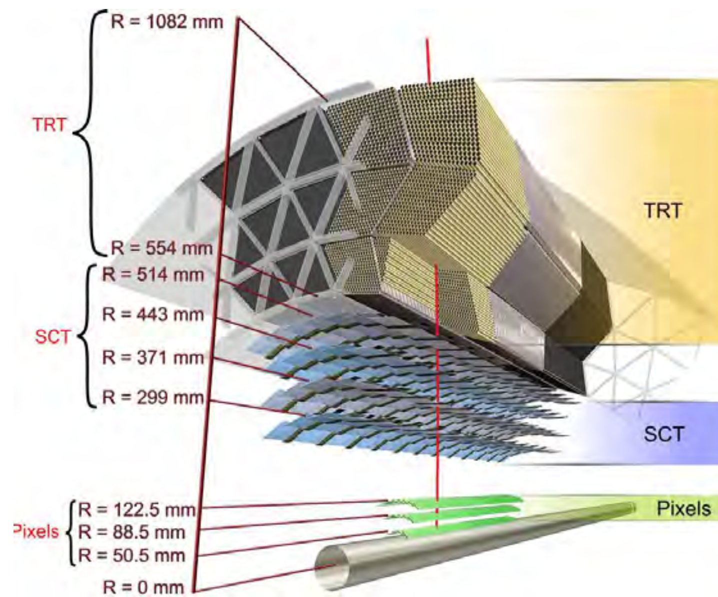

Figure 2.4: The sensors and structural elements traversed by a charged track in the barrel inner detector. The track traverses successively the beryllium beam-pipe, the three cylindrical silicon pixel layers, the four cylindrical double layers of the barrel silicon microstrip sensors (SCT) and approximately 36 axial straws contained in the barrel transition radiation tracker (TRT) modules within their support structure [3].

Pixel Detector

The choice of a silicon pixel detector as the innermost tracking layer is driven by the high track occupancy close to the interaction point. The active elements are sensors made of 250 µm thick, radiation tolerant silicon which is structured in pixels of $50 \times 400\,\mu m^2$. The pixel detector has a position resolution better than 15 µm in r/ϕ and better than 120 µm in z-direction. It substantially contributes to the pattern recognition in the track fitting algorithms, as it delivers accurate trackpoint information in all three spatial directions. This is essential for the identification of secondary vertices. It is composed of three central layers and three disks on each end-cap (fig. 2.5). The pixel detector has over 80 million readout channels, which is about 50% of the total number of readout channels in the whole experiment.

As this work discusses different sensor upgrade possibilities, the structure of the pixel detector is presented in a bit more detail than for the other detector subsystems. More details of the layout and on the implementation can be found in [4]. The ATLAS pixel detector in its global support frame is shown in the drawing of figure 2.5. In the central region the three barrel layers cover the interaction point at radii of 50.5 , 88.5 and 122.5 mm. The position of the first layer is given by the constraints from the beam pipe dimensions as well as by the radiation level which the sensors are able to withstand. The layers cover the beam axis over a region of $\pm 400mm$. In terms of *pseudo rapidity*[1] the barrel layers cover the region of $|\eta| < 1.9$. Three additional disc layers ensure at least three detector layers to be hit up to an $|\eta|$ value of 2.5. The discs are located in beam direction at ±49.5 , ±58 and ±65 cm.

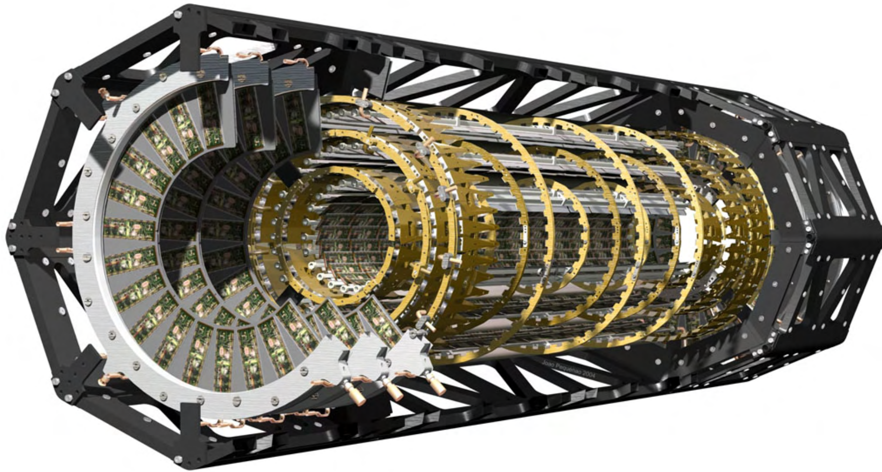

Figure 2.5: Drawing of the pixel detector in its global support frame [5].

[1] The pseudo rapidity η is defined by the angle θ between the beam axis and the particle trajectory as η being equal to $-\ln(\tan(\theta/2))$. A θ of 90° corresponds to $\eta = 0$. A θ of 0° to $\eta = \infty$.

The sensitive area is made up from detector modules of about $2 \times 6\,\mathrm{cm}^2$. To fully cover the layers without dead regions in between the modules are mounted with an overlap like the tiles on a roof. This kind of arrangement is illustrated for the barrel layers in fig. 2.6 and fig. 2.7. The layout of the disc layers is shown in fig. 2.8.

The material crossed under normal incidence by a particle in the barrel region corresponds to about 11% of a *radiation length*[2] X_0. Each of the three layers contribute with about 3% X_0 (1% X_0 detector modules, 0.5% X_0 cabling and 1.5% X_0 module support and cooling). The remaining 2% X_0 are attributed to the global support and subdetector encapsulation [3].

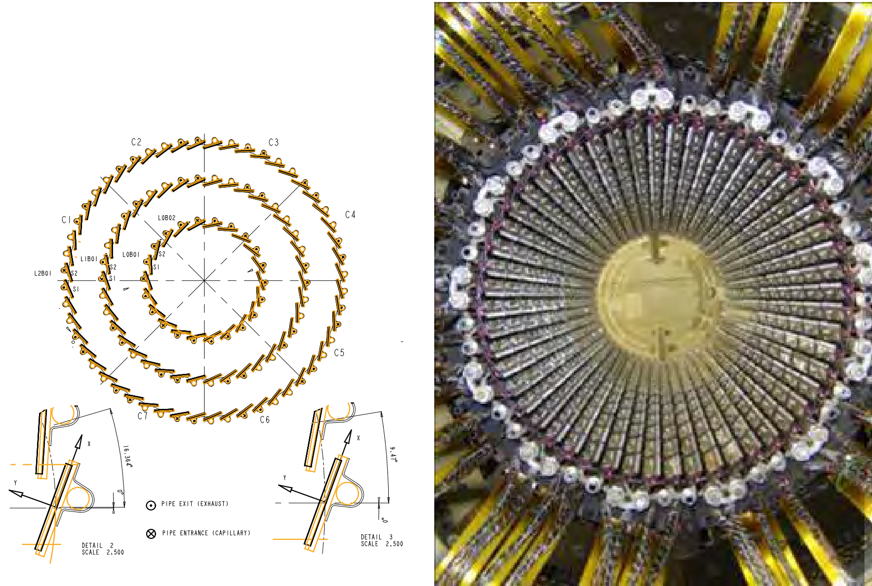

Figure 2.6: Drawing of the stave-arrangement in the barrel and a photograph of the fully equipped innermost barrel layer.

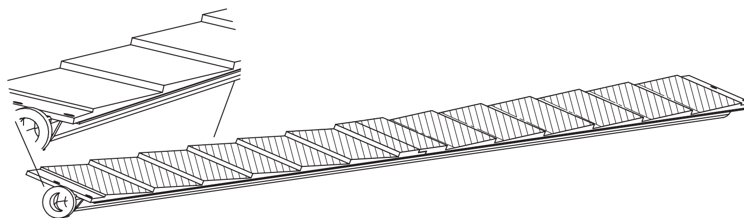

Figure 2.7: Illustration of a barrel stave showing the inclined positioning of the modules to achieve a shingled overlap (not to scale, horizontal direction jolted by roughly a factor of eight).

[2]The *radiation length* is a characteristic related to the energy loss and the deflection of high energy, electromagnetic-interacting particles in matter. See also chap. 3.1

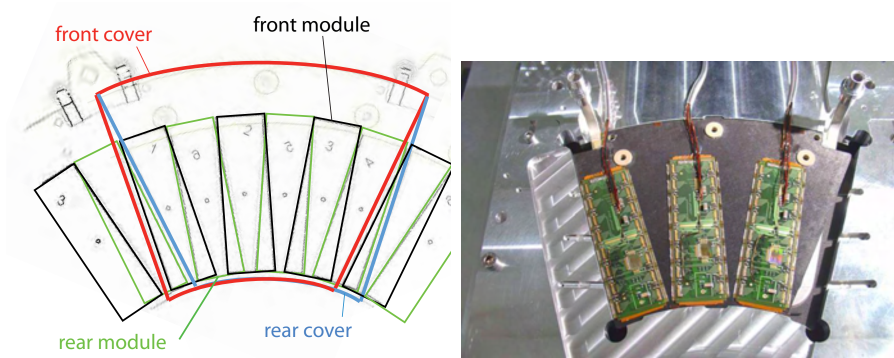

Figure 2.8: Drawing and photograph of an end-cap sector of the pixel detector, illustrating the module mounting positions.

Silicon Strip Tracker (SCT)

The design of the Silicon Strip Tracker (SCT) is similar to the pixel detector. It contributes with four barrel layers and nine discs on each side to the track reconstruction. Instead of pixel sensors the basic units are single sided p-in-n silicon strip sensors of 300 µm thickness, $6 \times 6\,\text{cm}^2$ in size. The strip pitch of the barrel is 80 µm and varies for the discs between 57 µm at the inside to 94 µm at the outside. Strip sensors show no position sensitivity along the strip direction. Therefore, the sensors are glued together with their strips rotated by a small stereo-angle of 40 mrad to obtain position information in this direction . The position resolution achieved in r/ϕ is about 16 µm and in z-direction around 850 µm [3].

Transition Radiation Tracker (TRT)

The Transition Radiation Tracker combines a straw tube tracker with electron/positron identification by using transition radiation. The barrel is made from axial oriented straws, while the discs contain radial straws. The gap between the straws is filled with synthetic fibers or foil-stacks to release transition radiation at every air to material transition. This effect is mainly relevant for highly relativistic electrons and positrons. The detection of these photons in addition to a track is used to distinguish $e^{\pm}$ from other particles such as π-mesons. In total 370000 tubes are arranged in the active volume and contribute with 36 points per particle on average to the track reconstruction. Depending on their position, the straw tubes have different lengths between 40 cm and 150 cm. They are filled with a Xe (70%)-CO_2 (27%)-O_2(3%)-gas mixture. A single tube has a radius of 4 mm with a 30 μm wire in the center. The distance of a particle to this wire can be determined with a precision of 170 μm. The position along the wire direction is not obtained.

2.2.2 The Calorimeters

The calorimeters used in ATLAS measure the energy of the particles by alternately absorbing energy and sampling the shape of the resulting particle shower. Furthermore the calorimeter is split in two subdetectors. The electromagnetic calorimeter, where energy from the particles is absorbed mainly by electromagnetic interaction and the hadronic calorimeter, where the remaining particles lose the energy in collisions with the nuclei of the absorber material. While the first mainly stops all the electrons and photons, the second stops the remaining hadrons. Only muons and weakly interacting particles like neutrinos are able to pass the calorimeters.

The electromagnetic calorimeter uses lead and stainless steel absorbers. Liquid argon (LAr) is used to sample the shape of the shower. Even if liquid, argon acts like a dense gas and the charge carriers produced by ionization due to the shower particles are used for the readout. Argon as noble gas is used to cope with the expected radiation damage as it does not create radicals and it allows to remove residues of nuclear reactions with reasonable effort. The whole electromagnetic calorimeter is embedded in an cryostat to keep the argon liquid. Special in the design is the accordion (zigzag) like structure. This allows readout at the edges, while ensuring enough absorber/sample transitions in all directions. The relative energy resolution is in the order of $10\%/\sqrt{E}$ and the location of the energy deposit is determined with an accuracy of roughly 0.025 radians for both solid angles [3].

The hadron calorimeter is lined up after the electromagnetic one. As energy-absorbing material lead is used to stop the hadrons while in the forward regions copper/tungsten is used. The sampling of the energy deposits in the barrel region is done with scintillator tiles while liquid argon is used for the forward regions. The relative energy resolution is about $50\%/\sqrt{E} + 3\%$ [3].

2.2.3 The Muon System

Muons are basically the only charged particles traversing the calorimeters. The clear, distinguishable signature of the muons enormously helps in the selection of events of interest and from special value for the discovery of new physics. The muon momentum and energy is determined by measuring its deflection in the magnetic field. For this, the track points of a muon are detected with a precision of about $80\mu m$.

The muon system is the largest subdetector. It builds the outer shell of ATLAS and dominates the overall picture by the size of its magnet system. The toroidal magnetic field is produced by eight gigantic air-core superconducting barrel loops and two separate end-cap magnets. The muons are detected in the barrel section by monitored drift tubes (MTDs). In the high occupancy forward directions cathode strip chambers (CSCs) are used. To make the muon signal available during the readout decision (triggering), parts of the system are optimized for fast readout. These parts use resistive plate chambers (RPCs) and thin gap chambers (TGCs) in the forwards regions.

2.2.4 The Trigger System

The 20 inelastic proton-proton collisions occurring on average per bunch crossing produce around 1.5MB of information in the detector. Since this is happening with a repetition rate of 40 MHz, the amount of data is by far too high to be permanently stored. It has to be reduced by a highly selective trigger system.

The detector is designed to temporarily cache all event information for 2.5 µs inside the subdetector systems. To make a decision fast enough, the first preselection decision is fully implemented in hardware. It uses parts of the calorimeters and the muon system to search for high transverse-momentum muons, electrons, photons, jets, and τ-leptons decaying into hadrons, as well as large missing and total transverse energy. The first level trigger (LVL1) reduces the readout rate of the full detector to 75 kHz.

The rate of accepted events is further reduced to about 1 kHz by a second trigger stage. The second level trigger (LVL2) is a package of highly optimized software algorithms running on a processor farm. For the refinement of the trigger decision the full detector information is available.

The last stage, the event filter (EF), does a more sophisticated analysis of the data and decides whether an event gets permanently stored or not. The software runs highly parallelized on a computer cluster to fall this decision within four seconds. The final rate of events to be stored permanently is about 100 Hz, corresponding to a datastream of several hundred megabytes per second, which equals three petabytes per year.

3 Operation Principles of Semiconductor Detectors

Particles and radiation are detected through their interaction with matter. The interaction processes differ for photons, charged particles and neutral particles. For the signal generation in semiconductor detectors at first order only interactions resulting in free charge carriers are of relevance. The free charge carriers in the sensor produce a current pulse which can be processed with the subsequent electronics.

3.1 Energy deposition by particles

High energetic charged particles passing through matter lose energy by many low energy transfers during interactions with the atoms of the material. The mean energy loss per unit length of a particle is described quite accurately by two characteristic quantities: the density of the material and the fraction of the particles momentum and mass, usually written as $\beta\gamma = p/mc$.[1] In fig. 3.1 the average energy loss is illustrated.

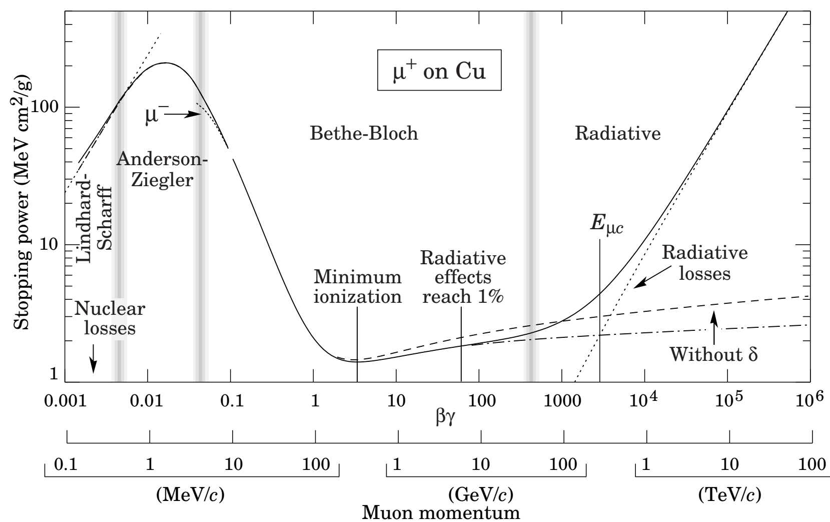

Figure 3.1: Stopping power of a μ in copper as a function of $\beta\gamma$. It is illustrating the functional behavior of energy loss of ionizing particles in matter [6].

[1] see tab. 3.1 for a definition of the variables

For particles below $\beta\gamma$ of 500, the energy loss is dominated by ionization. In the $\beta\gamma$ range of 0.1 to 500, the energy loss of a (heavy) charged particle is described by the Bethe-Bloch formula [6]:

$$-\left\langle \frac{dE}{dx} \right\rangle_{ion} = Kz^2 \frac{Z}{A} \frac{1}{\beta^2} \left[\frac{1}{2} \ln \frac{2m_e c^2 \beta^2 \gamma^2 T_{max}}{I^2} - \beta^2 - \frac{\delta(\beta\gamma)}{2} \right], \tag{3.1}$$

Particles produced in high energy physics experiments usually have a $\beta\gamma$ value in this region, especially the heavier particles like μ, π, p and K. A particle having the minimum value $\langle dE/dx \rangle_{min}$ in the curve in fig. 3.1 is called a minimum ionizing particle (MIP). It deposits in reasonable approximation $1.5 MeV cm^2/g$, nearly independent of the absorber material. A MIP can be considered producing the worst case signal amplitude, as it has the lowest possible energy deposit. The increase in energy loss in the material beyond this minimum is relatively small over the range relevant for particle physics, rendering the term MIP a good approximation for a wide range of particle momenta. Hence, the energy deposit by a MIP is often used to quantify the detector response.

The mean energy deposition of a particle passing a sample of finite thickness can be calculated using the formula given above. To obtain the energy-deposition spectra, however, statistical fluctuations have to be taken into account. Their origin can be separated into the fluctuations of the number of collisions experienced by a particle, which basically follows a Poisson statistic [7], and the fluctuations in the particular energy loss of a single interaction. Concerning solids, predominantly the energy transfers to individual electrons and to collective excitations (plasmons, etc.) have to be considered. While the latter are material dependent, the former

v	velocity of incident particle
z	charge of incident particle
M	mass of incident particle
E	energy of incident particle (MeV)
β	v/c, where c is the speed of light
Z	atomic number of traversed material
A	atomic mass of traversed material
u	atomic mass unit
ρ	density of traversed material
r_e	$= e^2/(4\pi\epsilon_0 m_e c^2)$, classical electron radius
K	$= 4\pi N_A r_e^2 m_e c^2$
m_e	rest mass of electron
I	Bethe's characteristic atomic energy (average ionization energy of material)
T_{max}	maximum kinetic energy imparted to a free electron in a single collission
$\delta(\beta\gamma)$	density effect correction to ionization energy loss
γ_E	$0.577\ldots$ Euler's constant

Table 3.1: Summary of variables used in the equations.

are for large momentum transfers in good approximation described by Rutherford scattering.

The first derivation of an energy-loss distribution or straggling function, as commonly referred to, was carried out for a thin detector by Landau [8]. An illustration of a Landau shaped distribution is shown in fig. 3.2. The Landau distribution can best be characterized by its most probable value of energy loss (Δ_p) and its full width at half maximum (w). To obtain accurate predictions for this characteristics one has to consider the atomic properties of the certain materials as well as the thickness of the sensor more seriously [9, 7]. For thin sensors the distribution becomes significantly wider and for thick sensors the shape of the distribution converges against a Gaussian. The most probable energy loss (MPV) and the FWHM are well measurable quantities in an experiment, even if for the latter one has to consider the noise of the measurement system. Contrary the mean of the energy loss is usually ill defined. The events that cause the high energy tail are rare and make the mean of an experimental distribution sensitive to statistical fluctuations, background as well as the considered energy range. Especially knock-on-electrons (δ-electrons) add up to this tail. These δ-electrons are electrons knocked out of an atom by the incident particle and which interact as particles of their own with the sensor.

An accurate description of the energy deposition in silicon was carried out by Bichsel [7]. He considered the material dependence in the momentum transfers as well as the number of collisions affected by the thickness of the sensor. Figure 3.2 shows the effect of the sensor thickness on the most probable energy deposition Δ_p and the full width at half maximum w of the distribution. While per unit length

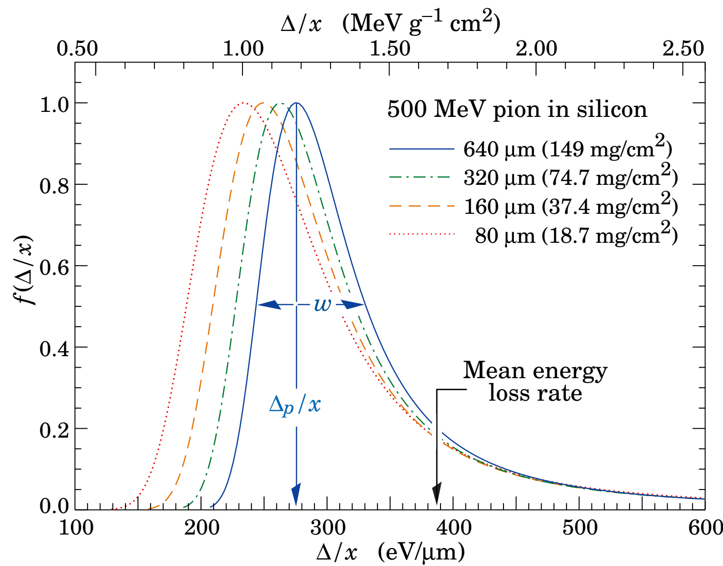

Figure 3.2: Straggling functions in silicon for 500 MeV pions, normalized to unity at the most probable value Δ_p/x. The width w is the full width at half maximum [10].

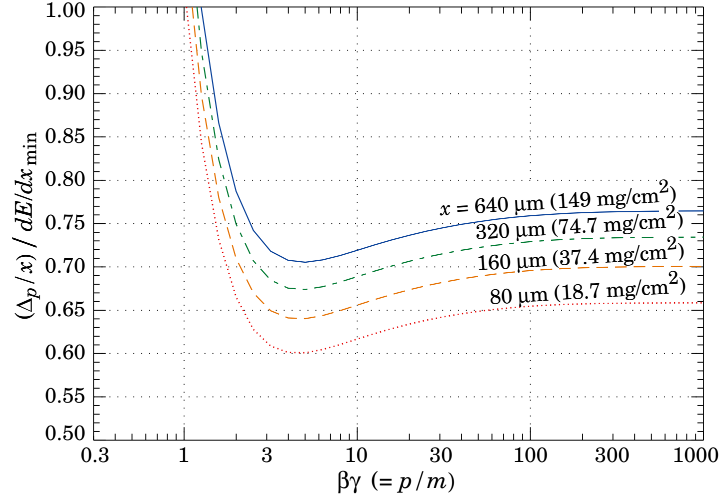

Figure 3.3: Most probable energy loss in silicon, scaled to the mean loss of a mimimum ionizing particle, 388 eV/µm (1.66 $\mathrm{MeVg^{-1}cm^{2}}$) [10].

the mean energy loss stays constant, the most probable energy loss for thicker sensors moves to higher values while in parallel the FWHM is reduced. This behavior is a consequence of the underlying statistics on the number of energy transfers. As result, the ratio Δ_p/w depends on the sensor thickness. Note, that for $\beta\gamma > 4$ the energy deposit by ionization rises due to relativistic effects. The MPV and FWHM scale accordingly. In solids the increase from the MIP values to the values for particles with $\beta\gamma$ of 100 can be larger than 10%. Figure 3.3 shows this dependence of the most probable value on the particle energy as well as on the sensor thickness. The values are shown for silicon and scaled to the mean energy deposit of a MIP. For particles above a $\beta\gamma$ of 100, the deviations with $\beta\gamma$ are less than 1 %. Good approximations for a silicon sensor with its thickness d given in μm are [7]:

$$\Delta_{p,Si}(eV) = d \cdot (190 + 16.3 \cdot \ln(d)), \ 110 < d < 3000 \tag{3.2}$$

$$w_{Si}(eV) = d \cdot (259.6 - 28.4 \cdot \ln(d)), \ 30 < d < 260 \tag{3.3}$$

$$= 71.3 \cdot d \cdot \left(1 + 39.4 \cdot t^{-0.8}\right), \ 260 < d < 3000 \tag{3.4}$$

The energy loss of particles above a $\beta\gamma$ of 500 is dominated by interactions with the Coulomb field of the nuclei. This corresponds to electrons with an energy above $250 MeV$ and to muons above $50 GeV$. For heavier particles this $\beta\gamma$ regime is usually not reached in present experiments. Concerning energy loss, the generation of bremsstrahlung is the most important. The energy loss is approximately given by:

$$-\left\langle \frac{dE}{dx} \right\rangle_{brems} = E \, \frac{Z\,(Z+1)}{A} \ln \frac{287}{Z^{1/2}} \frac{\rho}{716.4\,\mathrm{gcm^{-2}}} =: \frac{E}{X_0} \tag{3.5}$$

The contribution of the bremsstrahlung photons to the energy deposit in the sensor is negligible, as they most likely will not be absorbed again within the thickness of a low Z semiconductor sensor. Equation 3.5 also defines the material property *radiation length* X_0, which appears also in formula dealing with multiple scattering and pair-production.

3.2 Energy deposition by photons

The difference between photons and charged particles passing through matter is, that a beam of photons is mainly not degraded in energy, but attenuated in intensity.

$$I = I_0 e^{-\mu x}, \tag{3.6}$$

where x is the thickness of the sensor and μ the attenuation coefficient. The attenuation has different origins and the coefficient μ can be expressed by the cross sections σ of the different interactions: [2]

$$\mu = \mu_{photo} + \mu_{compton} + \mu_{pair} = \frac{\rho}{uA}\left(\sigma_{photo} + \sigma_{compton} + \sigma_{pair}\right) \tag{3.7}$$

The cross sections of the individual interactions depend strongly on the material and the photon energy and are shown in fig. 3.4 for the cases of silicon and carbon.

[2] see Table 3.1 for definition of variables

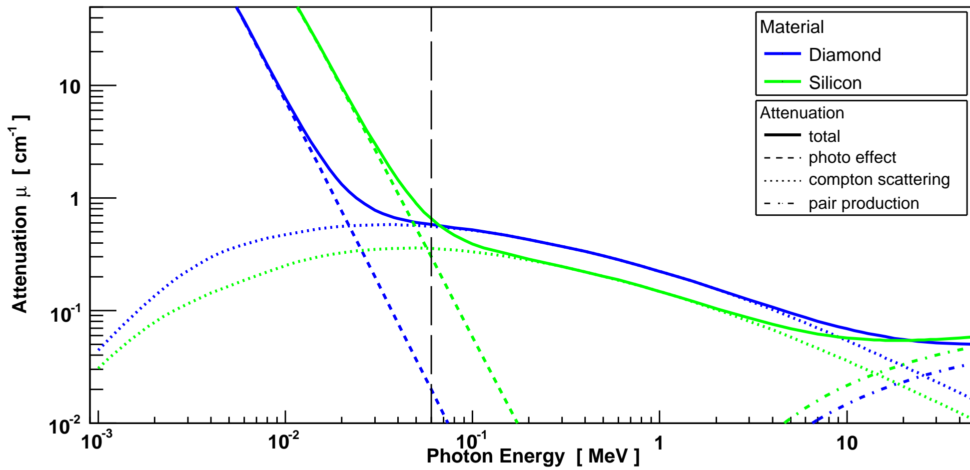

Figure 3.4: Attenuation coefficients for silicon and diamond [11]. The photon energy marked with the dashed line is equivalent to the mean energy loss from a MIP in a 200μm silicon sensor (60 keV). While for silicon at this energy the photo effect is as likely as Compton scattering, the photo effect in diamond is suppressed by one order of magnitude.

For photon energies up to several 10 keV, the dominant interaction is the photo effect. The cross section increases with Z to the power of 4 to 5, depending strongly on the photon energy. The photon is absorbed in the material and its energy fully transferred to an electron of an atom. For photon energies close to the band gap (eV), this directly creates an e/h-pairby rising the electron from the valence to the conduction band. For higher energies first a free electron is created which subsequently generates e/h-pairsby further interaction as described in the previous chapter. Usually the electron's energy is low enough to get full absorption again inside the sensor. By the photo effect, the discrete spectrum of a radioactive source is translated into a discrete number of generated e/h-pairs. This is extremely useful for calibration purposes and tests in the laboratory. By choosing the right source the most probable charge deposit from a MIP can be emulated (see also chapter 7.3).

Second important is Compton scattering. In the inelastic scattering process the photon transfers part of its energy to an electron while getting deflected itself. This deflection causes the attenuation in beam direction. The possible energy transfer is continuous. It starts with zero and has a sharp maximum at the so called Compton edge. The maximum transferable energy, which is also the most likely one, is given by:

$$E_{e,max} = \frac{(h\nu)^2}{m_e c^2 + h\nu} \tag{3.8}$$

As the energy transfer is continuous also the number of e/h-pairs generated from a photon of fixed energy is varying. Photon energies for which Compton scattering is dominating are therefore not that useful for testing purposes as the ones dominated by the photo effect.

The conversion of a photon into a free electron-positron pair is possible above a threshold of two times the electron mass (~ 1 MeV). For reasons of momentum conservation this is only allowed to happen in presence of either a nucleus or electron. This process fully dominates the photon absorption at high energies.

3.3 Sensors principles

In the following the principles and equations needed to understand the basic properties of a semiconductor sensors are compiled. Figure 3.5 shows the principle of a semiconductor sensor. The traversing particle creates e/h-pairs which are separated in an electric field and induce the signal current at the readout electrodes. Beside to the rise of electrons from the valence to the conduction band (e/h-pairs), the traversing particle spends energy to the excitation of lattice vibrations (phonons). Thus the average energy deposition needed to generate an e/h-pair is higher as the bandgap energy alone. As a rule of thumb it is given by twice the bandgap plus 1.5 eV [12]. Exact values are given in tab. 3.2.

In the case of a space charge free, intrinsic semiconductor the field inside the

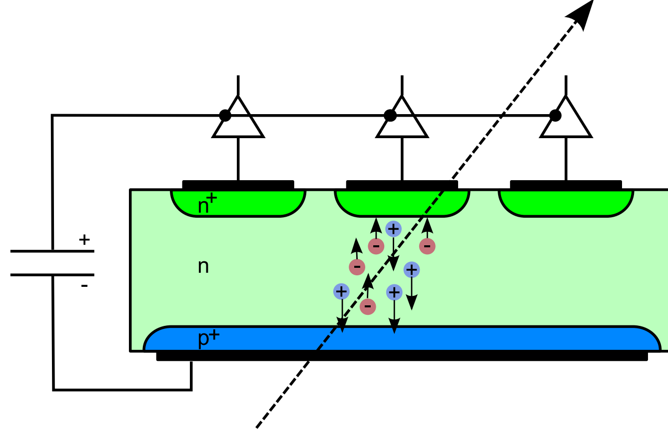

Figure 3.5: Schematic cross section of a semiconductor sensor. The passing particle creates free charge carriers in the bulk which get separated in the electric field produced by a bias voltage applied across the contact electrodes placed on either sides of the bulk. The motion and separation of the charge carriers induce a signal on the readout electrodes.

sensor is equal to a parallel plate capacitor and constant over the bulk:

$$E(x) = \frac{U_{bias}}{d} \tag{3.9}$$

Beside the signal carriers also thermal charge carriers are generated in the material. Their number is proportional to [13]:

$$n \sim T^{\frac{3}{2}} e^{-\frac{E_g}{2k_b T}} \tag{3.10}$$

This exponential behavior makes their number negligible for undoped high bandgap semiconductors like diamond and sensors operated at cryogenic temperatures. In the case of typical semiconductors like Si, Ge or GaAs the carriers of thermal origin dominate at room temperature over the carries produced by the incident particle. The situation can be changed by the use of a reverse biased pn-junction. In the depletion region of the junction all charge carriers are swept away and the continuously reproduced thermal carriers are few.

From the depletion results a space charge in the bulk which alters the electric field. In case of exact full depletion it is given by [14]:

$$E(x) = \frac{2U_{bias}}{d^2} \cdot (x - d) \tag{3.11}$$

To allow the depletion zone to extend over the full bulk width a combination of a lowly doped bulk and a highly doped contact is required. The voltage needed to deplete over the entire sensor thickness depends quadratically on the thickness d and linearly on the effective doping concentration N_{eff} of the bulk [14]:

$$U_{dep} \approx \frac{e}{2\varepsilon} N_{eff}\, d^2, \tag{3.12}$$

In the case of biasing the sensor with a voltage above U_{dep} the excess voltage adds up as constant field as from eq. 3.9. At lower biasing the sensor is only partial depleted and the charge collection is limited to the depleted fraction of the sensor. In the undeleted part no field is present to separate the charge carriers. As a consequence they will recombine and are lost for signal generation. To have a readily measurable quantity for the doping concentration of the material, it is commonly expressed in terms of resistivity [14]

$$\rho = \frac{1}{\mu e N_{eff}}, \tag{3.13}$$

where μ is the carrier mobility.

The mobility μ is material dependent and usually differs for electrons and holes. Together with the electric field in the sensor it describes the movement of the charge carriers:

$$\vec{v}(x) = \mu \vec{E}(x) \tag{3.14}$$

Beside the movement originating from the electric field the charge carriers also accomplish a thermally driven random-walk on their way through the sensor. The lateral diffusion acting on the charge carriers during their way to the electrodes results in a Gaussian shape profile with a width σ of [13]

$$\sigma = \sqrt{Dt}, \tag{3.15}$$

where t is the time during which the diffusion occurs. In the case of thermal equilibrium the diffusion constant D is directly coupled to the mobility by Einsteins relation [13]:

$$D = \frac{k_b T}{e} \mu \tag{3.16}$$

The signal current finally induced at an electrode by the movement of the charge carriers is given by Ramo's theorem [16]:

$$i_{ind}(t) = -nq\vec{v}(t) \cdot \vec{E}_w, \tag{3.17}$$

where n is the number of contributing charge carriers and q and $\vec{v}$ the carriers charge and velocity. The weighting field $\vec{E}_w$ describes the coupling of the carrier movement to the respective electrode taking into account the electrode geometry and the charge carrier travel distance. Figure 3.6 illustrates the signal formation in a segmented sensor. The total charge measured on an electrode corresponds to the induced current integrated over the carrier traveling time.

The shape of the weighting field has especially consequences for segmented sensors. The weighting field lines concentrate near the electrodes and most of the signal is induced in the charge drift close to the electrode. For the e/h-pairs created by radiation this implies that the charge carriers drifting towards the backplane contribute less significantly to the signal. If the charge carriers get stopped (trapping, recombination, underdepletion, etc.) before reaching the region close

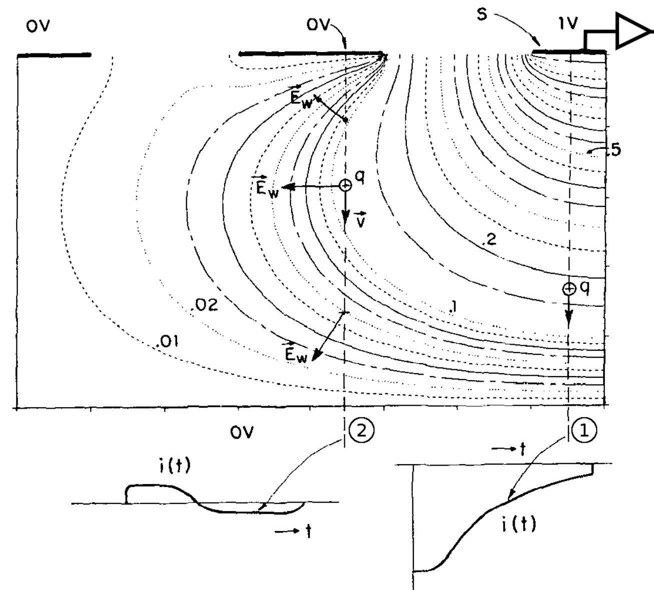

Figure 3.6: Illustration of the effects of Ramo's theorem. Due to the weighting field charge carriers moving close to the read out electrode of a segmented sensor induce a higher current. For charge carriers moving far away from the electrode the current vanishes in mean [15].

to the electrode their contribution to the total signal gets negligible. As this effect increases with the electrodes becoming smaller compared to the thickness of the sensor it is also named *"small pixel effect"*.

The segmentation of the electrodes is done to locate the transition point of the particle. To reach a higher spatial resolution than given by the granularity of the segmentation itself, the ratio of charge shared between segments can be used. Especially in the center between two segments, where the field vectors pointing to the either or the other electrode lay close together (chap. 6.1.1).

Next only a short overview of two different electrode geometries is given. The two most commonly used geometries are shown in fig. 3.7. One is the single-sided strip sensor. The electrode segmentation is carried out as strips. This

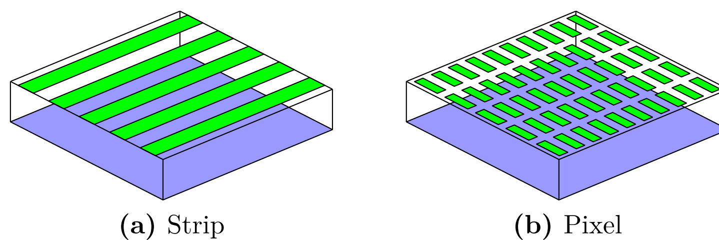

(a) Strip **(b)** Pixel

Figure 3.7: Different electrode geometries used for segmented semiconductor sensors

geometry allows the placement of the readout electronics on the sensor sides, but delivers spatial information just in one direction. To obtain two dimensional hit information one has to place two sensors with the strips in crossed orientation back to back or has to segment the electrodes of one sensor on both sides. In either cases the position determination has ambiguities if more than one particle is passing the sensor simultaneously. Pixel sensors solve this problem at the prices of an increased number of channels. The number of channels increase quadratically with the area instead linearly as for strip sensors. To equip all pixel electrodes with readout amplifiers usually either a specialized readout-ASIC[3] is directly connected on top using hybridization technology or a monolithic detector design is used which combines sensor and electronics on the same substrate. Details for the sensor types examined in this thesis are explained as needed in the corresponding chapters.

The most common solution to read out the sensor is to measure the total charge directly by use of a charge-sensitive-amplifier (QSA), as for example embedded in the ATLAS-Pixel readout electronics (see chapter 5). Figure 3.8 shows its principle. As for all measurements, one has to be able to separate the signal one wants to observe from the noise of the system. For the readout of a sensor this means that one has to distinguish the induced current from the particle transition from the leakage currents and the noise introduced by the readout amplifier. The latter depends by design on the capacity of the signal source [14]. The lower the capacitance and the leakage current of a sensors, the better signal to noise ratios are reachable. In first order the capacitance of a sensor channel corresponds to the one of a parallel plate capacitor:

$$C = \epsilon_0 \epsilon_r \frac{A}{d}, \tag{3.18}$$

where $\epsilon_0 \epsilon_r$ is the material dependent permittivity, A is the electrode area and d is the thickness of the depletion zone, which should ideally be the sensor thickness. For pixel detectors, however, the pixel to pixel capacitance dominates by far [17, 18].

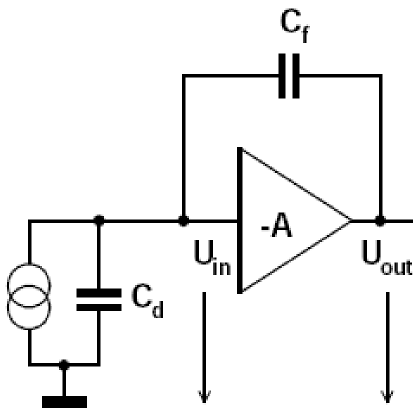

Figure 3.8: Principle of a charge-sensitive-amplifier (QSA). The detector is modelled as a current source (signal and leakage current) and a capacitor. While the voltage U_{in} (biasing of the sensor) is kept at a constant level, the voltage U_{out} changes in such a way, that the feedback capacity C_f absorbs the charge delivered from the sensor ($Q = C \cdot U$).

[3] Application Specific Integrated Circuit

3.4 Basic characteristics of silicon and diamond sensors

In this section the basic characteristics and properties expected for exemplary silicon and diamond sensors are discussed. For this the equations compiled in the previous sections have been used (for further details see also [14] or [19]). The required properties of silicon and diamond have been compiled in tab. 3.2. While silicon is well documented in the literature, values for diamond had partially to be derived either from graphite or scaled using silicon values. If done so, the reasonings are outlined in the text.

Silicon sensor used in todays high energy physics experiments have a typical thickness of several hundred μm . This is a trade off between several quantities like signal height, radiation length (deflection of a traversing particle) and required depletion voltage. In the following a silicon sensor made from a n-type substrate of about $200\mu m$ is assumed.

To allow full depletion of this sensor at a reasonable (well manageable) voltage of around 75V, lowly doped material with an effective doping concentration of $2.5 \cdot 10^{12}\,\mathrm{cm}^{-3}$ corresponding to $2\,\mathrm{k\Omega cm}$ is needed (eq. 3.12). This is 2-5 orders of magnitude less than standard material used in the silicon industry and already close to the intrinsic carrier concentration of $10^{10}\,\mathrm{cm}^{-3}$. Sensor grade silicon material has thus to be especially produced and the production of sensor grade p-type

property	symbol	silicon	diamond$^{\diamond}$	units	reference
atomic number	Z	14	6		
density	ρ	2.33	3.52	g/cm^3	
bandgap	E_g	1.12	5.48	eV	
electron mobility	μ_e	1450	1800 (4500)	cm^2/Vs	[20]
hole mobility	μ_h	505	1000 (3800)	cm^2/Vs	[20]
electron saturation velocity		2.4		2	$\times 10^7 cm/s$
intr. carrier conc. (300K)	N_{int}	10^{10}	≈ 1	cm^{-3}	
thermal conductivity (300K)		1.48	> 1800	$Wcm^{-1}K^{-1}$	
resistivity (300K)	ρ	10^3	$\approx 10^{13}$	$k\Omega cm$	
voltage breakdown		0.3	0.5 (4)	MV/cm	
relative permittivity	ϵ_r	11.9	5.7		
mean energy for e/h creation	$E_{e/h}$	3.61	13.1	eV	[21, 22]
av. energy loss MIP ($\Delta_{av.,MIP}$)	dE/dx	3.88	$6.14^{\dagger *}$	MeV/cm	[10]
		108	$47^{\dagger}$	$e/\mu m$	
		10.1	$5.7^{\dagger}$	Me/X_0	
radiation length	X_0	9.4	$12.1^{\dagger}$	cm	[10]

$^{\diamond}$ pCVD; values in brackets are for scCVD, †scaled from carbon value,
$^{\circ}$scaled from silicon value, *see text for explanation

Table 3.2: Material properties of Silicon and Diamond.

material is still a technology challenge. It has to be noted that p-type substrate with the same doping concentration shows three times the resistivity of n-type material (eq. (3.13)) as in silicon the mobility of holes is one third that of electrons (tab. 3.2).

The lower mobility results also in higher charge collection times. The maximum drift time occurs for electrons or holes traveling through the full sensor thickness. For the above stated sensor operated at its depletion voltage of 75 V the charge collection time is 14 ns for electrons and 41 ns for holes. The charge collection times are more than halved for a biasing at twice the depletion voltage. Namely to 2 ns and 6 ns correspondingly. This is as the biasing above the depletion voltage contributes linearly to the field inside the sensor, while below it contributes as given by eq. 3.11 as the space charge present due to the pn-junction effects the electric field. In addition to the drift according to the electric field a lateral spread of the charge cloud occurs by diffusion. For the stated sensor it is about 3 µm wide (Gaussian σ). It is the same for electrons and holes as the carrier mobility compensates for the differing drift times. For the same reason it is nearly independent of the material as long as the electrical field is the same.

The mean energy deposit of a MIP in silicon corresponds to 388 eV/µm or 107 e/µm. As stated in section 3.1 the most probable energy deposit and the FWHM of the distribution depends on the sensor thickness and the particle energy (fig. 3.2, fig. 3.3). For particles with a $\beta\gamma > 100$ (e.g. π>10 GeV) the most probable energy deposit Δ_p in a 200 µm thick sensor is calculated to be 58 keV which corresponds to a charge of 15300 e (eq. (3.2)). The expected ratio of Δ_p to the FWHM of the Landau distribution is about 2.5 (eq. (3.3)).

Diamond with its large band gap of 5.5 eV behaves more than an insulator than a semiconductor. The electrodes can be metalized directly on the surfaces without the need for implantation. The intrinsic carrier concentration is extremely low ($< 1cm^{-3}$) and the thermally generated leakage current is negligible. Therefore in contrast to silicon the creation of a carrier free region by means of a junction is not needed. The charge in the sensor is collected over the full bulk thickness as long as the biasing voltage is high enough to collect the charge carriers before they recombine or get trapped. This is especially important as diamond for sensor applications is predominately available as poly-crystalline material.

Artificial diamond wafers are industrially produced by *chemical vapor deposition* (CVD). The diamond is grown by depositing carbon from a microwave plasma, while simultaneously suppressing the formation of graphite by selective etching. The poly-crystalline structure originates from the parallel formation of seeds in the beginning of the growth process. Later on the growth process gets dominated by some of the seeds which leads to the grain structure as illustrated in fig. 3.9. The best diamond quality (lowest number of grain boundaries) is found close to the surface while the substrate side usually is of inferior quality. The grown diamonds have a coarse surface which needs to be ground and polished before being usable for sensor applications. By grinding the sensors are also brought to their desired

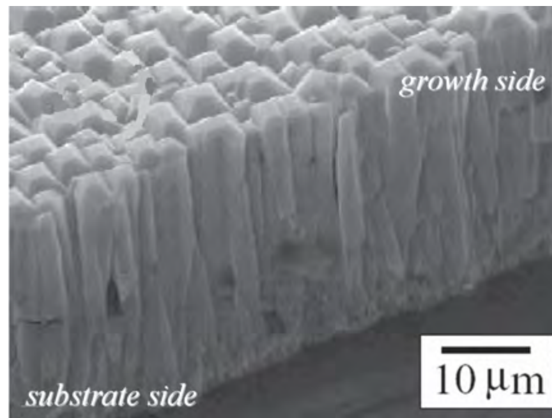

Figure 3.9: Grain structure of sensor grade poly-crystalline CVD-diamond [23]. Before metalization of the electrodes the material gets polished.

thickness, preferably by removing material from the lower quality substrate side. Nowadays also the growth of single crystalline material in sizes of about 1 cm^2 is possible by selecting an appropriate single crystalline substrate as seed [20].

The crystallite structure and the impurities inherent to such material cause trapping and recombination centers in the material. They limit the charge carrier life time. Charge carriers trapped at the grain boundaries might lead to space charge present in the bulk. The resulting lateral polarization fields have been observed to reduce the spatial sensor resolution by lateral charge drift or channeling effects [24]. However, in the last years the diamond quality has been significantly improved. Polycrystalline material suitable for sensor applications is commercially available at the 10 cm wafer scale. In recent times also single crystal material got available which misses the negative implications of grain boundaries.

A diamond sensor has no pn-junction. The absence of a pn-junction further results in a space charge free bulk which allows for charge collection even at low bias voltages. The mobility for electrons and especially for holes is much higher than the silicon value (tab. 3.2). For an ideal diamond sensor of 200 μm thickness this results in electron collection times of 1.5 ns. Due to the constant electric field inside the bulk the time scales linearly with the applied bias voltage. The charge collection times of holes are about the same.

While the energy deposit of particles is quite well documented for silicon, the values for diamond have to be derived. As already stated in the first section, the mean energy deposit is quite constant for all materials if expressed in terms of mass density. A good approximation for diamond seems therefore to scale the graphite value by the ratio in mass density. One obtains 6.14 MeV/cm, about 1.5 times the silicon value. For the creating of an e/h-pair, however, 13.1 eV are needed so that the number of e/h-pairs per unit length is 40%, per radiation length 60% of the silicon value. The mean charge deposited of a MIP in a 200 μm detectors is around 9400 e.

For applications in particle detection the most probable charge deposit and the width of the distribution is of higher importance than the mean energy deposit. This is, as a particle is usually detected by comparing the charge deposit against

a fix threshold value. As lined out previously, the actual shape of the landau distributions depends on the number of interactions taking place. Regarding sensor thickness this correlates to the electron density which scales between different materials roughly with the mass density. A first approximation for the relation between the mean energy deposition and the most probable charge deposition in diamond is thus to use the silicon value (fig. 3.3, eq. 3.2) where the thickness is scaled by the diamond to silicon ratio of the densities. The Landau distribution of a 200 µm thick diamond sensor is thus expected to have the shape of a 300 µm thick silicon sensor. While the silicon sensor has for a MIP a most probable to mean ratio of about 0.65, the ratio for the diamond of same thickness is 0.68. The same scaling reason narrows the ratio between the FWHM and the most probable value of the distribution by about 10% (Si: 2.5, C: 2.8). The values are quite sensitive to the detector thickness and thus have to be scaled individually for each detector. The most probable charge deposit of particles with $\beta\gamma > 100$ calculates to about 6800 e in a 200 µm thick diamond sensor. A 260 µm thick diamond collects a most probable charge of 9000 e and has the same radiation length as a 200 µm thick silicon sensor which collects 15300 e. Table 3.3 summarizes the characteristic values expected for the discussed sensors.

The most probable charge deposit in a diamond detector is 58% of the silicon value for a sensor of comparable radiation length. But on the other hand the charge distribution is narrower and the halved relative permittivity together with the negligible leakage current, even without cooling, allows to obtain higher signal to noise levels than for silicon detectors.

property	1	2	3	units
material	Si	Diamond	Diamond	
thickness	200	260	200	µm
radiation length	0.21	0.21	0.17	x_0/X_0%
pixel size	50x400	50x400	50x400	µm^2
capacitance (plate type)	10.5	3.9	5.0	fF
capacitance (pixel)†	500	180	240	fF
MPV ($\beta\gamma > 100$)	15.3	9.0	6.8	ke
FWHM ($\beta\gamma > 100$)	6.0	3.0	2.4	ke

† including pixel to pixel and stray capacitances. Based on the assumption, that the values scale like in the parallel plate case. The pixel capacity of an ATLAS pixel sensor has been used as reference value (400 fF[25]).

Table 3.3: Expected Properties of exemplary silicon and diamond sensors.

4 Motivation for Pixel Detectors using New Materials

The CERN Large Hadron Collider plans to start with a luminosity of $10^{33} cm^{-2}s^{-1}$ and is expected to ramp up to $10^{34} cm^{-2}s^{-1}$ during the first three years of operation. After that, it is planned to run at the nominal luminosity for the next 5-7 years, with a possible further increase to $2 \cdot 10^{34} cm^{-2}s^{-1}$. After this time vital components of the LHC and the associated experiments will suffer from radiation damage and need to be replaced. A maintenance shutdown of about one year will be unavoidable. This renders possible updates of components to extend the physics potential of LHC and its associated experiments.

For the observation and characterization of a physics process it has to occur often enough during the runtime of the experiment. The average number of events observed is given by the product of the cross section of the process and the integrated luminosity over time:

$$\langle N \rangle = \sigma(E) \cdot \int_0^T \mathcal{L}(t)\, dt \tag{4.1}$$

The error on a measurement usually scales with the number of observations. If the measured quantity follows for example a Gaussian distribution, after 5 years of operation an additional runtime of 15 years would be required to half the error ($\sim 1/\sqrt{N}$). To increase the physics discovery potential, the number of events generated for the process of interest has to be increase either by an increase in luminosity or by an increase of the processes cross section. For some processes, especially in the supersymmetry and extra dimension sector this is possible by an increase in energy. An increase in the colliders energy, however, would demand for higher magnetic fields to guide the beam. This would require impossible or extremely costly changes in the accelerator system. The only feasible option at the moment for a *super LHC (sLHC)* is to go for an increase in luminosity.

If two bunches containing n_1 and n_2 particles collide with frequency f, the luminosity is

$$\mathcal{L} = f \cdot \frac{n_1 n_2}{4\pi\sigma_x\sigma_y} = f \cdot \frac{n_1 n_2}{4\sqrt{\epsilon_x \beta_x^\star \epsilon_y \beta_y^\star}}, \tag{4.2}$$

where σ_x and σ_y characterize the Gaussian transverse beam profiles in horizontal and vertical direction assuming for simplicity the beam profiles to be equal. Instead of σ in the description of accelerators usually the terms *transverse emittance*, ϵ, and *amplitude function*, $\beta^\star$, at the interaction point are used. The parameters

n_1,n_2 and f are mainly determined by the injection system and affect the beam current, while the focusing at the interaction point (σ) is related to the associated focusing magnets. Thus the upgrade options presently[1] discussed either strive for a major enhancement in the beam injection (more protons, more bunches) or the focusing system.

An increase in luminosity will affect the requirements for experiments like ATLAS. The number of interaction occurring simultaneously during one beam crossing will increase accordingly to the luminosity increase. The rarely occurring processes of interest will thus be buried in an increased amount of background. This effect is illustrated in fig. 4.1. The detectors system must be able to deal with this pile-up of particle tracks.

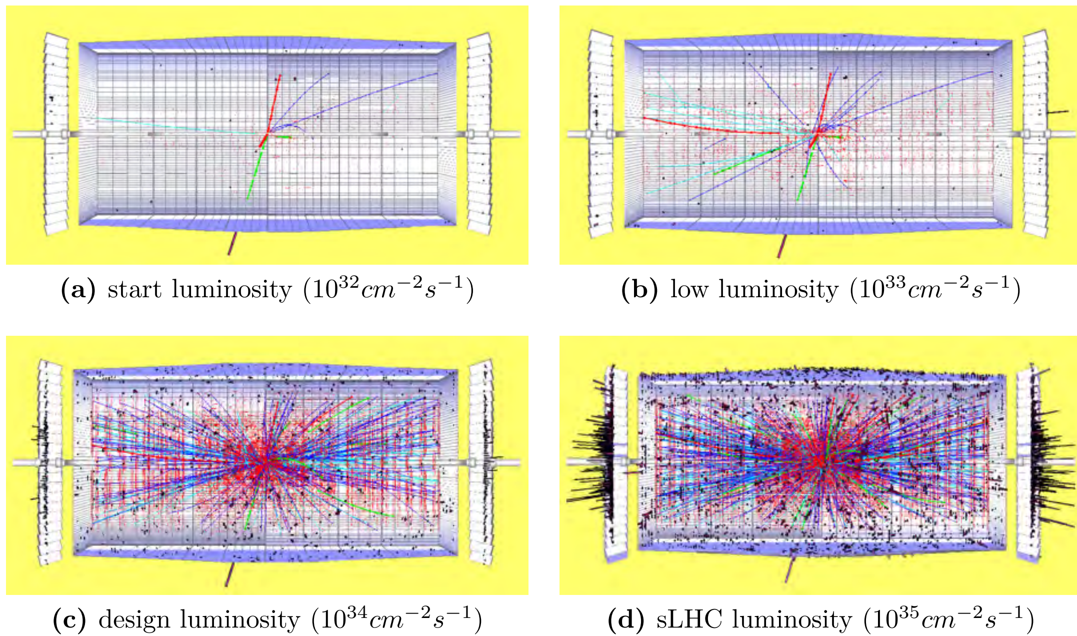

(a) start luminosity ($10^{32}cm^{-2}s^{-1}$) **(b)** low luminosity ($10^{33}cm^{-2}s^{-1}$)

(c) design luminosity ($10^{34}cm^{-2}s^{-1}$) **(d)** sLHC luminosity ($10^{35}cm^{-2}s^{-1}$)

Figure 4.1: Four event displays of an event $H \rightarrow ZZ \rightarrow \mu\mu ee$ ($m_H = 300\,GeV$) simulated in the CMS detector. From (a) to (d) the luminosity increases from $10^{32}cm^{-2}s^{-1}$ to $10^{35}cm^{-2}s^{-1}$, resulting in a corresponding increase of the background level [26].

Background levels and distributions at the nominal LHC luminosity have been extensively studied for the ATLAS environment [27]. As the beam energy is unchanged for sLHC, the radiation composition is expected to stay the same for sLHC while the intensity scales with the increase in luminosity. The extrapolated particle rates for the ATLAS inner detector region at sLHC luminosity are shown in tab. 4.1.

For the innermost layers at radii of several centimeters around the beam axis, the particle rates are dominated by charged pions and photons. Most of the

[1] September 2008

Radius $[cm]$	Particle rates $[MHz/cm^2]$						F_{neq} $[10^{14}/(cm^2y^{-1})]$	Dose $[kGy/y]$
	γ $> 30\,keV$	p $> 100\,MeV$	n $> 100\,keV$	$\pi^{\pm}$ $> 10\,MeV$	$\mu^{\pm}$ $> 10\,MeV$	e^{-} $> 0.5\,keV$		
5.05	458	20.3	41.4	341	3	81	27	1580
12.25	91.5	2.8	12.4	41.2	1.9	17.3	4.6	254

Table 4.1: Particle rates, fluences and doses expected at the innermost tracking detector layers at sLHC luminosity of $10^{35}cm^{-2}s^{-1}$. Extrapolated from data in [3].

charged particles are originating from the interaction point. Some of the photons are produced also directly and in interactions with the beam pipe, but most are created by neutron capture processes. The neutrons are mostly the result of back-splash from the calorimeters (albedo). In the study of radiation induced damage it is useful to introduce a quantity called the $1\,MeV$ neutron equivalent fluence (F_{neq}) which normalizes the damage to the one expected from $1\,MeV$ neutrons. For the region of the inner tracker fig. 4.2 shows the expected fluences during the lifetime of the sLHC.

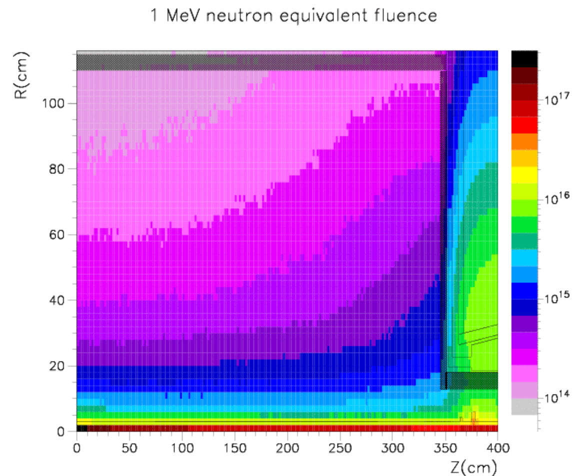

Figure 4.2: Integrated 1 MeV neutron equivalent fluence in dependence of the position inside the ATLAS inner tracker region. The calculations are based on an integrated beam luminosity of $3000fb^{-1}$, corresponding to three years of sLHC operation [28]. The innermost layer of a tracker upgrade is to be installed at a radius of about $5\,cm$ covering the $z = \pm 40\,cm$ region.

As consequence, a detector system at the sLHC luminosity of $10^{35}cm^{-2}s^{-1}$ has to cope with two major issues:

1. Pile-up of tracks caused by the high amount of instantaneous produced particles.

2. Radiation damage caused by the integrated particle flux.

The first can be addressed by highly segmented detectors allowing the separation of hits belonging to different particle tracks. The second demands for the development of radiation hard detector technologies which survive a tenfold increase in particle flux compared to the already harsh LHC environment. For the innermost layers of the tracker upgrade both issues can be tackled at once by using radiation hard pixel sensors.

4.1 Radiation damage

The main energy loss of a charged particle in matter is due to ionization of the lattice atoms (*Ionizing Energy Loss* (IEL)). While this generates the signal as stated in the previous chapter, it has no permanent influence on the material characteristics. For integrated circuits, however, ionization occurring especially in the oxide layers has an effect [14].

For semiconductor sensors the bulk damage due to destruction of the periodic lattice structure is of higher relevance. It effects the electronic properties of the material. The energy to dislodge an atom is highly material depended but in the order of $10 - 40\,\text{eV}$. Momentum conservation in the scattering hence sets a threshold energy for damage effects. In commonly used semiconductors the momentum threshold for electrons and photons (in case of the latter through secondary Compton electrons) is around 250 keV and is much smaller for the heavier particles ($\approx 200\,\text{eV}$). An 1 MeV neutron transfers on average 60 keV to a silicon atom. With this energy the recoil atom displaces in cascade interactions additional atoms and creates a cluster of defects. If nuclear reactions occur (e.g. for low energy neutron capture) the reactants remain as foreign atoms in the lattice and the recoil energy from emitted gamma rays is high enough to cause additional displacements.

The displacement damage is linked to the *Non Ionizing Energy Loss* (NIEL) [30]. Therefore the NIEL hypothesis is often used to scale the damage observed in one particular case to other kinds of particles and energies. The hypothesis is, that any displacement induced change in the material scales linearly with the

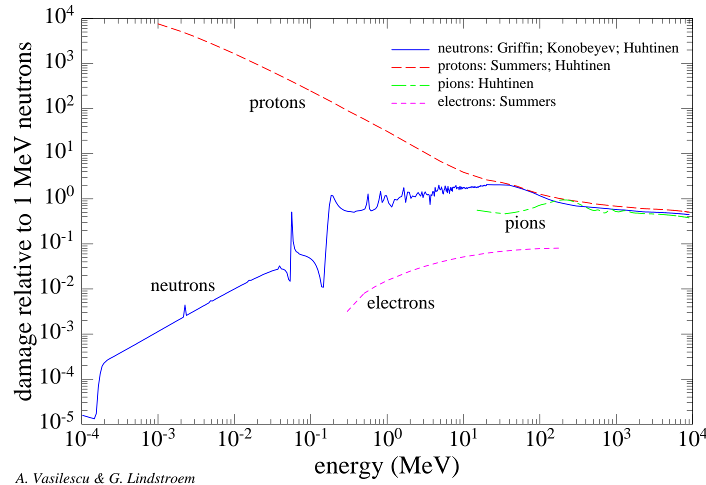

Figure 4.3: Displacement damage vs. energy for neutrons, protons, pions and electrons, scaled to the damage of 1 MeV neutrons [29].

amount of energy in the displacing collision. The non ionizing energy loss is not proportional to the total energy absorbed, but depends on the particle type and energy. The NIEL has been calculated for a variety of particles and for a large energy range. Based on the hypothesis, fig. 4.3 shows the displacement damage versus energy for different kinds of particles plotted relative to 1 MeV neutrons [29]. While NIEL scaling is usually taken for granted, several experimental results are indicating that NIEL scaling is not fully established [31]. Nevertheless NIEL scaling can be used to estimate relative effects. Measuring the radiation effects for all particles and energies relevant for the targeted radiation environment is impracticable.

The damage establishes itself as empty lattice sites (vacancies), atoms between regular lattice locations (interstitials), foreign atoms placed in the lattice structure and as conglomerates of these. Most of the primary defects created by the particles are mobile and the actual appearance of the defect states in the band structure evolve with time. In the beginning an annealing of the lattice structure reduces the number of defects (beneficial annealing). Stable defects are forming afterwards (reverse annealing). Common to all defects is the formation of additional energy levels in the bandgap (fig. 4.4). The actual appearance of the energy levels is highly material and temperature dependent.

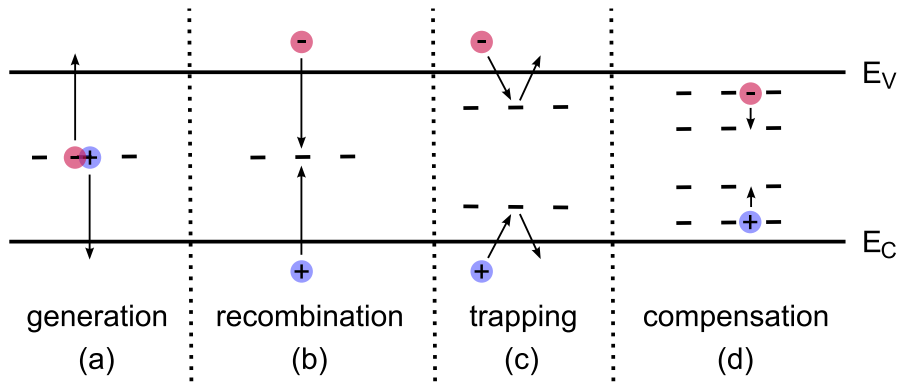

Figure 4.4: Intermediate energy levels induced by the dislodge of atoms can (a) help in the creation of thermal charge carriers, (b) act as recombination centers, (c) temporarily trap charges and (d) alter the effective doping.

The formation of mid-gap states facilitates the transition of electrons from the valence to the conduction band and becomes even worse, if multiple states form spread over the bandgap. The energy gap to overcome in one step by thermal excitation is reduced and the leakage current thereby increases. The increase of leakage current after radiation can be parameterized by [32]

$$I_d = I_0 + \alpha \cdot \Phi \cdot Ad, \tag{4.3}$$

where I_0 is the leakage current before irradiation, α is a damage coefficient dependent on particle type and energy, Φ is the particle fluence and the product

of detector area A and thickness d is the detector volume. The parameterization is valid quite generally, as it only assumes a uniform defect formation over the bulk, without depending on the details of the defects' energy states. A value of $\alpha = 3.99 \pm 0.03 \times 10^{-17} A/cm$ has been found to be in good agreement for various type of silicon detectors (fig. 4.5)[33, 34]. For diamond detectors no significant increase in leakage current has been observed [35]. Leakage current has an exponentially dependence on temperature, as it is proportional to the number of thermally produced charge carriers (chap. 3.3, eq. 3.10). This might lead to a thermal runaway and finally the destruction of the device. In thermal runaway the radiation induces an increase in leakage current which results in heating up of the device which in turn increases the current and so on. Beside this, an increased leakage current also negatively effects the signal to noise ratio achievable in a detector system [19, 14].

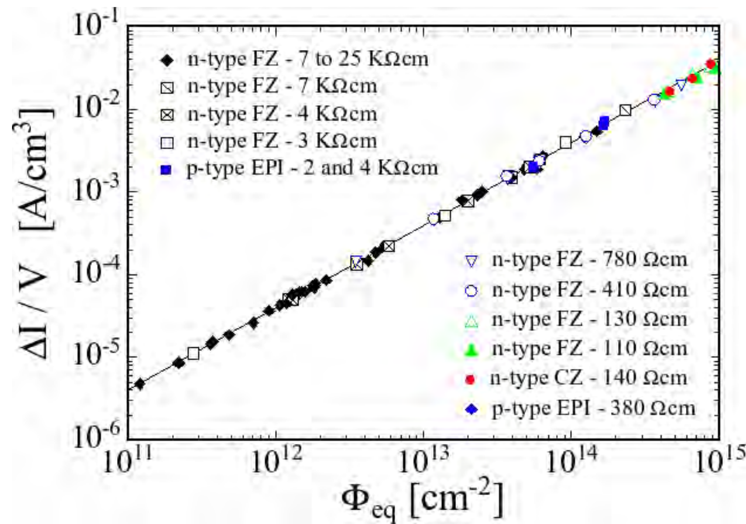

Figure 4.5: Fluence dependence of leakage current for various silicon detectors. The current was measured after heating at 60 °C for 80 minutes ($\alpha = 3.99 \pm 0.03 \times 10^{-17} A/cm$) [33].

Defects creating empty states close to the conduction band or filled states close to the valence band are trapping centers in which signal charge can be captured. Trapped charge either recombines or is released after some time by thermal activation. In so called deep level defects charges are trapped for a long time. This implies an effect commonly referred to as *pumping*. Charge collected at the readout electrodes increases from particle transition to particle transition as the deep level traps get filled up. The signal increases initially with time when under irradiation. Trapped charges also build up a space charge inside the detector volume, which affect the electric field inside the sensor and thus the drift of the signal charges.

The presence of trapping centers is common to all semiconductors with imperfect lattice structures and hence plays an important role for poly-crystalline materials

like diamond or composite semiconductors, e.g. GaAs. To assign the transition of a particle to a certain event, only charge carriers arriving in a certain time interval are useful. Trapped charge carriers do not contribute to the signal current. Especially sites with long trapping times (compared to the traveling time of the signal carriers), but short enough to be emptied again before charge carriers of a new particle transition arrive, limit the charge collection properties of the material. The loss of charge for the signal generation can be expressed in terms of a carrier lifetime τ, which is the average time a charge carriers travels before getting captured. The *charge collection distance* (ccd) is given by:

$$ccd = \tau \cdot v_c = \tau \mu E, \tag{4.4}$$

with the drift velocity v_c being the travel speed μE of the charge carriers. The lifetime decreases linearly with the concentration of trapping sites. Its flux dependence can be expressed as

$$\frac{1}{\tau} = \frac{1}{\tau_0} + \beta \cdot \Phi, \tag{4.5}$$

where Φ is the particle fluence, τ_0 is the carrier lifetime before irradiation and β is the damage coefficient depending on the kind of irradiation and material. For silicon damaged by fast charged hadrons a $\beta_h = 6.6 \pm 0.9 \times 10^{-16}\,\mathrm{cm}^2/\mathrm{ns}$ for holes and $\beta_e = 5.4 \pm 0.4 \times 10^{-16}\,\mathrm{cm}^2/\mathrm{ns}$ for electrons has been found independent of the type of doping and the material [34]. The damage coefficients for CVD diamond have been observed to be less than for silicon, but in the same order of magnitude ($\beta_e = \sim 2 \times 10^{-16}\,\mathrm{cm}^2/\mathrm{ns}$) [36]. In pixel detectors mainly the charge carriers moving close to the electrodes contribute to the signal (chap. 3.3). Charge carriers produced far away from the electrodes will most likely get trapped before reaching this region. Thus no significant increase in signal amplitude is obtained for detectors thicker than their corresponding charge collection distance.

The creation of states inside the bandgap also changes the effective doping concentration of semiconductors. Beside an increase in leakage current this especially changes the characteristics of junction based sensors. In silicon the damage results in the removal of donor levels and the creation of acceptor states. Therefore the properties of weakly doped n-type material are particularly effected. With the ongoing donor removal the doping concentration decreases until it reaches the point of *type inversion* where the radiation induced creation of new acceptor states takes over and the material starts to behave p-type like. Figure 4.6 shows the change in doping concentration of n-type bulk material typically used for sensor production. This change in doping concentration implies, that the bulk material reaches after a certain flux a doping level which does not allow anymore for a depletion at a reasonable bias voltage. In addition, the transition of n- to p-type material changes the location of pn-junctions inside the sensor. A previous n^+-n transition transforms to an n^+-p junction and a previous p^+-n junction transforms to an p^+-p transition.

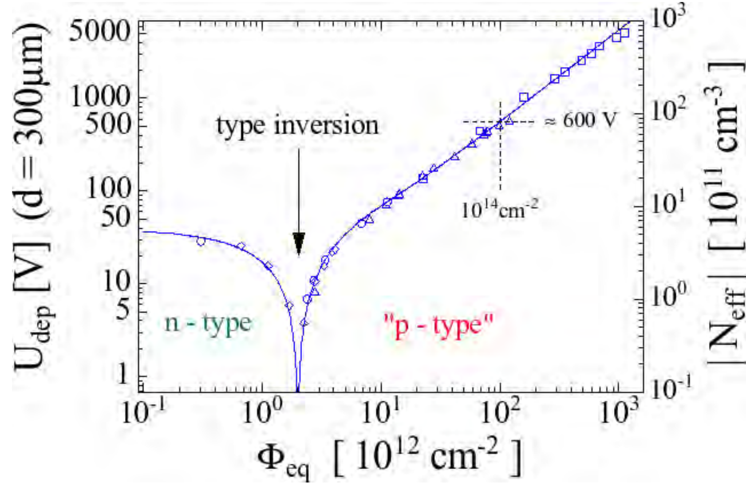

Figure 4.6: Change of the effective doping concentration in standard n-type silicon, as measured immediately after neutron irradiation [37].

4.2 Radiation hard sensor designs

The type inversion of n-type material, the increased leakage current and the limited carrier lifetime let traditional silicon sensors stop operating already at a relatively low flux in the order $10^{12-14}\,\mathrm{cm}^{-2}$. To ensure operation even at fluence above $10^{15}\,\mathrm{cm}^{-2}$, as required for present and further collider experiments, several measures are needed to deal with the implications of radiation.

Figure 4.7 illustrates the implications of type inversion on the operation of partially depleted sensors. Underdepleted operation becomes necessary if the increase in doping level does not allow anymore for full depletion of the sensor at reasonable biasing voltages (fig. 4.6). Traditionally p-in-n sensor are used, as they require for fabrication only the segmentation of the sensor implants on one side. After type inversion, however, the undepleted region of the sensor is shorting the p^+ pixel implants and make an underdepleted operation impossible. N-in-n sensors on the other hand, like used in ATLAS [38] have the depletion zone growing from the n^+-pixel implants and the drifting charge carriers are still seen by the individual electrodes. The undepleted portion of the sensors just does not contribute anymore to the charge collection. Before type inversion the n-in-n sensor still has to be operated fully depleted. This is no problem at all as the required depletion voltage is below the one required after irradiation.

Further radiation hardening can be accomplished by “defect engineering” of the used sensor material. Some of the stable defects which form have a major influence on the change of the effective doping concentration. Oxygenated silicon has been found empirically to create less severe damage states than the non-oxygenated standard material [31]. Research and development targeting this topic is carried out by the CERN based RD50 collaboration [39].

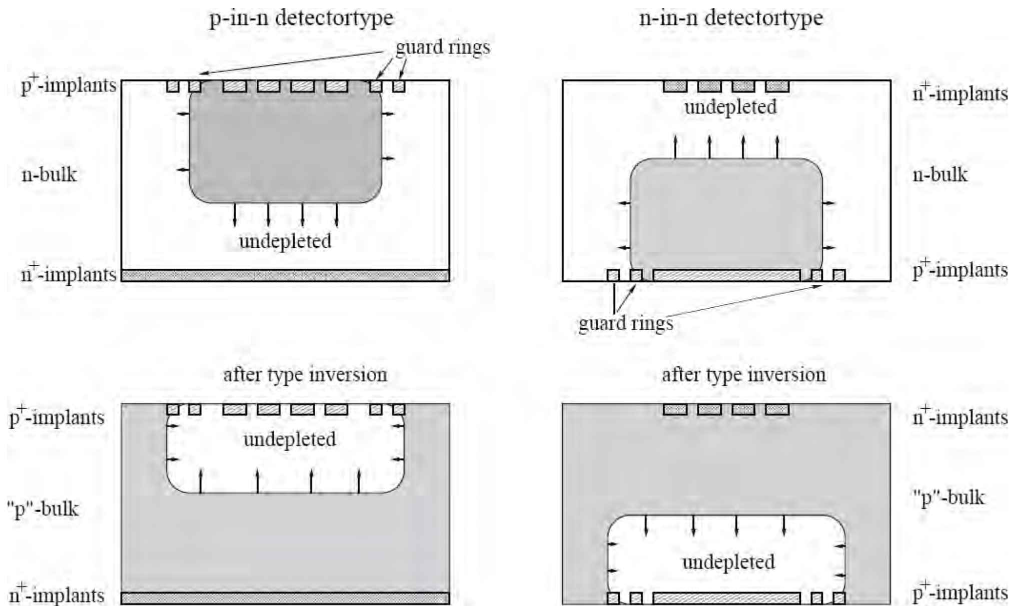

Figure 4.7: Sketch of the extend of the depleted sensor region in case of underdepleted operation for n-in-n (left) and p-in-n (right) sensors before (top) and after (bottom) irradiation [38].

Cooling of irradiated sensors is critical to limit the leakage current during operation, especially to prevent the thermal runaway. This requires the incorporation of a cooling concept in the detector design adding to the space and material requirements. To slow down the formation of stable defects (reverse annealing) also a continuous cooling is essential. In the case of ATLAS the sensors are cooled down to $-6\,°C$. Nevertheless the unavoidable warming-up during the maintenance periods of several weeks per year add already significantly to the degeneration of the sensors.

For fluences of about $10^{16}\,\mathrm{cm}^{-2}$ a further limitation occurs from the reduced charge carrier lifetime by the induced trapping centers. The resulting charge collection distances are much lower than the typical sensor thickness of $250\,\mu\mathrm{m}$.

To make sensors operational at high radiation levels further research and development is needed. Several options are discussed to address the problems occurring from the increased leakage current, the reduced carrier lifetime and the change in effective doping concentration. Possibilities are for example the further improvement of the bulk material by defect engineering, p-bulk based detectors which inherently are not effected by type inversion or thin silicon detectors allowing higher fields for fast charge collection [34].

A new concept which breaks with the traditional sensor concept and addresses the radiation effects by a different electrode geometry are the so called 3D-sensors [40]. In contrast to planar sensors the electrodes are driven into the bulk (fig 4.8).

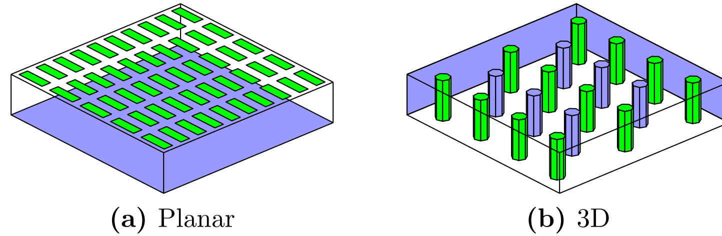

(a) Planar **(b)** 3D

Figure 4.8: Principle of a planar-sensor compared to a 3D-sensor. While for planar sensors the pixels are placed on top, they are driven for 3D-sensors into the bulk.

By an appropriate arrangement of the electrodes the p- to n-electrode spacing can be made smaller than the bulk thickness. This allows lower depletion voltages and shorter travel distances for the charge carriers while still generating signal over the full bulk thickness. In addition the edges of the sensor can be fabricated as electrodes. This avoids insensitive edges which are inherent to planar sensor designs. In chapter 9 prototype detectors based on the 3D-design are discussed.

Another approach is the use of a sensor materials which is inherently more radiation resistant. Diamond is such an option [41]. In terms of radiation damage, diamond sensors benefit from the large bandgap of diamond. Even after irradiation and without cooling the leakage current is in the order of several $\mathrm{pAcm^{-2}}$. The negligible leakage current significantly improves the signal to noise ratio obtainable for irradiated sensors. Besides that, diamond sensors are nearly unaffected by the radiation induced changes to the effective doping concentration as they are non-junction devices. In addition, diamond has excellent thermal conductance (tab. 3.2) which can be exploited for intelligent, low mass cooling concepts to dissipate the heat from the adjacent readout electronics.

The challenge for the use as sensor material lies in the concentration of trapping sites and the therewith correlated charge collection distances (fig. 4.9). The research and development undertaken by the CERN RD42 collaboration, in close cooperation with the CVD-diamond manufacturer "elementsix"[2], has succeeded to produce routinely 10 cm wafer scale poly-crystalline CVD-diamond (pCVD) with charge collection distances of more than 300 μm [42]. The charge collections distance thus reaches the thickness of a typical sensor. In recent times also the first singlecrystal diamond sensors (scCVD) have been produced in sizes of about $1\,\mathrm{cm}^2$ (fig. 4.10(b)). These sensors do not show the negative effects of the mentioned grain boundaries of pCVD-diamond and show full charge collection over the whole detector thickness.

Within RD42 several diamond based sensor devices have been built to explore their capabilities and to study their behavior with increase in radiation dose. Polycrystalline and single crystal CVD-diamond pixel detectors, as they are under study for a LHC upgrade, are the topic of chapter 8.

[2]former "De Beers Industrial Diamonds"

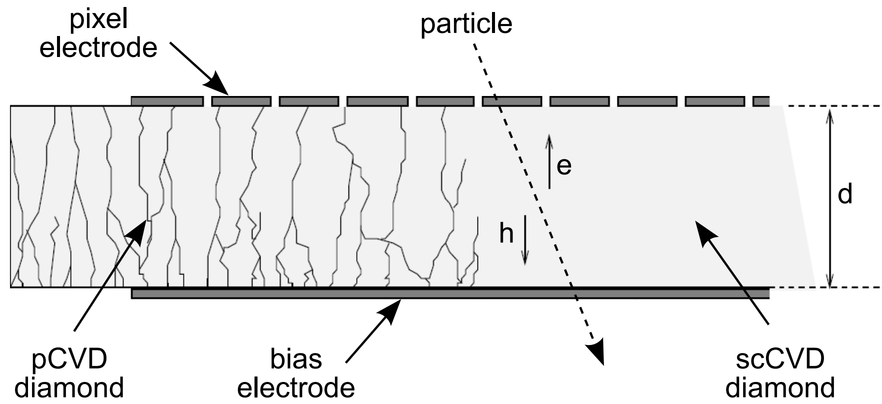

Figure 4.9: Schematic view of a diamond pixel detector. The left and right part of the sketch illustrate the difference between a poly-crystalline (pCVD) and a single crystalline (scCVD) diamond sensor. While the grain boundaries of poly-crystalline material influences the drift and recombination of the charge carriers, this is not the case for the single crystal material.

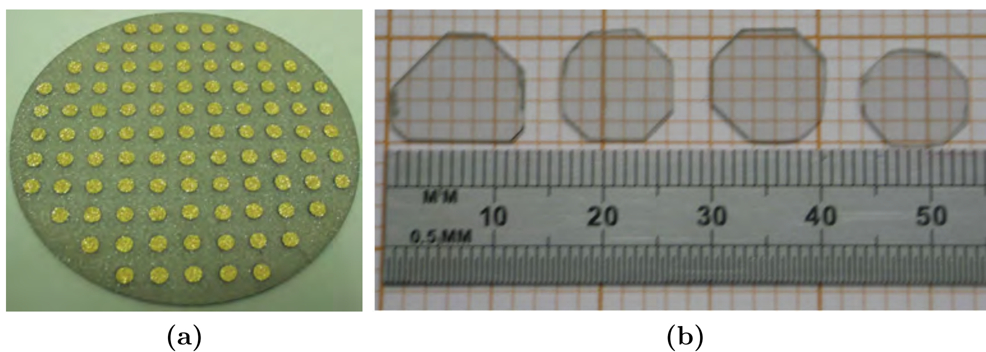

(a) **(b)**

Figure 4.10: (a) pCVD 10 cm wafer, with metalization dots on top. (b) several scCVD samples.

5 The ATLAS Pixel Modules

The building blocks of the ATLAS pixel detector are the pixel modules. Each has a size of about $2 \times 6\,\mathrm{cm}^2$. Basically a detector module consists of a silicon sensor, 16 front-end (FE) chips for the readout connected to the sensor via bump connections and a flex-hybrid which distributes the power and provides the interface to the global readout/control system. In fig. 5.1 a schematic cross section of a pixel module along its short direction is shown. The lower part shows a top side view of the module. Next the individual parts will be described.

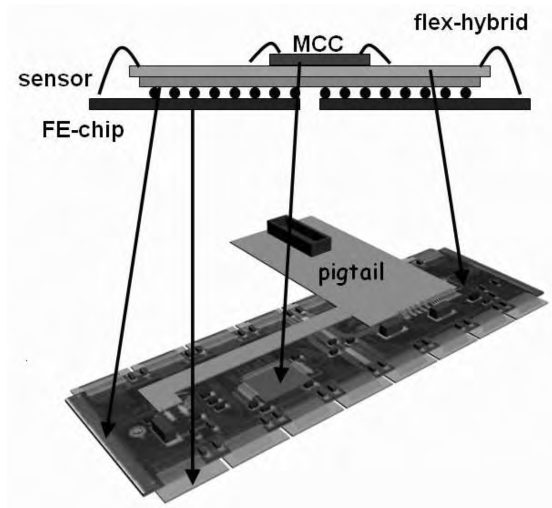

Figure 5.1: Pixel module overview, showing the individual components of a barrel module: sensor, FE-chips, flex-kapton-hybrid with pigtail and module control chip (MCC) [4].

The sensor

For the sensor $250\,\mu\mathrm{m}$ thick n-type bulk silicon is used. The sensor has a p^+ back plane and the individual pixels are made by n^+ implants. The sensor has thus an n-in-n design and is made for the collection of electrons. The high resistivity $(2-3\,\mathrm{k}\Omega/\mathrm{cm})$ bulk material allows depletion of the unirradiated sensor at around 60 V. To increase the radiation tolerance oxygenated silicon is used. The sensor has an active area of $1.64 \times 6.08\,\mathrm{cm}^2$. The sensitive area is surrounded by a $500\,\mu\mathrm{m}$ wide guard ring structure to prevent bias voltage breakdown, especially for the operation at high bias voltages as needed after accumulating a high radiation dose.

The sensor is divided into 47232 pixels which are connected to 16 FE-chips. The nominal pixel size is $400 \times 50\,\mu\mathrm{m}^2$. For a full coverage in the region between

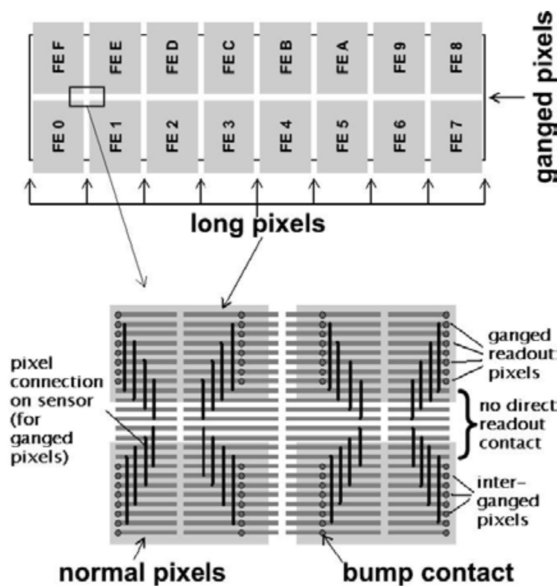

Figure 5.2: Schematic drawing of the arrangement of the FE chips on the sensor (top) and as zoom-in the sensor layout near the FE chip edges, illustrating long, ganged and inter-ganged pixels (bottom) [43].

two readout chips the pixels are enlarged to $600 \times 50\,\mu\text{m}^2$ and/or two pixels are connected together to make way for the chip placement (see fig. 5.2 for illustration). The pixels are oriented in such a way, that the long side of a pixel corresponds to the long side of the module. More details on the sensor layout can be found in [38].

The sensor-chip interconnection

Each pixel cell of the sensor is connected via an individual solder bump to the corresponding read-out amplifier on the front-end chip (fig. 5.3(a)). The pitch of the solder bump connections is given by the shortest pixel dimension of $50\,\mu\text{m}$ (fig. 5.3(b)).

For the production of the modules two different techniques were used. One is based on PbSn (solder) and provided by IZM[1], the other is based on Indium and carried out by SELEX[2] (former AMS). For the production of the sensor prototypes studied in this thesis only solder bumping has been used.

The solder bump deposition is carried out in several steps [44]. The cross section of solder bump is shown in fig. 5.4. In a first step the so called *under bump metalization* (UBM) is placed on the designated chip pads. The UBM consists of several sputtered metal layers. They prevent diffusion of the solder material and improve its adhesion and wettability. The PbSn for the bump bond is grown in a galvanic process on top of the UBM. The bump bonds get their spherical shape by the surface tension of the molten solder during a subsequent heat up. The PbSn bump bonds have to be applied only to one of th part being connected. The

[1]Institut für Zuverlässigkeit und Mikrointegration, Berlin, Germany
[2]Sistemi Integrati, Rome, Italy

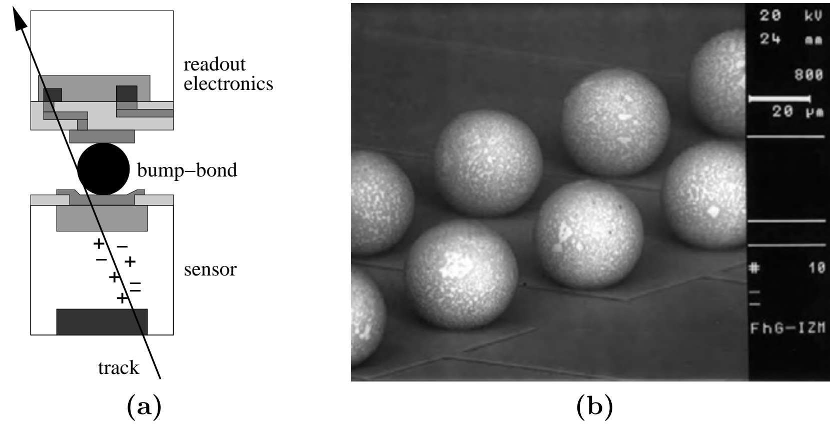

Figure 5.3: (a) cross section of a hybrid pixel detector (not to scale), showing one bump connection between a sensor and an electronics pixel cell [4]. (b) rows of PbSn solder bumps as found on the FE-chip (courtesy IZM-Berlin).

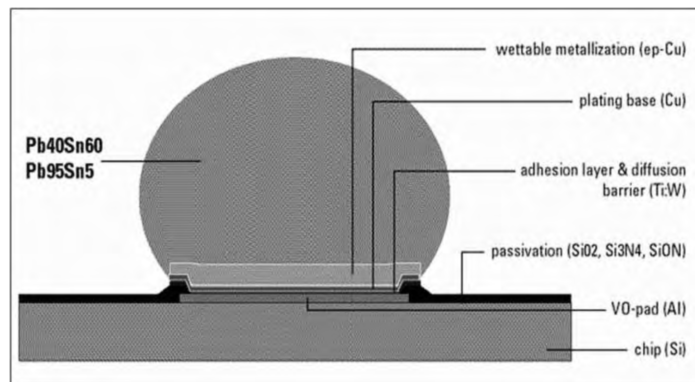

Figure 5.4: Build-up of a eutectic PbSn solder bump [44].

other part receives only the UBM metalization. During the fabrication of the pixel modules, the smaller FE chip instead of the sensor has been chosen for the bump bonds due to yield reasons.

The parts are mated by *flip-chipping*. The bump pads of the two parts are brought on top of each other with some flux. In the subsequent reflow the parts self-align by the surface tension of the solder. This process is comparable to the soldering of electronic components in the now commonly found BGA[3]-housings to a printed circuit board.

[3]Ball Grid Array

The readout chip

The front-end chip is fabricated in a 0.25 μm CMOS process using radiation tolerant layout rules [45]. To reduce the contribution to multiple scattering, the chips are thinned down to a thickness of 180 μm. The chip is responsible for the digitization and buffering of the pixel hit information until the global ATLAS trigger decision is taken. The digital part operates synchronously to the 40 MHz beam clock. A chip has 2880 individual pixel cells organized in 18 columns an 160 rows. Figure 5.5 shows the picture of a chip.

Figure 5.5: Picture of the FE chip. On the lower edge the connection pads are located. The homogeneous colored region above contains the *end of column* logic which takes care of the hit buffering and read-out driving. The upper region shows the pixel electronics, which is organized in 9 double columns and 160 rows. Taking a close look, the white lines can be identified as the individual pixel connection pads.

Each pixel cell has a physical dimension of $400 \times 50\,\mu m^2$ and contains a charge sensitive analog amplifier, a discriminator and digital output interface. A schematic view of the core components inside a cell is given in fig. 5.6. In the following a more detailed description of the chip internals is given.

The signal from the sensor enters the amplifier DC-coupled via the bump bond pad. The first stage is a charge sensitive preamplifier. It incorporates a DC feedback scheme capable of compensating DC leakage currents at the amplifier input of more than 100 μA. The charge from the sensor is collected on a feedback capacitance of nominally 5 fF, which in turn is discharged by an adjustable constant current source (about $2 - 10$ aC/ns). The amplifier was designed for a silicon sensor of 250 μm thickness. A typical input signal of about 20 ke, equal to 3.5 fC, returns to baseline within the order of a micro second. The leakage compensation cannot be switched off. While this is usually no problem, it has implications for the operation of prototype sensors as a pixel cell with a short makes the depletion of the sensor impossible. Each amplifier can be disabled to prevent noisy sensor pixels from continuously generating hit detections in the subsequent stages. Otherwise buffer-overflows would result in losses of real hits. The preamplifier is followed by a DC-coupled second amplifier stage and a differential discriminator. The threshold of the discriminator can be adjusted in the range of about 2000 e to 5000 e and

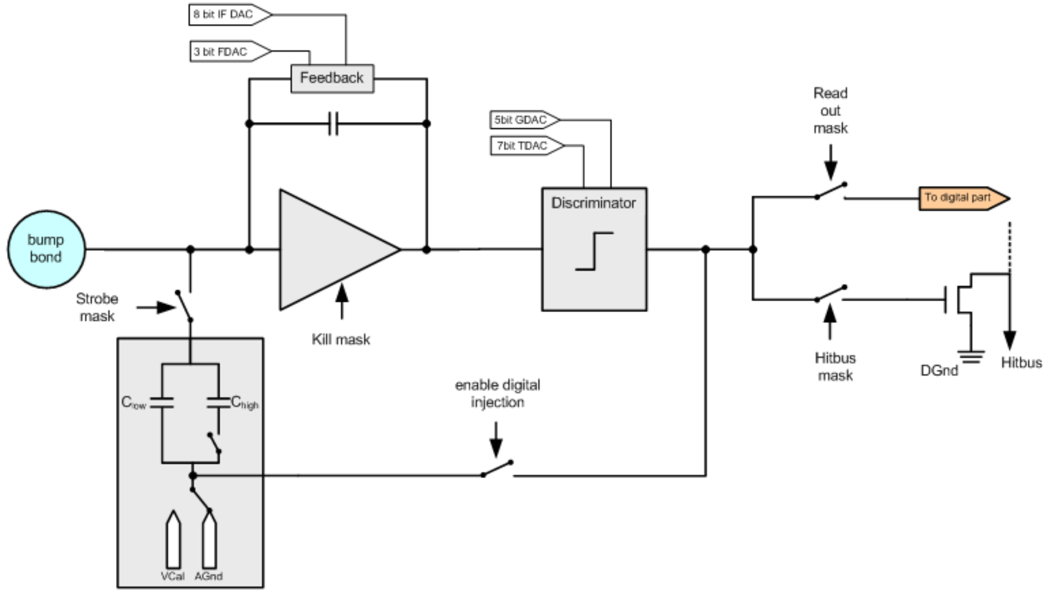

Figure 5.6: Schematic view of the analog part of a pixel cell in the FE chip including control signals and test circuits [46].

even wider, if higher noise levels and/or higher pixel to pixel deviations of the thresholds are acceptable.

By design, the output signal of the amplifier peaks always after the same time, independent of the amount of injected charge. The time constant of the exponential rise function depends on the sensor capacitance and the transconductance (g_m) of the preamplifier. The limit is thus set by the tolerated chip power consumption. The finite rise time implicates, that a hit with a small charge deposition crosses the threshold later than one with a larger charge deposition. Hits with small charge deposition thus might show up in the next event as the discriminator output is sampled once every 25 ns, corresponding to the 40 MHz bunch crossing frequency of LHC. This effect is usually referred to as *time walk*. Due to the constant discharge current, the time between the leading and the trailing edge of the discriminator signal, the *time over threshold* (TOT), is a direct measure of the deposited charge in a sensor pixel. Figure 5.7 illustrates the signal shapes at the different stages in dependence of the signal charge and adjustment settings. A hit pixel signals its pixel ID, the bunch crossing ID at which the signal crossed the threshold and the TOT value to the subsequent readout system.

The logic for the pixel readout is located at the bottom of the chip and is realized in two stages. The first stage continuously scans the pixel cells for hits. The identified hits are copied to the *end of column* (EOC) buffers. Two columns (320 pixels) share a common buffer with a depth of 64 hits. While a pixel is waiting for the transfer of its hit information it is insensitive. If no buffer space is left, a hit is lost. Consequently the number of hits detectable in parallel, but also in sequence is limited.

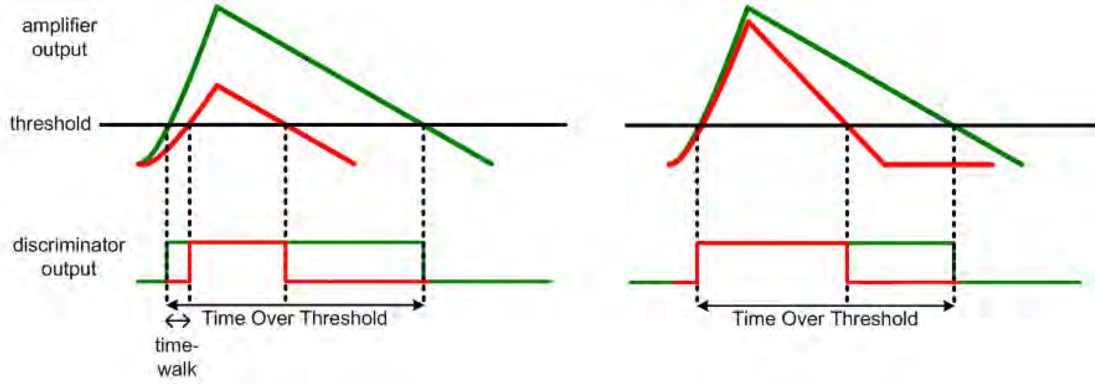

Figure 5.7: Output signals of the amplifier and the discriminator. The left picture shows the difference of the signals for a high (green) and a low (red) charge. The right one shows the difference of the signals for two different feedback current settings [46].

The EOC buffers are emptied by the second stage. In ATLAS the trigger to readout a specific event arrives with a fixed delay (latency). At the arrival of the trigger the current bunch crossing ID is taken, the *latency* is subtracted and the hits corresponding to the resulting bunch crossing ID are marked for readout. The marked hits are serialized and clocked out in turn at the 40MHz speed of the system clock. If the time according to the latency has passed, hits for which no trigger has arrived are discarded. One consequence of this two staged readout is, that a hit is only visible if its TOT is smaller than the trigger latency, as otherwise the hit has not yet been transfered to the buffers by the first stage.

While the trigger is usually supplied from the outside, the chip is also equipped with a self trigger for testing purposes. The self trigger uses a signal of all discriminator outputs linked by an or and additional logic. The functionality of the FE-chip can further be checked at several stages of the readout chain. First of all the basic communication with the FE-chip can be verified by reading back the values written to the different chip and pixel registers. The digital part of the hit detection and the readout stage can be tested with the help of an externally applied strobe signal. The strobe signal can be used to overwrite the discriminator output of selected pixel cells and thus for simulating hit detections. To check the pixel amplifier and discriminator stage each pixel cell contains a charge injection circuit. If enabled, the strobe signal is used to vary the voltage applied to a capacity connected to the amplifier input. The voltage is switched between the analog supply voltage (VDDA) and a calibration voltage V_{cal}. The resulting voltage step injects a charge pulse into the amplifier input. Each chopper has two selectable capacitors with nominal values of $C_{low} = 7.5\,\text{fF}$ and $C_{high} = 43\,\text{fF}$. The amount of charge is equal to

$$Q_{inj} = C_{low/high} \cdot \Delta V. \tag{5.1}$$

The charge is usually measured in units of the elementary charge e. The voltage

V_{cal} can be generated inside the chip with the help of a 10-bit digital to analog converter (Vcal-DAC). Typically the resulting slope for ΔV is 0.9 mV/DAC. This this corresponds to an injected charge of about 42 e per VCal-DAC step in the case of C_{low} and of 240 e for C_{high}. The exact capacitor values of the individual FE-chips are measured during the tests following the wafer production. The dispersion of the capacitors values between the different pixel cells of a chip have been found to be in the order of 1.5% for C_{low} and 2.3% for C_{high} [43]. In addition the characteristics of the Vcal-DAC are measured during the test. The linearity of the DAC is measured to be within one DAC value. The injection of a known amount of charge is used for the adjustment of the threshold settings, the feedback currents and for the calibration of the TOT values (chap. 7.2). More details on the chip electronics and further testing possibilities are given in [45], [47] and [43].

The flex hybrid

The flex hybrid provides the routing of the power, data and control lines from the cable connection to the 16 FE chips of a module. It also contains passive components for power filtering and the *module control chip* (MCC). The MCC combines the event data from the 16 chips to a single data stream and distributes the control signals to the front-end chips. The flex hybrid is based on a 50 µm thick polyamide substrate with copper traces of 25 µm thickness on both sides. The cover layers on both sides are made of commercial solder mask material. While for the disk modules the connection cable is directly soldered to the flex, the cables for the barrel modules are connected by a connector placed on an additional flex-board ("pig tail") as shown in figure 5.1. The kapton material features a low pin-hole probability, as needed for the housing of the high voltage traces ($\approx$ 600V) for sensor bias and is radiation hard enough to survive the radiation dose received during operation.

For testing purposes and for the characterization of new sensor designs also so called *single chip assemblies* were produced. They use a smaller sensor which is adapted to fit on a single front-end chip. The readout chip itself and the bump bonding used are the same as for the module. The flex-hybrid is replaced by a printed circuit board on which the single chip assembly is glued on. Since only a single chip is operated, a MCC is not needed. On the next page, in fig. 5.8, such a single chip assembly is shown.

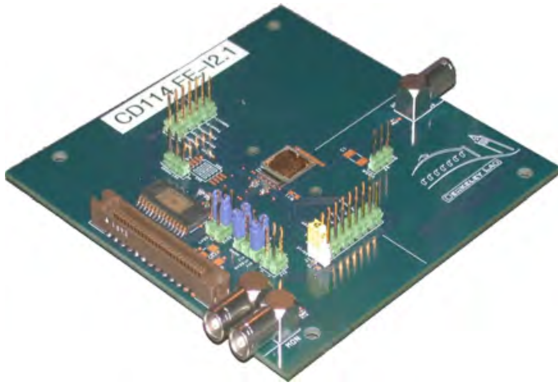

Figure 5.8: Picture of a *single chip card* as used for testing purposes and the first characterizations of new sensor designs.

6 The Testbeam Reference System

To characterize detector systems regarding their response on charged particles, tests are carried out in a mono energetic particle beam where the trajectories of the particles are recorded using a reference system (beam telescope). By knowing the position and the arrival time of an incident particle in the device under test (DUT), the device response can be characterized in detail. In particular this allows to study the charge sharing between adjacent sensor segments, the position resolution and the efficiency of the devices, core characteristics of tracking detectors. To carry out such measurements a testbeam setup as shown in fig. 6.1 is used. While the details of a testbeam setup vary for different applications, the basic concept of a beam test setup is usually the same.

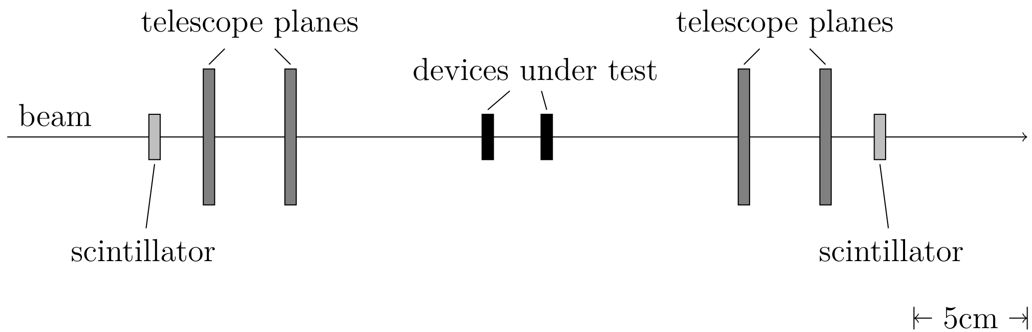

Figure 6.1: General testbeam setup

The passage of a particle is detected by the coincidence signal of two scintillation detectors in the front and back. It triggers the recording of the detector responses in the DUTs as well as in the telescope planes. The data collected from one trigger is called an event. A sequence of events without changes in the setup or reinitialization of the data acquisition system (DAQ) is referred to as a run.

The arrival time of a particle in the DUT is given precisely by the intrinsically fast scintillator response. Space points of the particle track in several reference detectors allow a reconstruction of the particle trajectories and thus the intersection point of the particle in the DUT. To obtain the best hit prediction in the DUT (see chap. 6.1.3), the telescope planes are placed before and after the DUT. Besides the intrinsic resolution of the planes, the quality of the track reconstruction is affected by multiple scattering occurring in the different detector planes and in the air between. As the effect is inversely proportional to the particles energy, high energy particle beams are preferred for beam tests.

At CERN for the tests of particle detectors usually pions of 100 to 180 GeV/c are chosen where multiple scattering is negligible. Due to the preparation of the startup of the LHC, the CERN testbeams were not available in 2005. Part of the studies were thus carried out at DESY[1]. The electron and positron beams provided at the DESY testbeam facility have a maximum energy of 6 GeV. The most commonly used energy is 4 GeV. At this energy the effects of multiple scattering play a major role.

6.1 Track reconstruction and alignment

The particle tracks are reconstructed from the hits recorded with the reference detectors of the telescope system. Therefore, the hit positions as well as the position of the planes have to be determined as precisely as possible. For detectors with resolutions in the order of μm usually the positions and orientations of the detectors in space are not known well enough from the survey of the setup. The alignment of the detector planes thus has to be reconstructed by using the tracks themselves. To accomplish this task the *Silab Testbeam Analysis* (SiTBeAn) software package has been developed in C++ and Python. It uses the ROOT[2] framework and is based on ideas implemented in the *H8* software, which was written in Fortran and used previously for the data analysis of the ATLAS pixel testbeams.

6.1.1 Hit reconstruction

To determine the hit position from the response of a segmented detector several hit reconstruction methods are available. The most commonly used methods are the binary hit reconstruction and the η-algorithm.

Binary: The impact position is calculated by the average position of the segments showing a charge deposit above a certain threshold. If the detector shows no charge sharing, the charge deposit is always concentrated in one pixel. In this case, the uncertainty of the hit reconstruction is given by

$$\sigma_{bin} = \frac{\mathrm{x_{pitch}}}{\sqrt{12}}, \tag{6.1}$$

where x_{pitch} is the width of the segment [19]. Neglecting noise, the same result is obtained if only the segment with the highest charge deposit is used.

Including information of adjacent segments, the best resolution for digital readout is obtained if the combination of threshold and charge sharing (drift, incidence angle) is tuned in such a way, that the probability of double hits equals that of single hits. In this ideal case the error on the hit reconstruction is halved as the

[1] Deutsches Elektronen Synchrotron, Hamburg

[2] ROOT is an object-oriented software package developed by CERN for particle physics data analysis

single- and double-hit information can be used to effectively halve the pitch. The requirements on a binary readout system are less demanding than on a system which also obtain charge information. It simplifies the electronics and readout, but causes a loss in reconstruction power.

η-algorithm: The η-algorithm corrects for the non-linearities in the charge division and uses the relation between the charge sharing ratio and the impact position of the particle to improve the hit reconstruction [48]. The charge sharing ratio η and the position reconstruction in one dimension are defined using the two neighboring segments with the highest charge deposit, Q_{left} and Q_{right}:

$$\eta = \frac{Q_{left}}{Q_{left} + Q_{right}} \tag{6.2}$$

$$x_{pos} = x_{left} + X(\eta), \tag{6.3}$$

where $X(\eta)$ is the correlation function between the inter-segment position and the charge sharing ration. The shape of the relation is highly detector dependant but can be measured in case of homogeneous particle incidence and is given by

$$X(\eta) = x_{pitch} \int_0^{\eta} p(\eta')d\eta', \tag{6.4}$$

where $p(\eta)$ is the probability density derived from the measured distribution of η-values. The error on the hit reconstruction is

$$\sigma_x^2(\eta) = \left(\frac{\partial X(\eta)}{\partial \eta}\right)^2 \sigma_\eta^2 = x_{pitch}^2\, p(\eta)^2 \left(\frac{S}{N}\right)^{-2} \left(1 - 2\eta + 2\eta^2\right), \tag{6.5}$$

where S/N is the signal over noise value of the detector [49]. As can be seen, the error depends on the shape of the η-probability function and the η-value itself. Usually it is smallest in between two strips, where the charge sharing is biggest ($\eta \approx 0.5$) and the η-distribution is a flat valley. Assuming a totally flat η-probability function, corresponding to an ideally linear charge sharing, the average resolution is

$$\sigma = 0.812 \cdot\ x_{pitch} \cdot (S/N)^{-1}. \tag{6.6}$$

6.1.2 Track fitting and plane alignment

With alignment of the telescope we understand to determine the parameters of all detector planes from the hit positions recorded in the planes them self. The inherent problem behind is that tracks are needed to determine the plane parameters, while the plane parameters are needed to determine the tracks. While several software packages exist to address multi parameter optimization problems (e.g. MINUIT, Milipede), we chose to code the procedure into the tracking code directly. In the following the method chosen for the implementation is outlined. In the mathematical descriptions the coordinate system is chosen such that the z-coordinate points in beam direction.

Track fitting: Each plane of the telescope system contributes one space point for the track reconstruction. In absence of a magnetic field and neglecting interactions of the particles with the material of the detector planes, the trajectory of a particle is described by a straight line. A track is then given by

$$\hat{x}_t = \begin{pmatrix} \tan\Omega_y \\ \tan\Omega_x \\ 1 \end{pmatrix} z + \begin{pmatrix} \Delta_x \\ \Delta_y \\ 0 \end{pmatrix}, \tag{6.7}$$

where z is the position along the beam axis and the four parameters $\Delta_x, \Delta_y, \Omega_x$ and Ω_y are the offset and the slope describing the track in the coordinate system of the setup. If the positions of the telescope planes are known, tracking is the task to determine the best set of track parameters which fit the given set of space points. This translates to a linear least square problem which can be solved directly.

A problem only occurs if in the time window of an event more than one particle traverses the setup. In this case the assignment of a hit to a track is ambiguous. The easiest way to avoid this situation is by adjusting the test beam conditions. Otherwise more sophisticated methods are needed to resolve the ambiguities, for example the use of the arrangement resulting in the overall minimal residual for all possible tracks or by prearranging the hits based on already known spatial correlations.

Plane alignment: The 2-dimensional hit positions delivered by the detector planes have to be translated to 3-dimensional space coordinates representing the particle positions in the global coordinate system of the testbeam setup. For a plane this translation is fully defined by six parameters: three parameters $\Delta_x, \Delta_y, \Delta_z$ for the plane origin $\mathbf{t}$ and three angles $\Omega_x, \Omega_y, \Omega_z$ describing the orientation. The determination of the plane parameters is done by minimizing the differences (residuals) between the reconstructed hit positions in the device and the predicted hit positions from the intersections of the tracks with the plane. In the following the implementation in the software package is sketched.

The transformation from device-coordinates (non-hatted) to system-coordinates (hatted) is described by a combination of a rotation and a translation. The rotation in a three dimensional space itself can be composed out of three successive rotations around the three axis of the system:

$$\mathcal{R} = \mathcal{R}_x \cdot \mathcal{R}_y \cdot \mathcal{R}_z \tag{6.8}$$

$$= \begin{pmatrix} 1 & 0 & 0 \\ 0 & \cos\Omega_x & -\sin\Omega_x \\ 0 & +\sin\Omega_x & \cos\Omega_x \end{pmatrix} \cdot \begin{pmatrix} \cos\Omega_y & 0 & +\sin\Omega_y \\ 0 & 1 & 0 \\ -\sin\Omega_y & 0 & \cos\Omega_y \end{pmatrix} \cdot \begin{pmatrix} \cos\Omega_z & -\sin\Omega_z & 0 \\ +\sin\Omega_z & \cos\Omega_z & 0 \\ 0 & 0 & 1 \end{pmatrix} = \tag{6.9}$$

$$\begin{pmatrix} +\cos\Omega_y\cos\Omega_z & -\cos\Omega_y\sin\Omega_z & +\sin\Omega_y \\ +\cos\Omega_x\sin\Omega_z + \sin\Omega_x\sin\Omega_y\cos\Omega_z & +\cos\Omega_x\cos\Omega_z - \sin\Omega_x\sin\Omega_y\sin\Omega_z & -\sin\Omega_x\cos\Omega_y \\ +\sin\Omega_x\sin\Omega_z - \cos\Omega_x\sin\Omega_y\cos\Omega_z & +\sin\Omega_x\cos\Omega_z + \cos\Omega_x\sin\Omega_y\sin\Omega_z & +\cos\Omega_x\cos\Omega_y \end{pmatrix} \tag{6.10}$$

The full transformation including the translation is given by

$$\hat{x}_h = \mathcal{R}x_h + \mathbf{t}, \tag{6.11}$$

where the z component of the device coordinate x_h is usually zero, as the detector is a plane and already fully specified by x and y. With $\mathcal{R}$ being a rotation matrix, the back transformation is given by

$$x_h = \mathcal{R}^{-1}\left(\hat{x}_h - \mathbf{t}\right) = \mathcal{R}^T\left(\hat{x}_h - \mathbf{t}\right). \tag{6.12}$$

As can be seen from (6.10) the full rotation matrix is quite complex to calculate. An approximation for small angles is often sufficient. In this case the matrix significantly simplifies to

$$\mathcal{R} \approx \begin{pmatrix} 1-{\Omega_y}^2 & -\Omega_z & 0 \\ +\Omega_z & 1-{\Omega_x}^2 & 0 \\ 0 & 0 & 1 \end{pmatrix}. \tag{6.13}$$

To align a plane to a given set of tracks, first the predicted hit positions in the plane have to be determined. In our model they are given by the intersection point of the line representing the track with the plane representing the device. This point is given by

$$\mathbf{n}\cdot\left(\hat{x}_t - \mathbf{t}\right) = 0, \tag{6.14}$$

where $\mathbf{n}$ is the normal vector of the plane of interest (represented by the last row of the corresponding rotation matrix $\mathcal{R}$), $\mathbf{t}$ is the translation vector of the plane and the $\hat{x}_t$ the track as described by eq. 6.7.

The standard method to determine the parameters of a model is the method of least squares. It is used to find the set of parameters which gives the best fit between the measured data and the predictions of the model. The best fit is characterized by the sum of squared residuals having its smallest value. A residual is the difference between an observed value and the value predicted by the model.

$$\begin{aligned} r_i &= f_{meas,i} - f_{pred,i}\left(\mathbf{p_1},\ldots,\mathbf{p_n}\right) \\ &= f_{meas}(\alpha_i) - f_{pred}\left(\alpha_i,\mathbf{p}\right) \end{aligned} \tag{6.15}$$

$$S = \sum_{i=1}^{m} {r_i}^2 = \mathbf{r}^T\cdot\mathbf{r} \tag{6.16}$$

In the case of f_{pred} being a linear function of the parameter vector $\mathbf{p}$, the residuals of all measurements i can be expressed by a matrix equation

$$f_{pred}\left(\alpha_i,\mathbf{p}\right) = g_1(\alpha_i)\cdot p_1 + \ldots + g_n(\alpha_i)\cdot p_n = \sum_{j=1}^{n} g_j(\alpha_i)\cdot p_j \tag{6.17}$$

$$\mathbf{F} = \begin{pmatrix} g_1(\alpha_1) & \ldots & g_n(\alpha_1) \\ \vdots & \ddots & \vdots \\ g_1(\alpha_i) & \ldots & g_n(\alpha_i) \end{pmatrix} \tag{6.18}$$

$$\mathbf{r} = \mathbf{f}_{meas} - \mathbf{F}\cdot\mathbf{p}. \tag{6.19}$$

The optimal parameter set is given by [50]

$$\mathbf{p} = \left(\mathbf{F}^T\mathbf{F}\right)^{-1}\mathbf{F}^T\,\mathbf{f}_{meas}. \tag{6.20}$$

The expressions given above are based on the implicit assumption that all measurements are uncorrelated and have equal uncertainty. If this is not the case, a modified approach must be adopted for which the best estimate for the parameter values is given by

$$\mathbf{p} = \left(\mathbf{F}^T \mathbf{W} \mathbf{F}\right)^{-1} \mathbf{F}^T \mathbf{W} \, \mathbf{f}_{meas}; \quad W_{ij} = \delta_{ij} \frac{1}{{\sigma_i}^2}, \tag{6.21}$$

where $\mathbf{W}$ is the weighting matrix. Still assuming no correlations between the measurements the weighting matrix is diagonal and given by the variances σ_i^2 of the corresponding measurements.

Due to the nature of the rotation matrix the plane alignment is a highly nonlinear least square problem and f_{pred} is not a linear function of $\mathbf{p}$. In this case there is no closed solution to determine the best set of parameters. Instead the best parameters must be obtained by successive approximation:

$$\mathbf{p}^{k+1} = \mathbf{p}^k + \Delta\mathbf{p} \tag{6.22}$$

For each iteration values of $\Delta\mathbf{p}$ are found for which $S(\mathbf{p}^{k+1}) < S(\mathbf{p}^k)$ until the sum of the least squares has approached its minimum and $S(\mathbf{p}^k) - S(\mathbf{p}^{k+1}) < \epsilon$, a predefined abort value. In each iteration the model can be linearized by a first-order Taylor series expansion about $\mathbf{p}^k$. Then $\Delta\mathbf{p}$ is calculated in analogy to the linear problem.

$$f_{pred}\left(\alpha_i, \mathbf{p}^k + \Delta\mathbf{p}\right) = f_{pred}\left(\alpha_i, \mathbf{p}^k\right) + \sum_{j=1}^{n} \frac{\partial f_{pred}\left(\alpha_i, \mathbf{p}^k\right)}{\partial p_j} \cdot \Delta\mathbf{p} \tag{6.23}$$

$$\mathbf{F} = \begin{pmatrix} \frac{\partial f_{pred}\left(\alpha_1, \mathbf{p}^k\right)}{\partial p_1} & \cdots & \frac{\partial f_{pred}\left(\alpha_1, \mathbf{p}^k\right)}{\partial p_n} \\ \vdots & \ddots & \vdots \\ \frac{\partial f_{pred}\left(\alpha_i, \mathbf{p}^k\right)}{\partial p_1} & \cdots & \frac{\partial f_{pred}\left(\alpha_i, \mathbf{p}^k\right)}{\partial p_n} \end{pmatrix} \tag{6.24}$$

$$\Delta\mathbf{f} = \left(\mathbf{f}_{meas} - \mathbf{f}_{pred}(\mathbf{p}^k)\right) \tag{6.25}$$

$$\Delta\mathbf{p} = \left(\mathbf{F}^T \mathbf{F}\right)^{-1} \mathbf{F}^T \, \Delta\mathbf{f} \tag{6.26}$$

This method is commonly known as the Gauss-Newton algorithm. Another option is the method of deepest descent, sometimes referred to as the Cauchy algorithm. In this case $\Delta\mathbf{p}$ is determined by

$$\Delta\mathbf{p} = \lambda \cdot \nabla S(\mathbf{p}^k) = \lambda \cdot \mathbf{F}^T \, \Delta\mathbf{f} \tag{6.27}$$

where λ is an adjustable parameter defining the size of the step in the direction of the deepest descent. An algorithm combining features of the Gauss-Newton as well as from the Cauchy algorithm is the Levenberg-Marquardt algorithm:

$$\Delta\mathbf{p} = \left(\mathbf{F}^T \mathbf{F} + \lambda \cdot \mathrm{diag}(\mathbf{F}^T \mathbf{F})\right)^{-1} \mathbf{F}^T \, \Delta\mathbf{f}. \tag{6.28}$$

The (non-negative) damping factor λ is adjusted in each iteration. If the reduction of S is rapid, a smaller value can be used. This brings the algorithm closer to the Gauss-Newton method which works best in the region close to the minimum. If an iteration gives insufficient or no reduction in the residual, the value of λ is increased again. This moves the algorithm back in the direction of the deepest decent method which converges faster, but less precisely in the direction of the minimum. Various more or less heuristic arguments have been put forward in the literature for the best adjustment strategy of the damping parameter λ. In this thesis the strategy outlined in [51] was used and found to work.

It is worth to note, that the least square approach strives for a parameter set resulting in a mean residual of zero. This is what is wanted for ideal detectors where the residual distributions are symmetric. Inhomogeneous illumination, noise hits or wrongly assigned tracks lead to distortions which effect the symmetry of the residual distribution in real data and thus the minimization. As a consequence, only known good hits and tracks have to be used for the alignment. It also has to be remembered that all iterative methods converge in a local minimum only. Whether it is also the global minimum of the posed problem often depends on a good guess of the initial values.

Alignment of the entire telescope system: The problem in the alignment of the entire telescope system lies, as mentioned before, in the fact that the tracks are needed to align the planes while the plane positions are needed to obtain the tracks. The solution to cope with this problem is to start with a good guess either on the plane positions or on the tracks. Then the overall alignment is being improved by an iterative approach which aligns the planes and fits the tracks in turn.

The first guess on the plane parameters are the measured positions after the mounting of the detectors in the testbeam. Using no special surveying equipment the error on the parameters is in the order of $\pm 1^\circ$ and ± 1 mm, which has to be compared to the detector resolution of several μm. The divergence and slope of the particle beam is typically small compared to the resolution of the detectors even if considering the longitudinal dimensions of the setup. Therefore, a quite accurate track sample to start with is given by the hit positions in one fixed plane and straight lines with no slopes. Another consequence of the small beam divergence is that the alignment is quite insensitive along the beam direction. Therefore, although the z-positions of the detectors are still required, they are not required with high accuracy as their contribution to the error is small. Based on these assumptions an iterative approach is started:

1. To fix the coordinate system one of the planes is chosen as reference. Its parameters are fixed and not changed in any of the following steps. To fix the z-scaling the z-position of another plane has to be fixed in addition.

2. As the first track sample straight tracks without slopes through one of the telescope planes are chosen.

3. The planes are aligned to the given set of tracks.

4. A new track set is fitted from the updated hit positions.

5. The steps starting from step number 3 are repeated until the changes in the parameter values are below a defined abort value ϵ.

Verification of the alignment procedure: The alignment algorithms were verified with simulated data. Simulated tracks were used to calculate hit positions in the different detector planes. For the hit response these hit positions were smeared with a Gaussian to consider the finite detector resolution. The alignment procedure itself was verified by randomly changing the plane positions according to the expected uncertainties of the setup and observing the realignment success of the alignment code.

For real data generally asymmetries in the residual distributions occur, to which the least square based alignment methods are sensitive. The asymmetries originate from noise, dead channels, changes in the detector response depending on position and so on. Therefore, cuts have to be applied and refined during the iterations to finally obtain the best set of parameters.

The residual distributions as shown in figure 6.2 allow to visually verify the correct alignment of the detector. If the detector is properly aligned in the x- and y-direction, the mean of the corresponding residual distribution must be zero. A misalignment of the rotation angles can be identified through the change of the mean residual along the detector axis. While for a proper alignment the residuals stay constant, they show a slope otherwise (e.g. fig. 6.2(c)). The residual of y against the position in y is sensitive to a rotation around the x-axis, while the residual of x vs. x is sensitive to a y-axis rotation. Rotations around the z-axis become visible in the plots of the residual in y vs. x-position and of the residual in x vs. the y-position. Also the assumption of wrong pixel/strip sizes, which might have their origin in the fabrication tolerances of the sensors, results in artificial plane rotations. For large assumed pixel sizes are compensated by the scaling effect of an additional rotation. To small pixels cannot be compensated but result in rotation angles of zero degrees.

6.1.3 Track extrapolation onto the DUT

The precision of the track extrapolation in the plane of the device under test is limited by three effects: multiple scattering of the particles in the material of the setup (detector, air, etc.), the error on the fitted parameters of the track and the precision of the alignment.

Track fitting error: Uncertainties in the knowledge of the hit positions in the telescope planes propagate to an uncertainty in the predicted hit position from

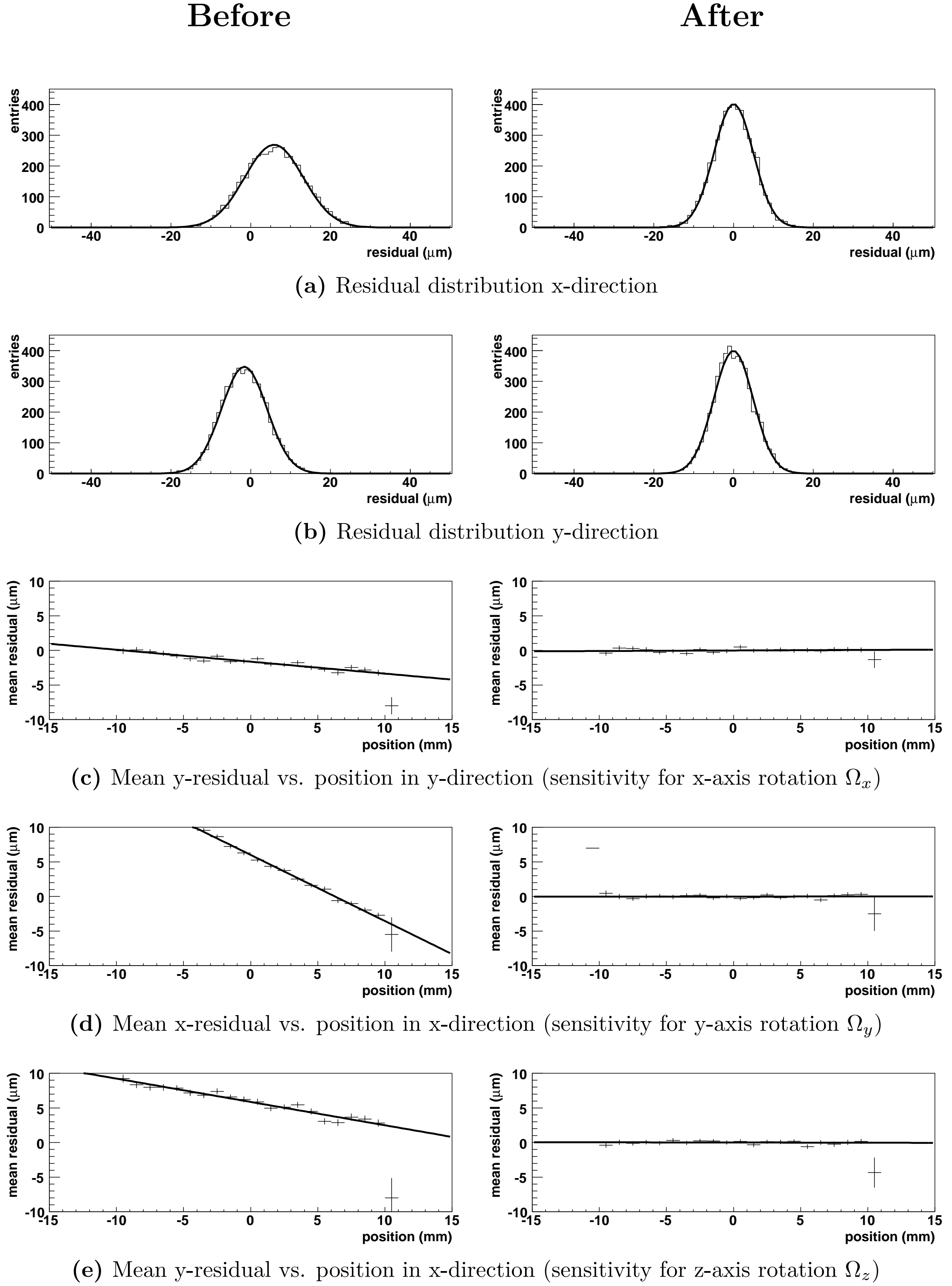

(a) Residual distribution x-direction

(b) Residual distribution y-direction

(c) Mean y-residual vs. position in y-direction (sensitivity for x-axis rotation Ω_x)

(d) Mean x-residual vs. position in x-direction (sensitivity for y-axis rotation Ω_y)

(e) Mean y-residual vs. position in x-direction (sensitivity for z-axis rotation Ω_z)

Figure 6.2: Residual plots for a device displaced by $\Delta x = 6\,\mu\text{m}$, $\Delta y = -1.5\,\mu\text{m}$, $\Delta z = 2\,\text{mm}$, $\Delta\Omega_x = -1.1°$, $\Delta\Omega_y = 2.5°$ and $\Delta\Omega_z = 0.02°$ before and after alignment (simulation of 5000 events for a DUT of 5 µm resolution).

the track extrapolation. The error for a DUT placed at the position z_{DUT} is then given by [50]

$$\sigma_{pred} = \sqrt{V[\text{offset}] + z_{DUT}^2 V[\text{slope}]} \tag{6.29}$$

$$V[\text{offset}] = \left(\sum_i \frac{1}{{\sigma_i}^2} \right)^{-1} \tag{6.30}$$

$$V[\text{slope}] = \left(\sum_i \frac{z_i^2}{\sigma_i^2} \right)^{-1} , \tag{6.31}$$

where σ_i and z_i are the respective plane resolutions and positions expressed in the weighted center of mass system characterized by $\sum_i {\sigma_i}^{-2} z_i = 0$. Consequently the error is minimal at the position $z_{DUT} = 0$, where it is only limited by the resolution of the telescope planes themselves and independent of their absolute spacing.

If the hit position of the device under test is included in the fit, the predicted and measured hit positions are correlated. As a result, the observed variance of the residual distribution is reduced by the variance of the track prediction. In the other case of not including the hit position of the device under test, the error of the track prediction adds up to the intrinsic resolution of the device.

Multiple scattering: Besides the intrinsic resolution of the telescope devices, the effect of multiple scattering adds up to the uncertainty in the hit positions in the telescope planes. While traversing a medium charged particles are deflected by many small-angle scatters due to Coulomb interactions with the nuclei. For small angles the distribution is roughly Gaussian and the angular spread is giv1;5Ben by:

$$\Theta_0 = \frac{13.6\,\text{MeV}}{\beta c p} z \sqrt{\frac{x}{X_0}} \left[1 + 0.038 \ln \left(\frac{x}{X_0} \right) \right] , \tag{6.32}$$

where p, βc and z are the momentum, velocity and charge number of the incident particle respectively. The thickness of the scattering medium is given by x, while X_0 is the radiation length of the medium as defined in chap. 3.1. The effect of multiple scattering can be incorporated in the hit resolution of the different detector planes and thus directly affects the track extrapolation error as illustrated in fig. 6.3. If the effects of multiple scattering limit the precision of the predicted position it is best to place the DUT as close as possible to one of the telescope planes.

Alignment error: The uncertainties in the plane positions obtained after the alignment add up to a systematic error on the predicted hit position. Unlike the previously mentioned errors, the alignment error is the same for all events, but might vary depending on the position. Usually it is small compared to the precision of the predicted position.

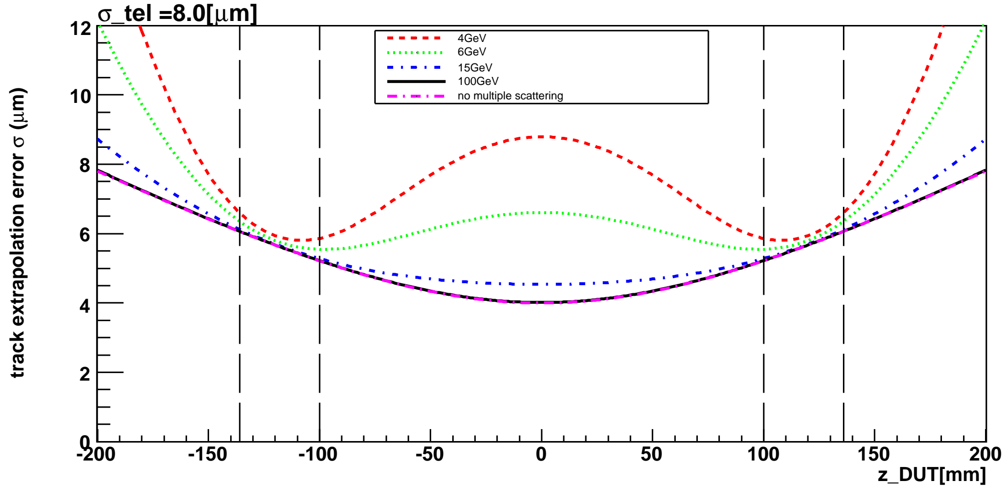

(a) telescope plane resolution of 8 µm

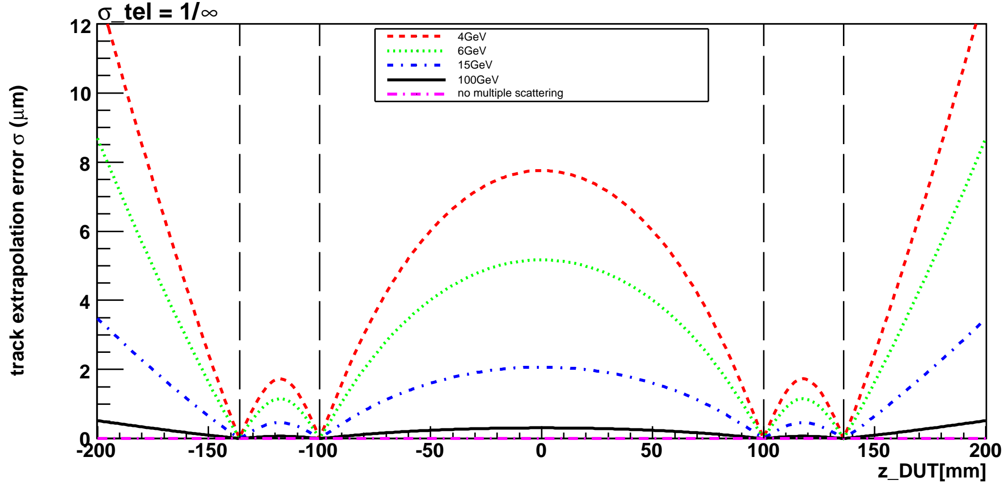

(b) infinite telescope resolution

Figure 6.3: Track extrapolation error for a DUT as a function of its position in z for various beam energies. Telescope planes are located at the positions indicated by the vertical lines. The DUT is assumed to equal 500 µm thick silicon while the telescope planes are considered massless.

6.2 The telescope modules

In the testbeam setup detector modules from the Bonn Atlas Telescope (BAT) were used as reference planes [52]. Each module represents one plane of the reference system and contributes with one point to the track reconstruction. Figure 6.4 shows a picture of a BAT module.

Figure 6.4: Picture of a Bonn Atlas Telescope Module (BAT) [53]

The sensor is a Hamamatsu[3] double-sided silicon strip detector with a pitch of 50 µm without intermediate strips. It has a thickness of 300 µm. The strips on the two sides are arranged perpendicularly to each other and made by n-implants on one side and p-implants on the other side (in the following referred to as n- and p-side). Each side contains a total of 640 strips which cover a sensitive area of $32 \times 32\,\mathrm{mm}^2$. For the readout of a side five VA2 ICs from IDEAS[4] are used. Each of the chips features 128 low noise and low power charge sensitive preamplifier-shaper circuits with simultaneous sample and hold, a daisy-chainable serial analog output and additional calibration features. The analog current output is translated to a voltage by a transimpedance amplifier and digitized with a 12 bit ADC. For the system control, event building and data transfer an FPGA-based digital card is included in the module.

Beside an external power supply for the sensor bias and the operating voltages no additional hardware is needed. The connection to the DAQ system is done via a proprietary digital system bus to the DAQ system (Blue Board Bus). For details on the modules and telescope DAQ see [53] and [54].

A specialty of the BAT modules is the zero-suppressed readout mode. Threshold settings for each strip can be uploaded to the module. The digital logic then detects the strips containing hit information and only transfers this charge information plus those of two neighboring strips on either side. This ensures a readout of the full hit information. The benefit of the zero-suppressed readout is the reduced data size which minimizes storage, transfer bandwidth and, as a consequence, system dead time. The drawback is the loss of non-hit strip information in the data which

[3]Hamamatsu Photonics Deutschland GmbH
[4]Gamma Medica-Ideas, Inc. (Norway)

is needed for the sensor characterization and event based signal correction. This information has to be provided separately.

For a single event, the output signal *out* digitized by the ADC of a strip can be decomposed in three components:

$$out = ped + noise + q, \tag{6.33}$$

where *ped* is a fixed offset originating from the sensor leakage current and the readout electronics (pedestal), noise is the individual noise of one strip together with the common noise induced by the environment and, in presence of a passing particle, q, the deposited charge in the sensor. In the following the characterization is shown for one module using data of the October 2006 testbeam period. The other modules used in the telescope system behave similarly.

Noise and Pedestals: The strip noise and pedestal values are measured by sampling the strip signal in absence of signal charge. The strip pedestal corresponds to the mean signal while the variance characterizes the noise of the strip. As the zero-suppressed data contains no strip information without a signal component, a special characterization measurement is carried out at the beginning of each run. For each strip the output is subsequently sampled one hundred times and the mean and RMS values are stored as preamble to a data taking run. Figure 6.5 shows the results of these noise and pedestal measurements in units of ADC counts, further referred to as ADU.

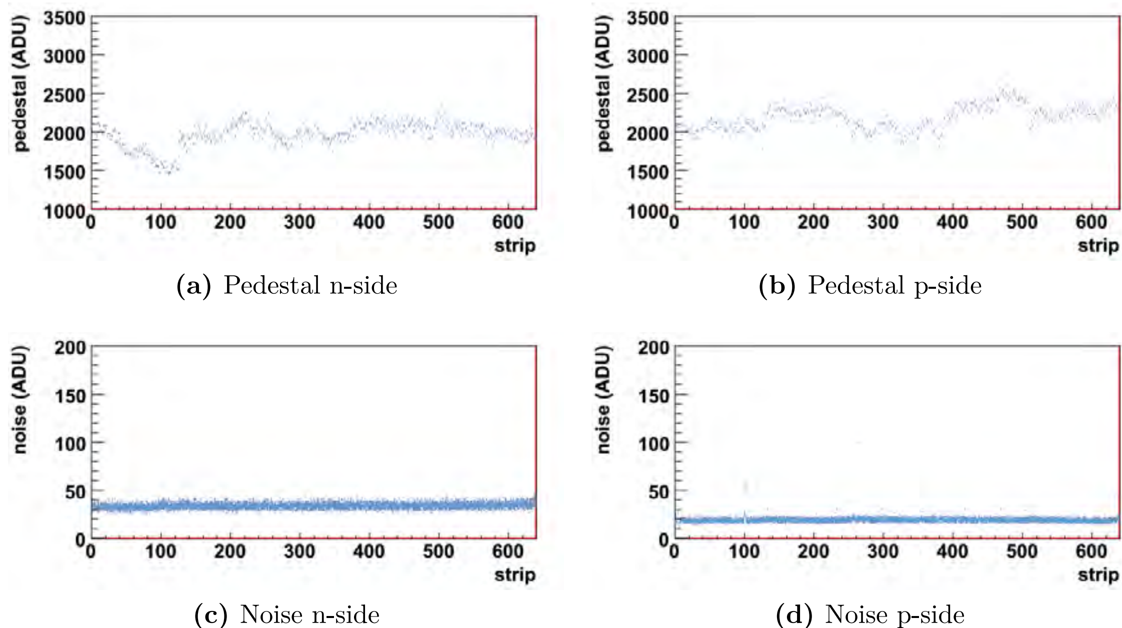

(a) Pedestal n-side

(b) Pedestal p-side

(c) Noise n-side

(d) Noise p-side

Figure 6.5: Distribution of the strip pedestal and noise values measured at the beginning of each run

The pedestals are differing from strip to strip, but in general no common pattern or structure is observed. There is only a slight dependence on the readout chip visible (multiples of 128 strips). The typical noise of a strip, depending on the module, is between 27 ADU and 36 ADU for the n-side and around 19 ADU for the p-side.

Looking more closely into the distributions of fig. 6.5(c-d), one sees, that sporadically a noise value deviates from the usually observed noise of a strip. Most likely this is not related to an increase in system noise itself, but due to an irregularity during the noise measurement. For a verification, the data itself where used for a noise and pedestal measurement regardless of the zero suppression. For part of the events this is possible as the signal charge, as shown later, is rarely spread over more than three strips while at least five strips are read out. If the particles hit the center region between two strips, the outermost strips represent the sampling of strips without signal. With this data a crosscheck of the results obtained from the characterization measurements is possible in the region of the beam. In fig. 6.6 the correlations of the noise values obtained from the initial characterization measurement and from the run data are shown. They clearly support the previously mentioned suspicion.

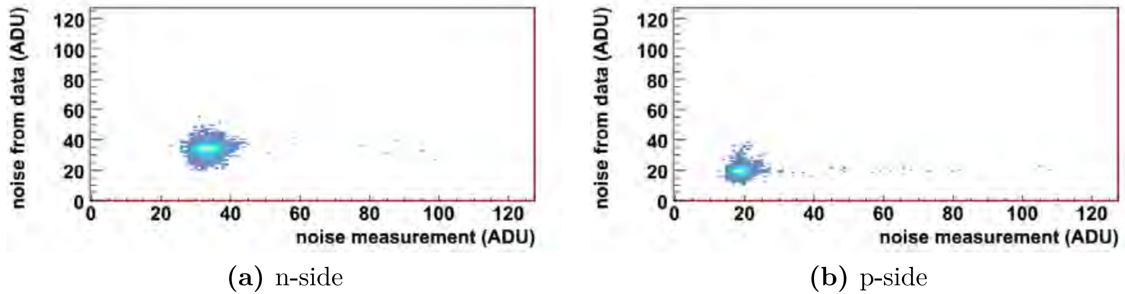

(a) n-side **(b)** p-side

Figure 6.6: Correlation of the noise values obtained from the initial measurement and from the run data

To compensate for the wrong noise measurements, the mean noise of each strip was calculated while discarding 5% of the data at both edges of the distribution. The same method was used to determine the pedestal values, even if they are more robust to the observed distortions than the noise measurement.

The variation of the pedestals as a function of the run number and thus in time is shown for strip no. 320 (plane center) in fig. 6.7. No obvious time dependence is observable. This stability is important as the pedestals are automatically subtracted during data taking and hence influence the hit detection using zero-suppression. The fluctuation of the mean pedestal is typically less than 4 ADU and thus in the order of the expected statistical fluctuation for a mean measurement using 100 samples ($2-3$ ADU). The pedestal fluctuations are very small compared to the strip noise and the mean pedestal can be used in good approximation for the whole analysis.

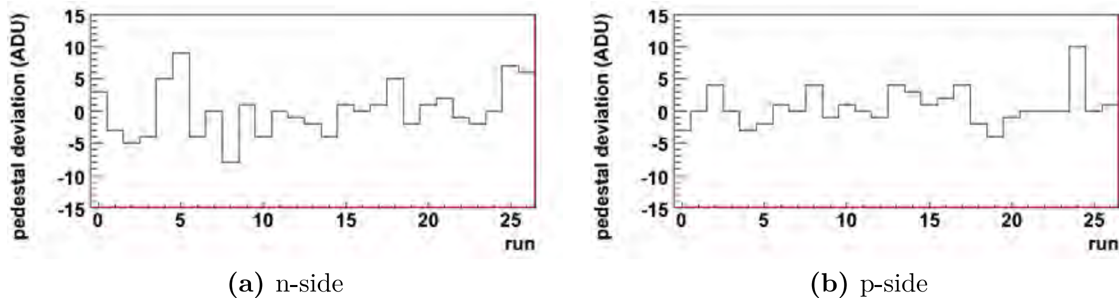

(a) n-side **(b)** p-side

Figure 6.7: Pedestal deviation from the mean for strip no. 320 as a function of the run number (time)

Hit identification, clustering and charge collection properties: A particle hit in the detector has to be identified by its charge deposit in the sensor. The *seed* of the charge deposition is found by selecting the highest strip entry in a continuous region of hits above the threshold. The threshold is predefined internally by the modules zero suppression and was 256 ADU. The pedestal subtracted seed signal distributions are shown in fig. 6.8(a,b). They have a Landau shape, show a broadening to the left side due to charge sharing between several adjacent strips and have a low side signal cutoff caused by the threshold of 256 ADU.

As discussed previously, the signal fluctuation (noise) of a strip is usually lower than 36 ADU for the n-side and 18 ADU for the p-side. A threshold setting of 256 ADU thus complies to a 7σ cut for the n-side and a 14σ cut for the p-side. To ensure at least a 5σ cut also for more noisy strips, an additional software cut was included in the seed selection. In addition all strips with a noise larger than 80 ADU were excluded. This cuts make it for the seed strip signal very unlikely to be a fake signal originating from the system noise.

To account for the charge sharing, all adjacent strips with a significant signal entry were considered to originate from a single particle and combined to a single cluster. The neighbor cut was set to three times the noise value. Due to the lower noise of the p-side the average cluster size is larger than on the n-side. The corresponding cluster charge and size distributions are shown in fig. 6.8(c-f). As can be seen, the charge is rarely spread over more than three strips. The most probable charge deposit is 815 ADU on the n-side and 789 ADU on the p-side. The signal to noise value for the n-side is in the order of 20 ADU and for the p-side in the order of 40 ADU.

The charge distributions in fig. 6.8(c-d) show charge entries at the left and right outside of the expected (fitted) Landau distribution. They most likely originate from noise, a scattered or secondary particle or an interaction taking place in the sensor. As they do not originate directly from a beam particle incident, they are useless and even disadvantageous for a precise track reconstruction and have to be suppressed. Limiting the hit identification to the region given by the scintillator excludes already most of the secondary particles as they usually do not travel in

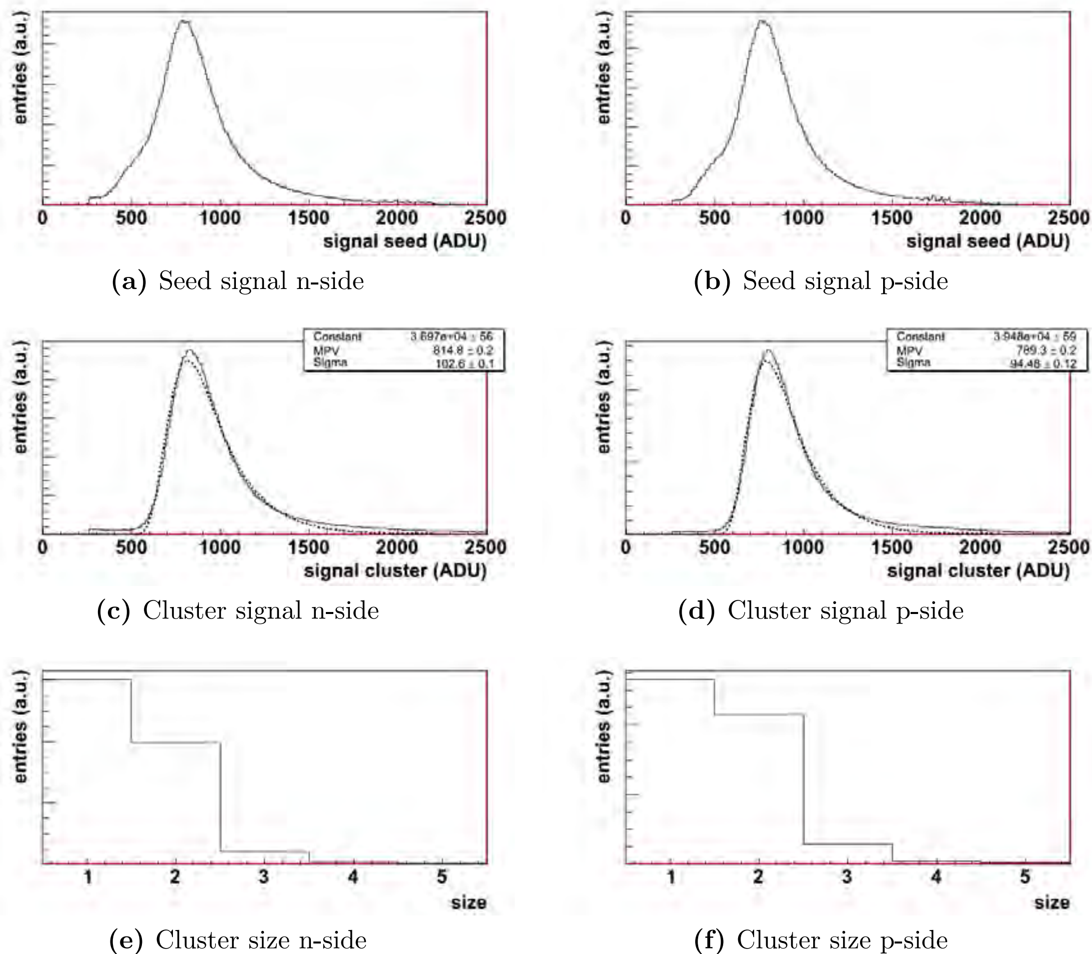

(a) Seed signal n-side

(b) Seed signal p-side

(c) Cluster signal n-side

(d) Cluster signal p-side

(e) Cluster size n-side

(f) Cluster size p-side

Figure 6.8: Seed signal, cluster signal and cluster size distribution as obtained from the modules raw data stream.

parallel to the beam particles. In addition the beam conditions were adjusted such that predominantly single particles crossed the detectors at a time. Besides the effect that this avoids the ambiguity problem of a strip detector, it also implies that a second hit in the detector is very likely originating from a $\delta-$electron, an interaction or from common noise disturbances. The same is true for clusters with a size bigger than two. In all these cases no precise hit position reconstruction is possible. As a consequence, all events with more than one hit and cluster sizes larger than two were discarded. Figure 6.9 shows the signal distribution of the hits considered for reconstruction. It nicely follows a Landau shaped distribution.

The BAT modules show a dependence of the charge signal on the strip number which is particularly pronounced at the chip edges at multiples of 128 strips (fig. 6.10). This originates from gain variations in the chip amplifiers and has to be dealt with during the charge sharing based hit reconstruction.

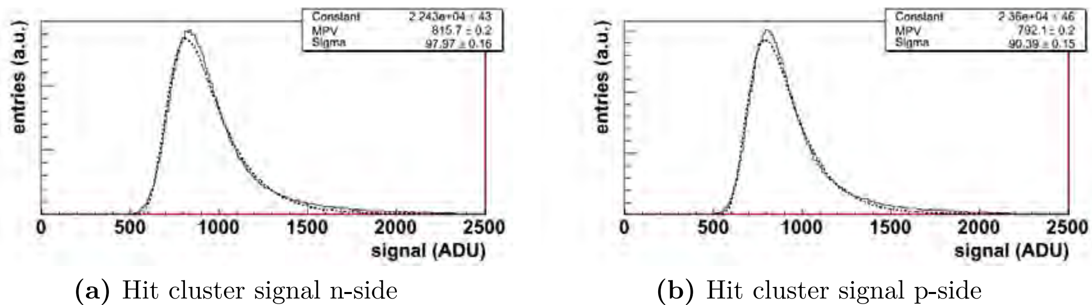

(a) Hit cluster signal n-side **(b)** Hit cluster signal p-side

Figure 6.9: Cluster signal of the events considered for hit position reconstruction.

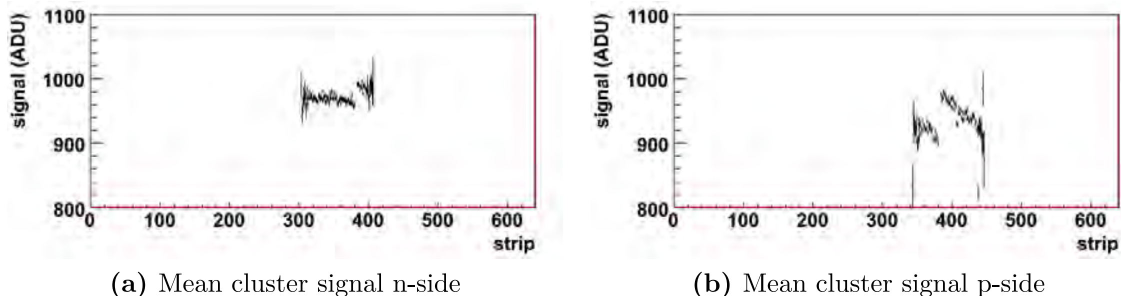

(a) Mean cluster signal n-side **(b)** Mean cluster signal p-side

Figure 6.10: Strip dependence of the mean cluster signal. The chip edges stand out at multiples of 128 strips. Only the region illuminated by the beam and selected for triggering is shown.

Hit position reconstruction and resolution: The hit positions are reconstructed based on the η-method described in 6.1.1. As an example, fig. 6.11 shows the average η-probability distribution and the η-correction function for the n-side of a module. The η-distributions extend to values below zero and above one as the system noise allows for negative charge signals. The η-probability function is periodic and the values below zero and above one can be treated correctly by folding them inside. Most of the hits show only a small or negligible charge sharing

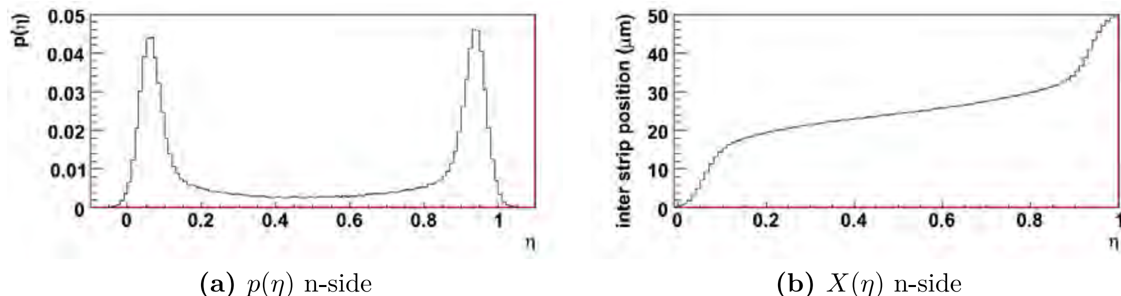

(a) $p(\eta)$ n-side **(b)** $X(\eta)$ n-side

Figure 6.11: η-probability function $p(\eta)$ and η-correction function $X(\eta)$ for the n-side of a module.

($\eta < 0.1$ or $\eta > 0.9$) as already expected from the cluster size distributions. The region of reasonable charge sharing ($0.1 < \eta < 0.9$) is limited to the region of about 15 μm between two strips. This is where the module has the best hit reconstruction precision. In the other region, around the center of a strip, the resolution is worse. Both conclusions result directly from the hit reconstruction error given by eq. 6.5. In fig. 6.12(a) the difference between the reconstructed hit position and the hit position predicted by using the hit positions of the remaining telescope planes is shown. The two classes of hit reconstruction accuracy become visible as indicated by the double Gaussian fit.

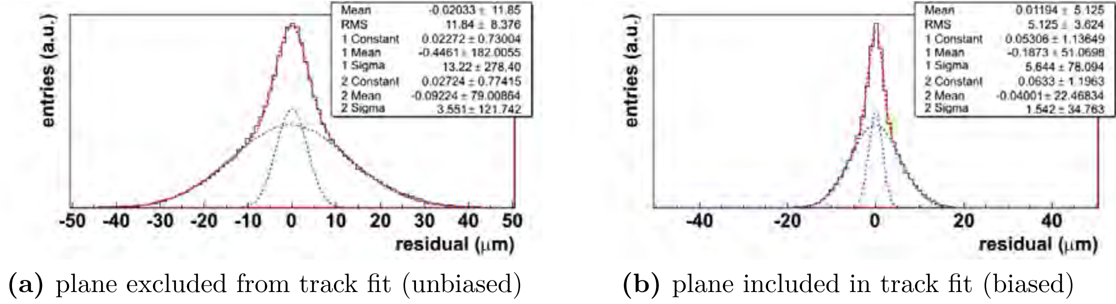

(a) plane excluded from track fit (unbiased) **(b)** plane included in track fit (biased)

Figure 6.12: Residual distributions of the n-side of BatModule3

The RMS (sigma) value obtained from fig. 6.12(a) reflects the intrinsic resolution of the plane plus the track prediction error. If one includes alternatively the plane under study in the track fit for the hit prediction one obtains the residual distribution shown in fig. 6.12(b). The distribution gets narrower, as in this case the RMS (sigma) value reflects the intrinsic resolution of the plane minus the track prediction error. Using the RMS values obtained by these residual plots and calculating the track prediction error as described in section 6.1.3, the intrinsic resolution of a BAT module can be determined to be in the order of $8 - 10$ μm. The resolution obtainable in the DUT for the four plane telescope system is thus in the order of $4 - 5$ μm (See also fig. 6.3).

7 Characterization and Calibration of ATLAS Pixel Devices

7.1 The TurboDAQ test system

The test system used for the characterization of the pixel devices is the so-called *TurboDAQ* set-up (fig. 7.1), developed at the LBNL[1] in Berkeley. The hardware consists of two custom made boards called TPLL[2] and TPCC[3].

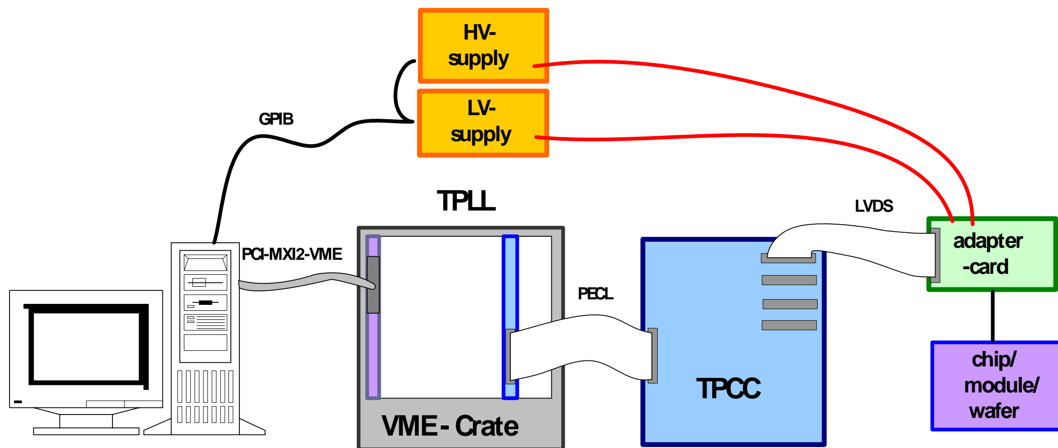

Figure 7.1: Sketch of the TurboDAQ test system [55].

The TPLL generates all control signals needed to operate the devices and provides the external trigger interface. It also contains a buffer for the incoming hit data and an FPGA[4] in which part of the control and data processing procedures are implemented in hardware. This is necessary to cope with the maximum data rate of 160 MBps for a 16-chip module. The pixel-modules or single-chip-assemblies are connected to the TPLL via the TPCC. The TPCC adapts signal levels, adjusts signal propagation delays and multiplexes the connection to up to four different devices. The connected devices can be operated and controlled in parallel, but the processing of the hit data is only possible for one selected device

[1]Lawrence Berkeley National Laboratory
[2]Turbo Pixel Low Level card
[3]Turbo Pixel Control Card
[4]Field Programmable Gate Array

at a time. The entire setup is connected to the measurement PC via a VME-bus[5]-interface and controlled by the TurboDAQ application. The software provides the functionality needed to configure and operate the devices and to write the output data stream to storage. In addition it allows direct access to all chip registers and contains automated procedures to characterize the devices and adjust the variable chip parameters.

For the testbeam measurements the TurboDAQ setup has been included in the testbeam control and data acquisition. Additional modifications were needed to operate several ATLAS devices with corresponding TPLL/TPCC pairs with one DAQ PC.

7.2 Calibration and adjustment of the front-end chip

The hit detection threshold and the ToT charge readout has to be tuned to the required operation parameters. This is done for each pixel individually with the chip internal, calibrated charge injection circuit.

Threshold adjustment: Only pixels with a charge deposit above threshold are considered for readout by the electronics of the pixel chip. The thresholds are set by a global chip threshold DAC (GDAC) and individual pixel threshold DACs (TDACs). The latter allow a fine tuning and a compensation of pixel-to-pixel variations.

The threshold of a pixel for a given GDAC/TDAC setting is obtained by measuring the fraction of detected hits as a function of the injected charge. In the ideal case the discriminator response is a step function. In reality the noise of the system leads to a smearing and the measurement is described by a complementary error function (Erfc):

$$P_{hit}(Q) = \frac{1}{2} Erfc\left(\frac{Q_{thresh} - Q}{\sqrt{2} \cdot \sigma_{noise}}\right) := \frac{1}{\sqrt{\pi}} \int_0^\infty \exp\left(\frac{Q - Q_{thresh}}{\sqrt{2} \cdot \sigma_{noise}}\right) dQ, \qquad (7.1)$$

where Q_{thresh} is the discriminator threshold and σ_{noise} the noise of the system. The result of such a measurement is shown in fig. 7.2. The discriminator threshold corresponds to the charge where 50% of the injections cause a hit. Usually the threshold scans are carried out with the chips C_{low} charge injection capacity.

The GDAC and TDACs for the desired threshold are obtained by first selecting the GDAC value which roughly corresponds to the threshold and then finding the TDAC which fits best for each pixel. This is done by measuring either all or interpolating between several discrete TDAC settings. If only the GDAC is used to set the threshold, the pixel-to-pixel variation of the thresholds for a module is found to be about 700 e [43]. By using also the TDACs, the threshold variation can be reduced to $40 - 60$ e [46]. Both values have to be compared to the desired thresholds of approximately 3000 e.

[5] Versa Module Eurocard-bus, multi user computer bus, standardized as ANSI/IEEE 1014-1987

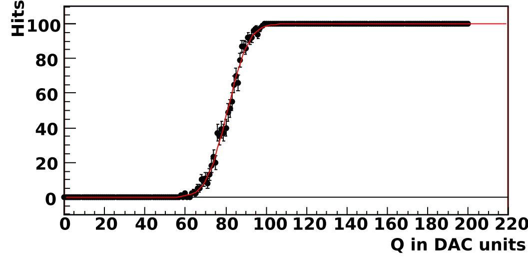

Figure 7.2: Illustration of a threshold measurement.

ToT-adjustment and calibration: The FE-I3 chip is optimized for a zero-suppressed, digital readout and not for a precise measurement of the collected signal charge. The "analog" measure of the charge is given by the signal time over threshold (ToT), as explained in chapter 5.

To get a homogeneous ToT response for all pixels, the feedback current (IF) can be adjusted similarly to the threshold tuning, but with less accuracy. The chip-average feedback current is set by the IF DAC, while the pixel-to-pixel variation can be minimized with the help of the individual FDACs. The standard tuning aims for a ToT of 30 for a charge of 20 ke, which is the most probable charge deposit of a particle in the ATLAS pixel silicon sensor. Given the standard threshold of 4000 e, this corresponds to a charge of about $500 - 600$ e per ToT unit. With a tuning for a lower feedback current (at the cost of a longer pixel dead time) charge resolutions in the order of $200 - 300$ e are possible.

The calibration of ToT values to electrons is done by injecting charges of known amount and characterizing the ToT response [43]. In theory the relation between the charge in electrons and the ToT value is linear. Unavoidable unlinearities in the analog part of the front-end chip, however, lead to deviations, especially for values close to the threshold. The relation is best expressed by the three parameter function

$$ToT = P_1 + \frac{P_2}{P_3 + Q_{inj}}. \tag{7.2}$$

It adequately describes the relation between ToT and charge except for low ToT values ($\lesssim 10$). It has been found, that for the calibration the C_{high} injection suits best. However, the charge calibration uncertainty is in the order of 10% and usually underestimates the meassured charge [55].

7.3 Measurements for sensor characterization

The characterization of the sensor is focused on two aspects: the detection efficiency of a particle transition and the position reconstruction from the obtained signals. Both aspects are directly correlated to the amount of charge collected in the sensor and how that charge compares to the noise of the system. For the posi-

tion reconstruction also the characteristics of the charge sharing between adjacent pixel cells is important. Additional aspects of interest are the quality of the bump connection between sensor and chip, the amount of dead channels and how the assembly procedure affected the performance of the sensor.

Noise measurements: The noise of the pixel readout is obtained from a threshold scan as outlined before. The dominant contribution to the system noise comes from the amplifier and depends on the pixel capacitance and leakage current [14]. The typical noise of an ATLAS pixel module tuned to a threshold of 4000 e is 180 e. The bare chip, missing the input capacity of a sensor, can be operated at a threshold of 1700 e with a noise of about 130 e.

Tests with radioactive sources: Tests with radioactive sources are especially useful to characterize the bump connections and to compare the performance between the individual pixel cells of a sensor. Bad sensor pixels or sensor-to-chip connections become directly visible in pixel-to-pixel count rate variations if the sensor is homogeneously illuminated.

For tests of silicon sensors of around 200 µm thickness an ^{241}Am-source is favorable, as the dominant 60 keV γ-emission is comparable to the most probable energy deposit of a MIP. The γ-emission is absorbed predominantly by the photo effect and the fixed charge deposit allows a cross check of the ToT calibration.

In the case of diamond sensors, the charge deposit of a γ-photon with comparable energy deposit of a MIP does not show a clear calibration peak as in silicon. Due to the lower atomic mass of diamond, the absorption is dominated by Compton scattering. In addition, the limited charge collection distances of poly-crystalline diamond makes the charge collected on a pixel electrode dependent of the origin of the photon conversion. Charge produced close to a pixel electrode has a higher chance to reach the electrode than charge from photons converted further away. While this does not affect the identification of pixel-to-pixel variations, it makes the quantification of the charge collection and a cross check of the ToT calibration by means of a source practically impossible.

Tests in a particle beam: While in the real experiment secondary particles from a collision traverse the sensors, in beam tests these are particles from an accelerator beam showing similar characteristics. In combination with a reference system (chap. 6) this allows to study the sensor response in dependence of the impact position of the particle. In particular this allows the measurement of the detection efficiency, the charge collection and the accuracy of the hit reconstruction in dependence to the relative position inside a pixel cell.

Detection efficiency

The detection efficiency ε is the probaility to detect a particle crossing the detector and defined as

$$\varepsilon = \frac{k}{n}, . \tag{7.3}$$

where k is the number of detected particles if n particles cross the detector. The difficulty to determine ε to high accuracy by measuring n and k in an experiment arises from the fact, that the precision of "there is a particle", "a hit is detected" and the error on the fraction of k over n is limited by statistical and systematic effects.

Predicting a hit: To predict a hit in the DUT the track extrapolation from the telescope system is used. Not for all particle transitions a good track reconstruction is possible. For example if the particle got heavily scattered of the original trajectory or if a secondary particle or noise hit is included in the track fit. These tracks can be excluded by setting a cut on the quality of the track fit (χ^2). Nevertheless, the hit prediction is only possible within the accuracy of the track reconstruction. For the used telescope system it is in the order of $4-5\,\mu$m (chap. 6). Assuming a Gaussian shape, 0.1% of the particles will hit the sensor more than $\pm 15\,\mu$m (3.3σ) away from the predicted position. Therefore, also hits detected in an adjacent pixel of the predicted one have to be considered to originate from the particle transition.

Detecting a hit: A particle is considered detected if the charge deposit in the sensor is above a certain threshold. The threshold is set by making a compromise between missing a particle and wrongly identifying noise as a particle. For the expected Landau shaped charge deposit this usually means setting the threshold below the lower edge of the distribution. Depending on the charge collection properties of the sensor, the lowest charge deposit from a particle might already be in the order of the noise.

Statistical error: To quantify the statistical error on the efficiency measurement, the value of interest is the variance of the efficiency provided that a measurement of n samples yields k detections ($V[\varepsilon]|_{k,n}$). For a calculation often a "Poissonian" or "Binomial" approach is used. The "Binomial" approach starts from the well known variance of the number of detections if the efficiency is provided, namely $V[k]|_{\varepsilon,n} = n\,\varepsilon\,(1-\varepsilon)$. One assumes then, that the true efficiency ε is very close to the expectation value $\hat{\varepsilon} = k/n$ from the measurement. It is:

$$V[\varepsilon]|_{k,n} \approx V[\hat{\varepsilon}]|_{k,n} \approx \frac{1}{n^2} V[k]|_{\varepsilon,n} = \frac{n\,\varepsilon\,(1-\varepsilon)}{n^2} \approx \frac{n\,\hat{\varepsilon}\,(1-\hat{\varepsilon})}{n^3} = \frac{k\,(n-k)}{n^2} \tag{7.4}$$

Unfortunately this assumption is particularly wrong in the most interesting cases of ε being close to one or zero. The correct way to handle the calculation of the statistical errors as described in [56, 57] is summarized as follows.

Required is the probability of having an efficiency ε if the measurement of n events gives k detections. The probability distribution can be derived from the Binomial probability distribution with the help of Bayes' Theorem. Mathematically it is given by the following expression:

$$P(\varepsilon|k,n) = (n+1)\binom{n}{k}\varepsilon^k(1-\varepsilon)^{n-k} \tag{7.5}$$

$$= \frac{(n+1)!}{k!\,(n-k)!}\,\varepsilon^k(1-\varepsilon)^{n-k} \tag{7.6}$$

From equation 7.6 one can directly calculate the most probable value $\varepsilon_{m.p.}$, the mean value $\langle\varepsilon\rangle$ and the variance $V[\varepsilon]$:

$$\varepsilon_{m.p.}|_{k,n} = \frac{k}{n} \tag{7.7}$$

$$\langle\varepsilon\rangle|_{k,n} = \frac{k+1}{n+2} \tag{7.8}$$

$$V[\varepsilon]|_{k,n} = \frac{(k+1)\,(k+2)}{(n+2)\,(n+3)} - \frac{(k+1)^2}{(n+2)^2} \tag{7.9}$$

The difference between the "Binomial" error obtained from eq. 7.4 and the "Bayesian" error from eq. 7.9 is illustrated in fig 7.3. While the "Binomial" error vanishes for the situation of reaching absolute or zero efficiency, the "Bayesian" error reaches a finite value.

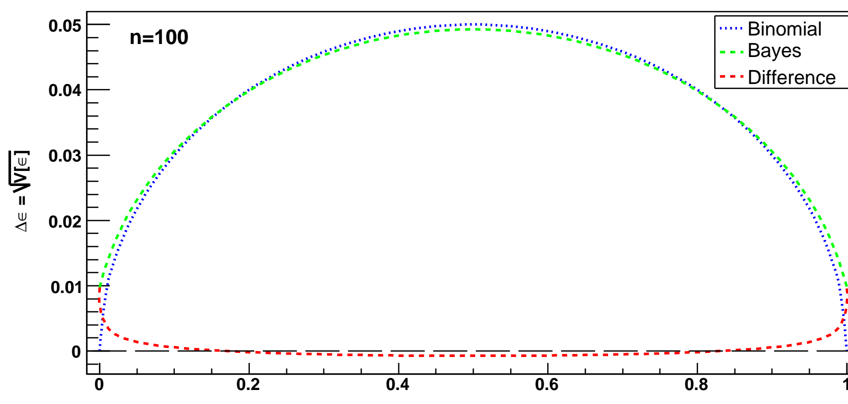

Figure 7.3: Comparison between the "Bayesian" and the "Binomial" treatment of the variance of an efficiency measurement with one hundred samples. The "Binomial" error vanishes for the situation of reaching absolute or zero efficiency while the "Bayesian" error reaches a finite value.

The shape of the probability density $P(\varepsilon|k,n)$ is shown for different pairs of k and n in fig. 7.4. Especially for very high and low efficient detectors, which will give measurements with k values close to n and zero respectively, the distribution deviates significantly from a Gaussian. In this case, an estimate of the error of the efficiency, $\Delta\varepsilon$, is more appropriately given by the shortest 68.3% confidence interval around the most probable value.

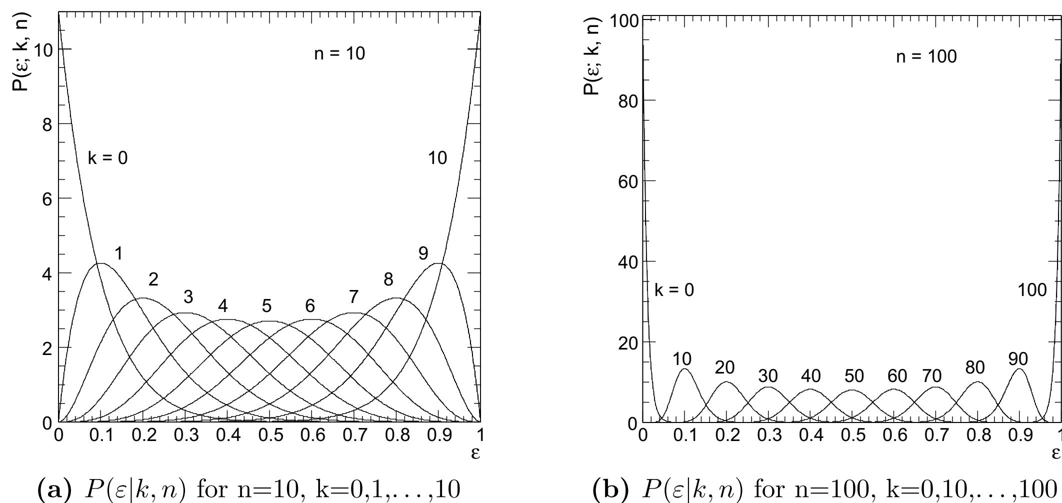

(a) $P(\varepsilon|k,n)$ for n=10, k=0,1,. . . ,10

(b) $P(\varepsilon|k,n)$ for n=100, k=0,10,. . . ,100

Figure 7.4: The probability density function for different n,k value pairs [57].

8 Diamond Pixel Sensors

Diamond sensors are solely composed of the CVD-diamond[1] bulk and metal electrodes on the top and the bottom. Contrary to silicon a diode junction is not required. The bulk material directly acts as solid state ionization chamber. Figure 8.1 illustrates the concept of a hybrid diamond pixel detector.

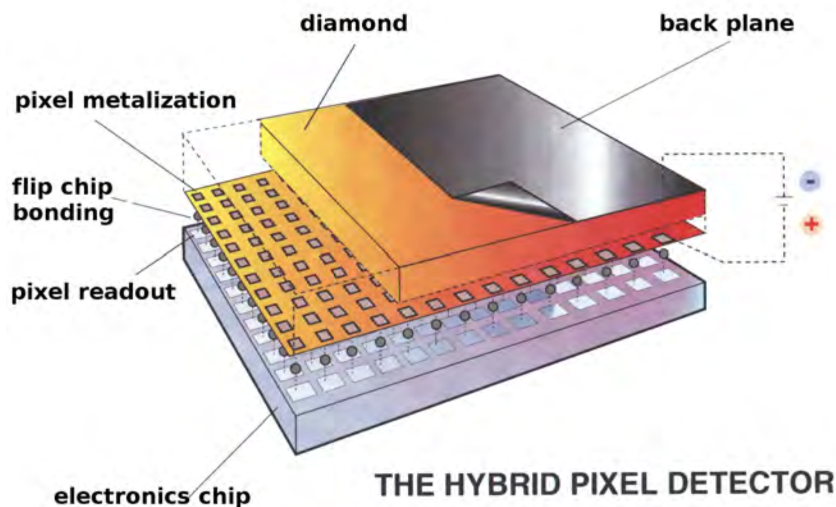

Figure 8.1: Schematic view of a hybrid diamond pixel detector

For the sensors poly-crystalline (pCVD) as well as single crystalline (scCVD) CVD-diamond is commercially available. While pCVD diamond can be fabricated in wafers of up to 12 cm in diameter, scCVD diamond is at present only available in pieces of about 1 cm^2. The properties of the different diamond materials and the benefits of diamond regarding radiation hardness have been outlined in chapter 3.4 and chapter 4.2.

Especially the option to operate without low temperature cooling and the achievable signal-to-noise ratio after high irradiation render them very promising for detectors close to the interaction point. To prove the feasibility of a diamond pixel detector with a size reasonable for a real detector, an ATLAS-like 16 chip module with a poly-crystalline sensor of $2 \times 6\,cm^2$ has been produced and characterized. Results will be presented in section 8.2.

[1] *Chemical Vapor Deposition* (CVD). See chap. 3.4

Single crystalline diamond is also of great interest for pixel detectors. The material does not suffer from the charge collection deficiencies inherent to the grain structure of poly-crystalline material. Single crystal diamond sensors show a spectroscopic-grade charge collection previously only known from silicon. The results of the first scCVD pixel detector are presented in section 8.1.

Fabrication: The diamond sensor material is delivered thinned to the desired thickness, polished and cut to the required shape from the CVD-diamond manufacturer “elementsix”[2]. The sensors are cut to shape with a laser. The laser cutting graphitizes the surface which makes cutting after the electrode metalization impractical. To allow the processing of a diamond sensor using the same industrial equipment as used for the assembly of silicon pixel sensors, the sensor is embedded in a wafer-like support structure. The procedures to even embed an irregular shaped sensor into a ceramic support wafer have been developed by IZM[3]. A cut out is made in the ceramic support wafer according to the shape of the diamond and the sensor is glued in with an epoxy fully planar to the supports surface. Figure 8.2 shows a module size piece of pCVD diamond as well as a scCVD sensor in their embedded state. The embedded sensors are then ready for metalization

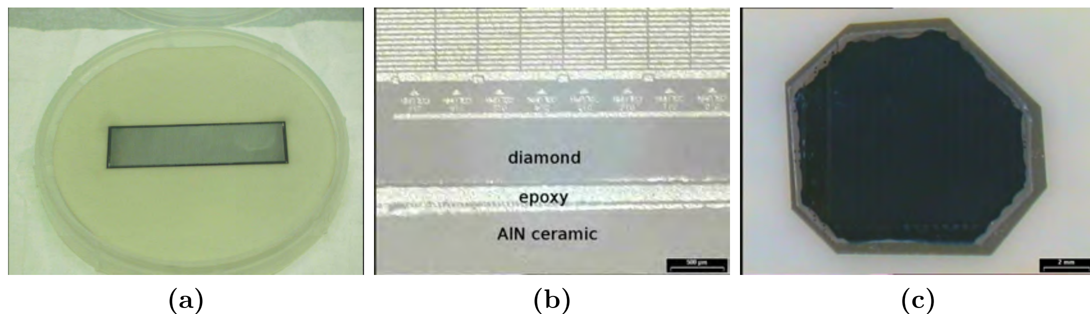

(a) (b) (c)

Figure 8.2: Embedded diamond sensors for silicon-wafer like processing. (a) $2 \times 6\,\mathrm{cm}^2$ diamond sensor embedded in a 10 cm wafer. (b) close view of the epoxy glue connection. (c) embedded, irregular shaped single crystal diamond of $1\,\mathrm{cm}^2$.

and solder bumping using the standard processing facilities. Before the structure is flip-chipped to a readout chip, the sensors are taken out of the support wafer. For the studied prototypes the first metalization was deposited at the Ohio State University before embedding. Only the under bump metalization and bumping were carried out in the embedded state.

[2]former “De Beers Industrial Diamonds”
[3]Institut für Zuverlässigkeit und Mikrointegration, Berlin, Germany

8.1 scCVD diamond single chip assembly

The scCVD single chip assembly has been realized with a 395 μm thick single crystal diamond of about 1 cm^2. All the processing steps from the unmetalized diamond sensor to the fully working detector were realized within a short timescale of several weeks by the industrial partner IZM. The assembly with the sensor bump bonded to the readout chip is shown in fig. 8.3(a). Due to its shape, it was impossible to connect all channels of the readout chip to a sensor pixel. The backplane metalization ends a few millimeters apart of the sensors edges and shows there a slight liftoff. This is partly attributed to the epoxy removal step after embedding. Therefore, shortcomings in the charge collection at the edge pixels are expected. The metalization of the pixel electrodes itself worked fine. Except for two pixels it has a perfect metal to diamond surface adhesion. Figure 8.3(b) shows a section of the pixel metalization.

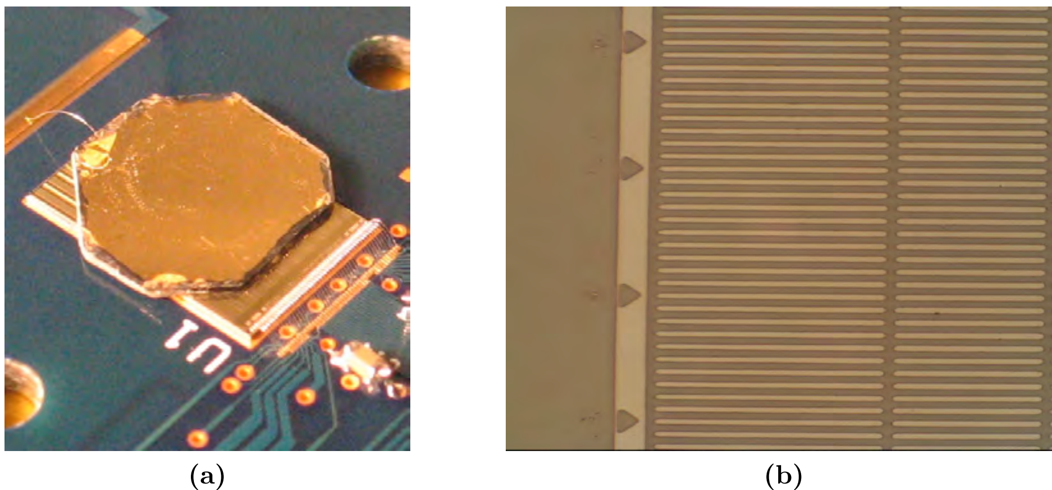

(a) **(b)**

Figure 8.3: (a) Irregular shaped scCVD diamond sensor bump bonded to the readout chip. (b) Close-up of the pixel metalization of the sensor before the bump bonding process.

Setting up operation: The diamond detector was operated at a threshold of 1700 e (GDAC 5, TrimT 64) and was tuned to a ToT value of 30 at an injected charge of 10000 e (IF 18, TrimF 10). The mean threshold obtained after tuning is (1676 ± 40) e (fig. 8.4(a)) with an electronics noise level of (130 ± 9) e (fig. 8.4(c)). This noise value is measured to be comparable to the noise of a sensorless chip.

As a first test, the device was illuminated with an ^{241}Am γ-source, which deposits about 4500 e in the sensor. The hitmap is shown in fig. 8.5(a). In conjunction with the results from the calibration this hitmap was used to derive a map of good and bad pixels. The map is shown in fig. 8.5(b). All channels not being connected to

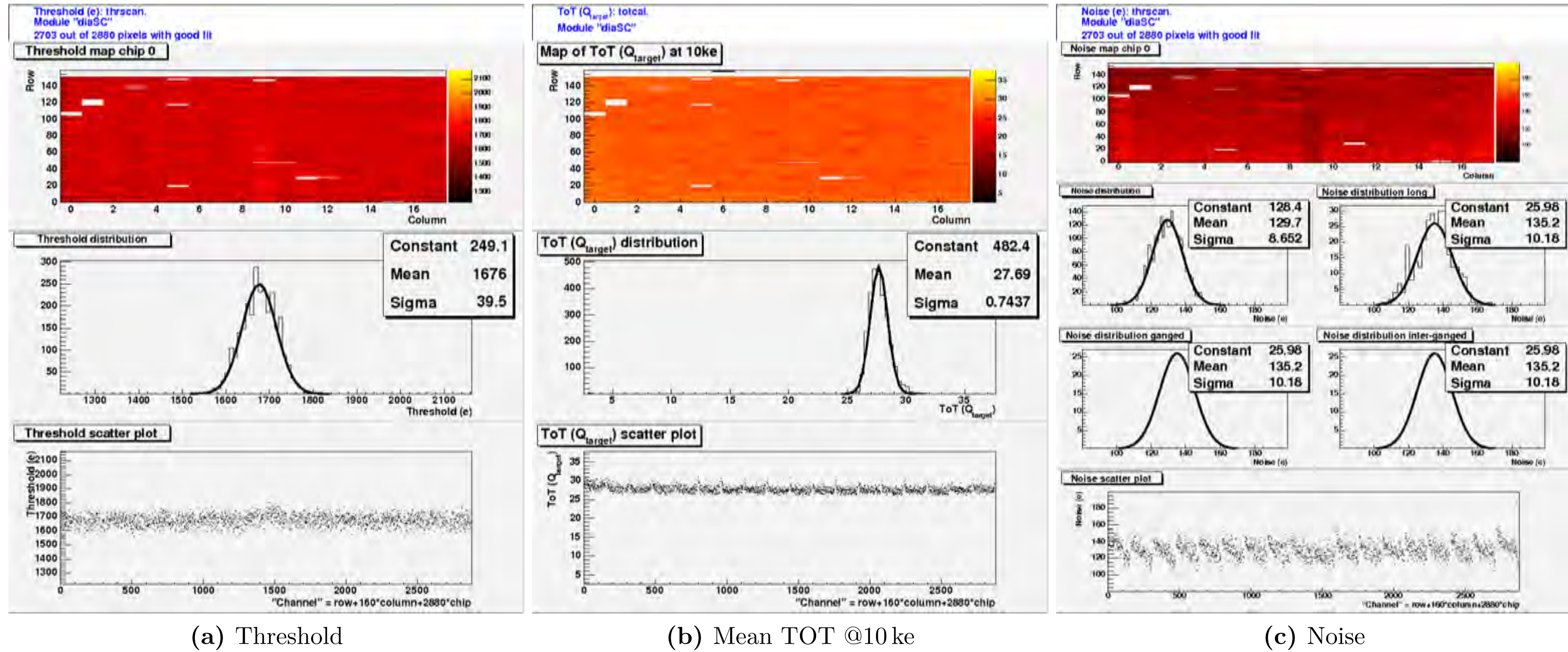

(a) Threshold **(b)** Mean TOT @10 ke **(c)** Noise

Figure 8.4: Maps showing the threshold, ToT@10 ke and noise values obtained with the tuning used for the measurements.

the sensor (324) or having no valid threshold tuning (12) have been masked out. Additionally, the very noisy channels (4) identified by the source scan as well as the pixel cells potentially suffering from a bad or missing backplane metalization (353) have been masked out. Two pixels (13/16;17/36) were identified to show no hits, which is most likely due to a missing solder bump connection.

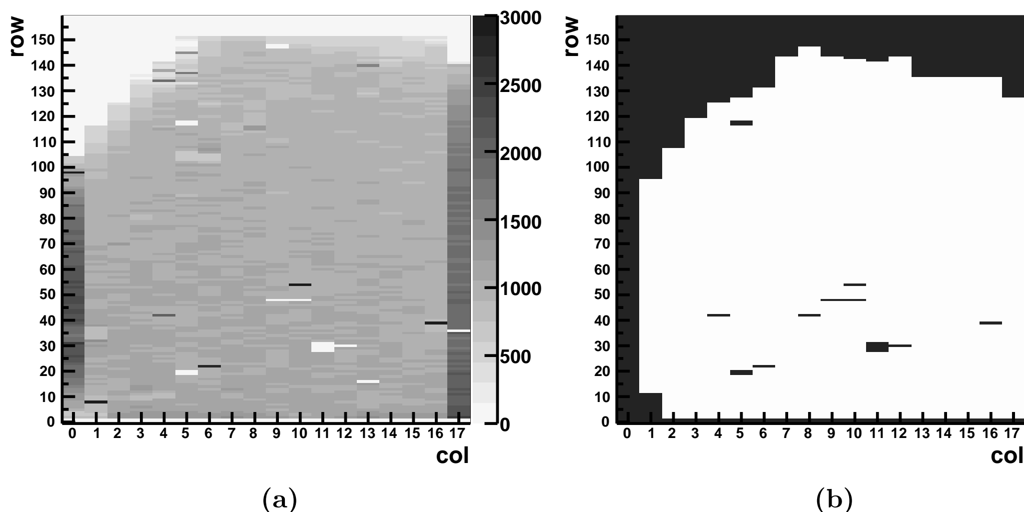

Figure 8.5: (a) Hit map obtained by illumination with a ^{241}Am source. (b) Map of masked out (black) pixels

The charge calibration (chap. 7.2) was carried out using the inbuilt C_{high} charge injection circuit. The values from the standard wafer test procedure [43] have been used as calibration for the injection circuit (41.4 fF,0.913 mV/DAC).

In fig. 8.6(a) the ToT response of one individual pixel to the injected charge is shown. The solid line is the calibration fit. The range for fitting has been limited to the region of 10 ke to 25 ke, where most of the charge deposits of particles are expected. The ToT calibration is obtained for every pixel individually. Figure 8.6(b) displays the spread of the calibrations over all pixels by superimposing all calibration curves. The error-bars illustrate the RMS spread of the projection on the y-axis. It has been shown for silicon detectors, that the charge calibration uncertainty is in the order of 10% and usually underestimates the deposited charge [55]. The same uncertainty is also assumed for the diamond device.

To address the accuracy of a single charge measurement, in fig. 8.6(c) the distribution of input charges resulting in the same ToT value is shown for a selected pixel. The sigma of the distribution corresponds to a noise of 500 e. This is much higher than the 130 e obtained from the threshold measurement. The discrepancy is understandable as the ToT noise originates from a jitter in the width of the shaped charge pulse at the discriminator, while the threshold noise depends on the jitter of the pulse hight (see also fig. 5.7, chap. 5 for clarification).

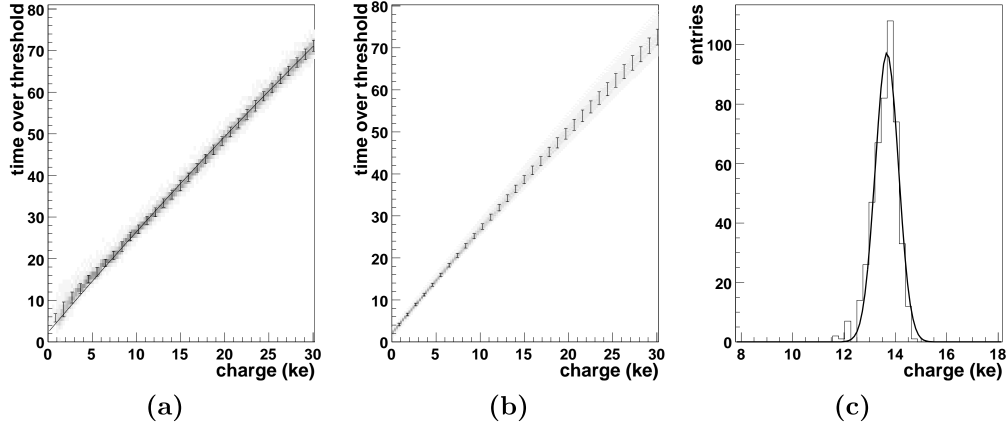

Figure 8.6: (a) ToT response to injected charges of fixed amount for one pixel. The curve corresponds to the calibration used for this pixel in the ToT to charge conversion. (b) The calibration function superimposed for all connected pixels. The vertical bars illustrate the RMS of the pixel to pixel spread. (c) Distribution of input charges of one selected pixel for a fixed ToT of 34 with a mean of 13700 e and a sigma of 500 e.

A cross calibration of the charge calibration by means of standard radioactive source is more difficult than for silicon sensors. Diamond has a much higher Compton contribution to the photon absorption (chap. 3.2). In addition, the appearance of several nearby emission lines in many of the practical radioactive sources and the limited ToT charge resolution of the used front end electronics make an accurate calibration impossible.

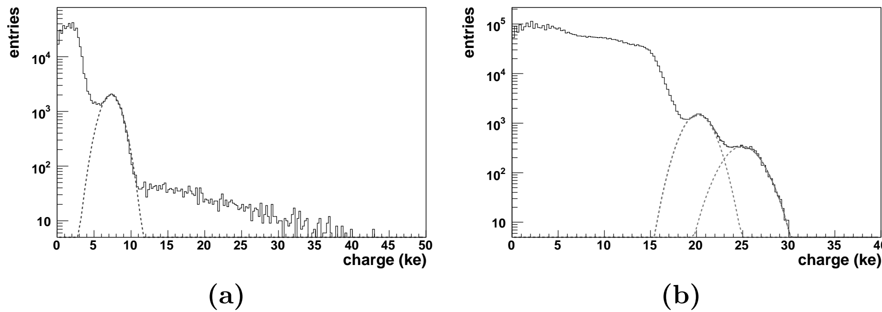

Figure 8.7: (a) charge spectrum obtained by illumination with an ^{57}Co source (122 keV). The fitted Gaussian corresponds to a peak charge of 7300 e (95 keV). (b) charge spectrum obtained by illumination with an ^{133}Ba source (356 keV, 303 keV, 384 keV, 276 keV). The fitted double Gaussian corresponds to peak charges of 20000 e and 25000 e (265 keV and 325 keV).

The spectrum obtained from the γ-lines of an Americium source turned out to be useless for calibration because of the mentioned effects. The measured spectra of a ^{133}Ba and ^{57}Co source are shown in fig. 8.7(a+b). The most probable γ-emissions for Barium, sorted by occurrence, are 356 keV, 303 keV, 384 keV and 276 keV respectively. In the measured charge spectrum one can only resolve two peaks (note the log scale) at 265 keV and 325 keV. Nevertheless, the measurement indicates that the used calibration most likely underestimates the deposited charge. This is in agreement with the expectations.

Testbeam measurements

The beam tests have been carried out in a 100 GeV beam of pions at the CERN SPS. For technical reasons the average data taking rate was limited to about $50-60$ Hz and the trigger region reduced to an area of about $4 \times 4\,\mathrm{mm}^2$. To predict the hit position in the scCVD diamond device, the testbeam reference system described in chapter 6 was used. Only tracks from events with a single hit in each telescope plane were selected for the characterization measurements. The precision obtained in the plane of the device under test (DUT) including the alignment uncertainties is about 5 µm. The beam divergence is measured to be less than 0.2 mrad. The uncertainty in the beam incidence angle with respect to the DUT plane is at most 1°.

Charge collection and cluster size: In single crystal diamond the electric field is constant over the full bulk thickness. Its absolute value is proportional to the applied bias. As the drift velocity is directly proportional to the field, higher fields cause faster charge collection and hence a smaller spread of the charge cloud by diffusion. This effect is observed in fig. 8.8(a-b), where the measured charge distributions are plotted for fields of roughly (a) 0.25 V/µm (100 V), (b) 0.5 V/µm (200 V) and (c) 1 V/µm (400 V).

As discussed previously (chap. 3), the shape of the Landau distribution depends on the density and thickness of the sensor material. For the 395 µm thick diamond sensor one expects a most probable value (Δ_p) of 13900 e and a full width at half maximum of 4200 e. The measured values of 13100 e and 4000 e are within the ToT calibration uncertainties of 10% in good agreement with the expectations.

For bias voltages below 100 V the shape of the cluster charge distribution starts to change as shown in fig. 8.9. The nominal charge deposition of 13000 e moves to lower values as expected due to an increased lateral diffusion. In addition a second class of charge depositions show up at the lower side of the distribution. Of special interest is the fact, that for both kinds of charge deposition single as well as double hits are observed. To study the effect further, hits are separated by having a charge depositions above or below 9 ke. Figures 8.10(a-c) show for different bias voltages the fraction of hits below 9 ke for all pixels as maps. The low charge entries observed for bias voltages below 100 V can be clearly assigned

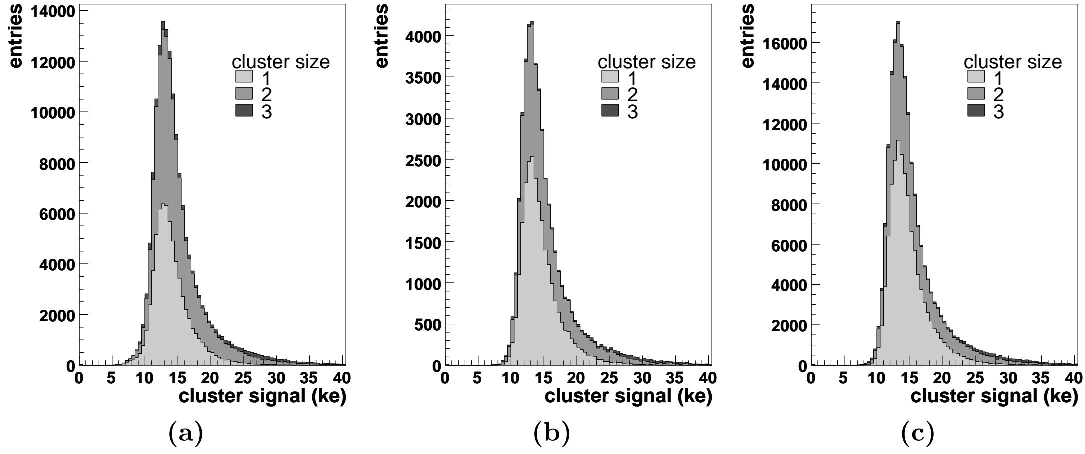

Figure 8.8: Signal charges separated by the contribution of one, two and three pixel clusters for bias voltages of (a) 100 V (0.25 V/µm), (b) 200 V (0.5 V/µm) and (c) 400 V (1 V/µm)

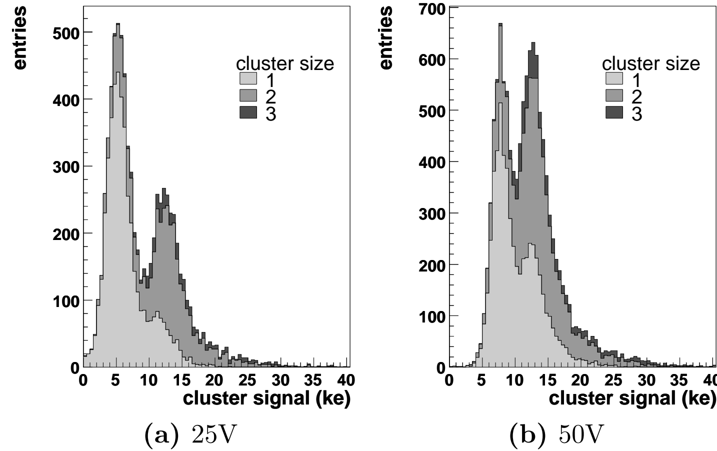

Figure 8.9: Signal charges separated by the contribution of one, two and three pixel clusters for bias voltages of 25V and 50V.

to the upper left region of the sensor. Figure 8.11 shows the fraction of single hit clusters per pixel for selected bias voltages.

The reduced charge collection in combination with the increased average cluster size are a clear indication for a reduced electrical field in the upper left part of the device. The reduction either originates from space charge present in the diamond bulk itself or from effects at the metal to bulk interface. The latter is much more likely for the backplane contact as a metal lift of has been already observed for the edge regions. However, no implication of these effect has been observed for the

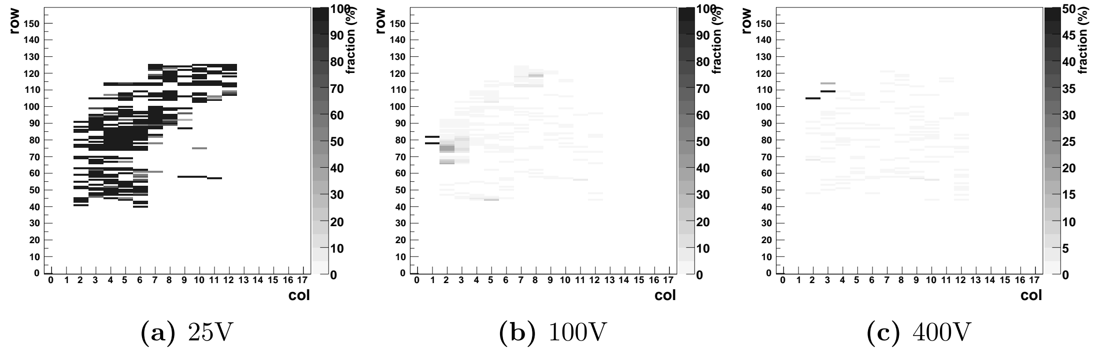

(a) 25V **(b)** 100V **(c)** 400V

Figure 8.10: Fraction of hits with a charge deposit below 9 ke.

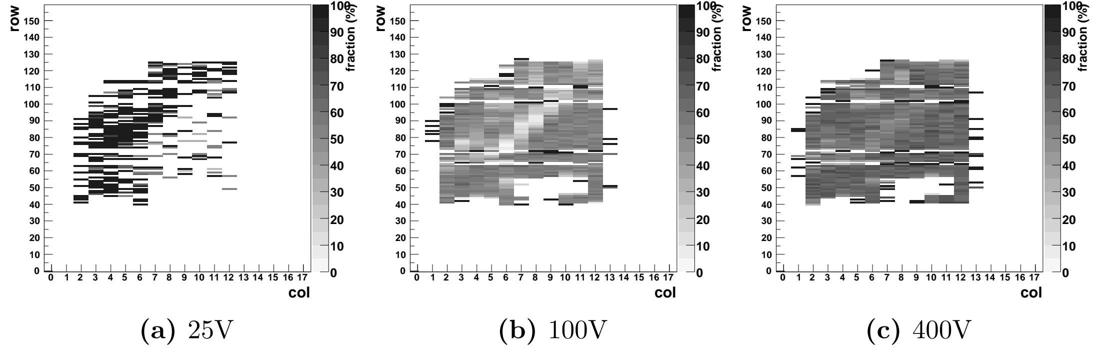

(a) 25V **(b)** 100V **(c)** 400V

Figure 8.11: Fraction of one hit clusters.

charge distribution as well as for the charge sharing at bias voltages above 100 V (0.25 V/μm).

Concentrating on hits in the lower right part of the sensor, fig. 8.12(a) shows the most probable charge measured as a function of the bias voltage. The curve saturates for voltages above about 100 V, indicating that for single crystal diamond full charge collection is already reached for fields of 0.5 V/μm. The slight increase still observed is an expected effect induced by the readout threshold of 1700 e and the charge sharing between adjacent pixel cells. The dependence of the charge sharing on the bias voltage becomes also visible in the distribution of cluster sizes shown in fig. 8.12(b). The cluster size corresponds to the number of adjacent pixels above threshold. At low biasing the lateral diffusion distributes the charge cloud over several pixels. Most of the observed clusters are two hit clusters. Observing a one hit clusters just means, that the amount of charge spread in a neighboring pixels is below the readout threshold. With increase in bias voltages the lateral charge spread reduces. At a bias of 200 V single and double hit clusters have a

fractional sharing of roughly 60:40. The overall efficiency to find a hit near a track point (i.e. within 3x5 pixels) extrapolated on the plane of the DUT is found to be larger than 99.9%.

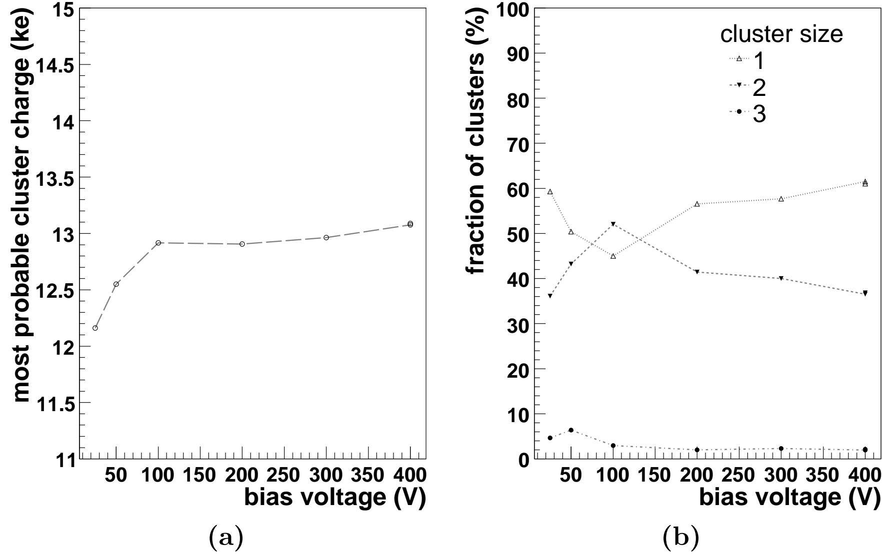

Figure 8.12: (a) Most probable values of the charge distribution and (b) fraction of charge cluster of noted size as a function of the bias voltage.

Hit reconstruction: The spatial resolution of the scCVD device is determined by measuring the differences between the position reconstructed in the device and the position predicted in the plane of the device by the telescope. Figure 8.13 shows these residual distributions in the two pixel dimensions. For both, first only the center of the pixel with the highest charge entry is used as the hit position (light gray distributions). Second also the charge sharing between neighboring pixels is considered (dark gray distributions).

The expected digital resolutions of pixel pitch divided by $\sqrt{12}$ in both directions, i.e. 14.5 μm and 115 μm, respectively, folded by the resolution of the track extrapolation of about 5 μm, is observed. Position reconstruction considering the charge information available via the ToT readout is done using the η-algorithm (chap. 6.1.1), where the η-correction function has been calculated column wise. The intrinsic resolution of the device in the short pixel direction (fig. 8.13(b)), after quadratically subtracting the telescope extrapolation error of 5 μm, then is (8.9 ± 0.1) μm for a bias voltage of 200 V. The performance of the η-algorithm depends on the charge sharing and thus on the used bias voltage (fig. 8.13(c)).

In previous studies of poly-crystalline diamond [24], the pCVD grain structure and the trapping of electric charges at the grain boundaries causing horizontal polarization fields, have been shown to influence the space point reconstruction in

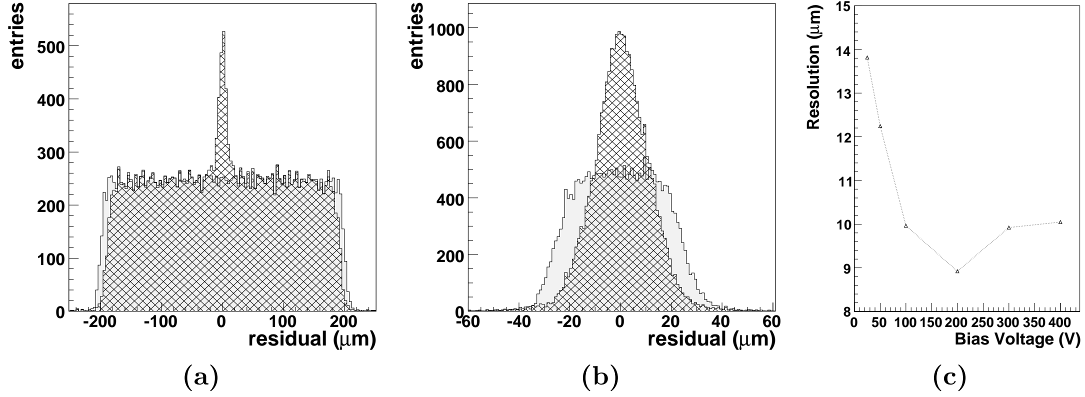

Figure 8.13: Spatial resolution of the scCVD diamond device. (a) resolution in 400 μm direction. (b) resolution in 50 μm direction. (c) intrinsic resolution in 50 μm direction in dependence of the applied bias voltage.

pCVD devices. To classify this effect the same procedure as described in [24] has been used. For hits taken in different events fig. 8.14 shows the correlation of the measured residuals in the short 50 μm pixel dimension as a function of the distance of the tracks' impact points (given by the telescope extrapolation). The sinusoidal shape of this distribution reflects the pixel pitch of 50 μm, damped by the radial distance effect. The data are well fitted by a functional form $a \sin(bx)/\sqrt{x} + c\ \exp(-x/r_c)$, with c being consistent with zero. In [24] it was shown that in comparison with silicon, pCVD diamond – as a consequence of the pCVD grain structure – showed a net correlation developing for small two track distances and a correlation length $r_c = 36$ μm for the exponential term was measured. This effect, observed in [24], is indicated by the dashed lines in figs. 8.14. The measurement demonstrates that in single crystalline diamond for a bias voltage above 200 V such a net correlation does not exist, i.e. no evidence for polarization fields are observed.

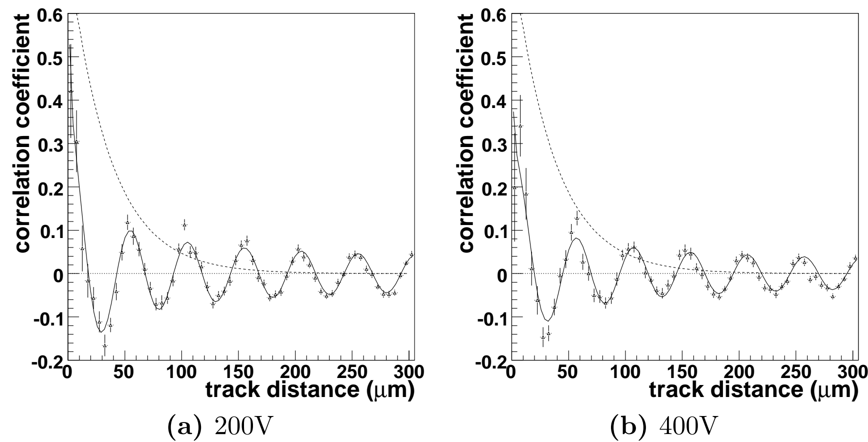

(a) 200V **(b)** 400V

Figure 8.14: Correlation coefficient between the spatial residuals of two events, as a function of the separation between the tracks of the two events. The correlation is shown for a bias of 200V (a) and 400V (b). The solid line is a fit with a function containing a $\sin(\mathrm{ax})/\sqrt{x}$ plus an exponential term. The dashed line displays the correlation found in [24] for a pCVD diamond device showing a pronounced exponential contribution. The dotted line is the exponential contribution for the single crystal diamond.

8.2 pCVD diamond module

The pCVD diamond sensor used for the complete module has been cut out from a 10 cm pCVD diamond wafer. The finally used sensor has a size of about $64 \times 19\,\mathrm{mm}^2$. For the first production of a diamond module it was chosen to go with the original wafer thickness of 800 μm even if a contribution for signal generation is only expected from the region at the pixel electrodes within the charge collection distance. Thinning of diamond is a time consuming process and was not done here. In fig. 8.15 the diamond sensor bump bonded to 16 FE-I3 chips for readout is shown. The device is completed by a flex-hybrid (chap. 5) glued on top of the sensor. The flex distributes the power and connects the individual chips to the readout system. The diamond module looks the same as a standard silicon module (fig. 8.16) as the sensor is covered on one side by the chips and on the other by the flex.

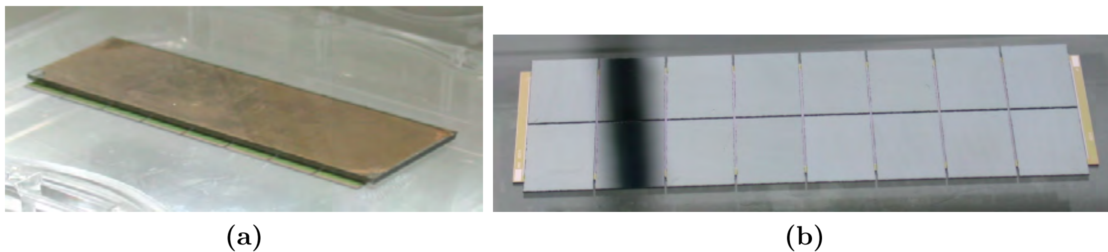

(a) (b)

Figure 8.15: Diamond module equipped with 16 FE-I3 chips for readout. The photographs show (a) the sensor side and (b) the electronics side of the device (the black strip on (b) is a shadow).

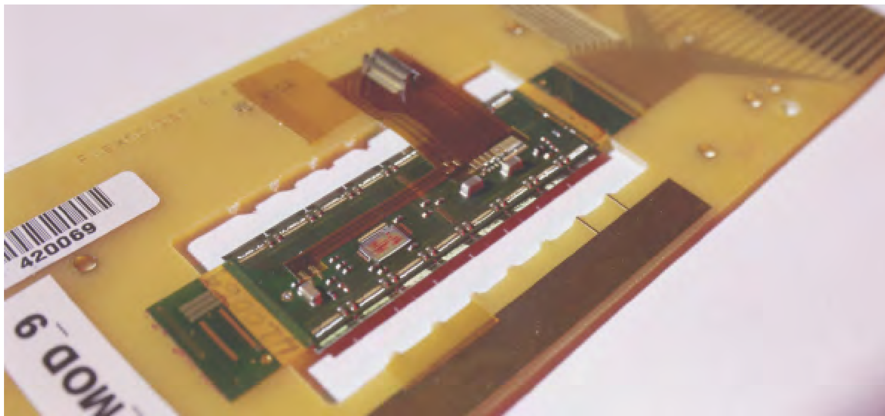

Figure 8.16: Image of a full dressed ATLAS module. The module is glued with the flex-hybrid on a support frame to ease handling during production and testing.

The backside of the sensor is metalized as a whole to form the backplane electrode. The backplane metalization shows a slight lift of the outermost edges of the

device. As a nice side effect, this allows for a view from the backside, through the (transparent) diamond on the surface of the readout chip (fig. 8.17). The metalization for the pixel electrodes follows the geometry given by the current ATLAS pixel sensor layout (chap. 5, fig. 5.2), including enlarged and ganged pixels in the regions between two readout chips. The metalization worked fine for the dominant fraction of the surface (fig. 8.18(a)). For the ganged pixels and some distributed regions, especially at the corners, however, the pixel metalization had problems with adhesion to the surface (fig. 8.18(b)). This problem could be partially traced back to doing the metalization without embedding of the module. The rectangular shape of the sensor prevented a homogeneous spinning of the coatings on the sensor during the lithographic processes. In order to keep with the time schedule it was chosen to not redo the metalization. During the under bump metalization a second metal layer according to the pixel geometry is deposited, which was expected to work also as pixel electrode. Figure. 8.18(c+d) shows the result. In regions where the pixel metalization worked fine, also the under bump metalization (UBM) was. In the regions where the pixel metalization was missing, the UBM produced partially electrodes which may still work for charge collection.

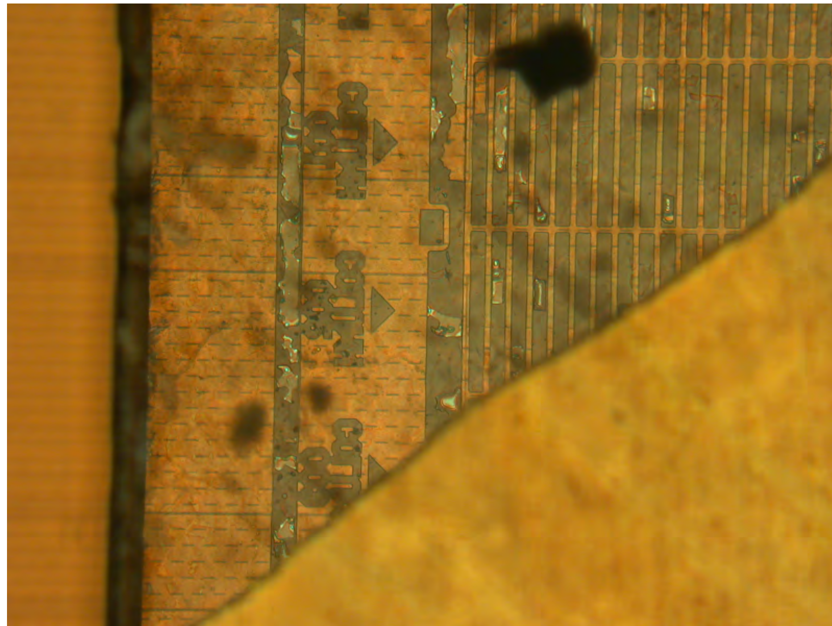

Figure 8.17: View through the diamond sensor at the corner of the device. The area in the lower right is the backplane metalization. In the center one looks through the diamond sensor on top of the pixel metalization. Between the metalization the surface of the readout chip appears. The black strip to the left marks the edge of the sensor. Due to the different refraction indexes of diamond and air the part of the pixel chip visible on the left is blurred.

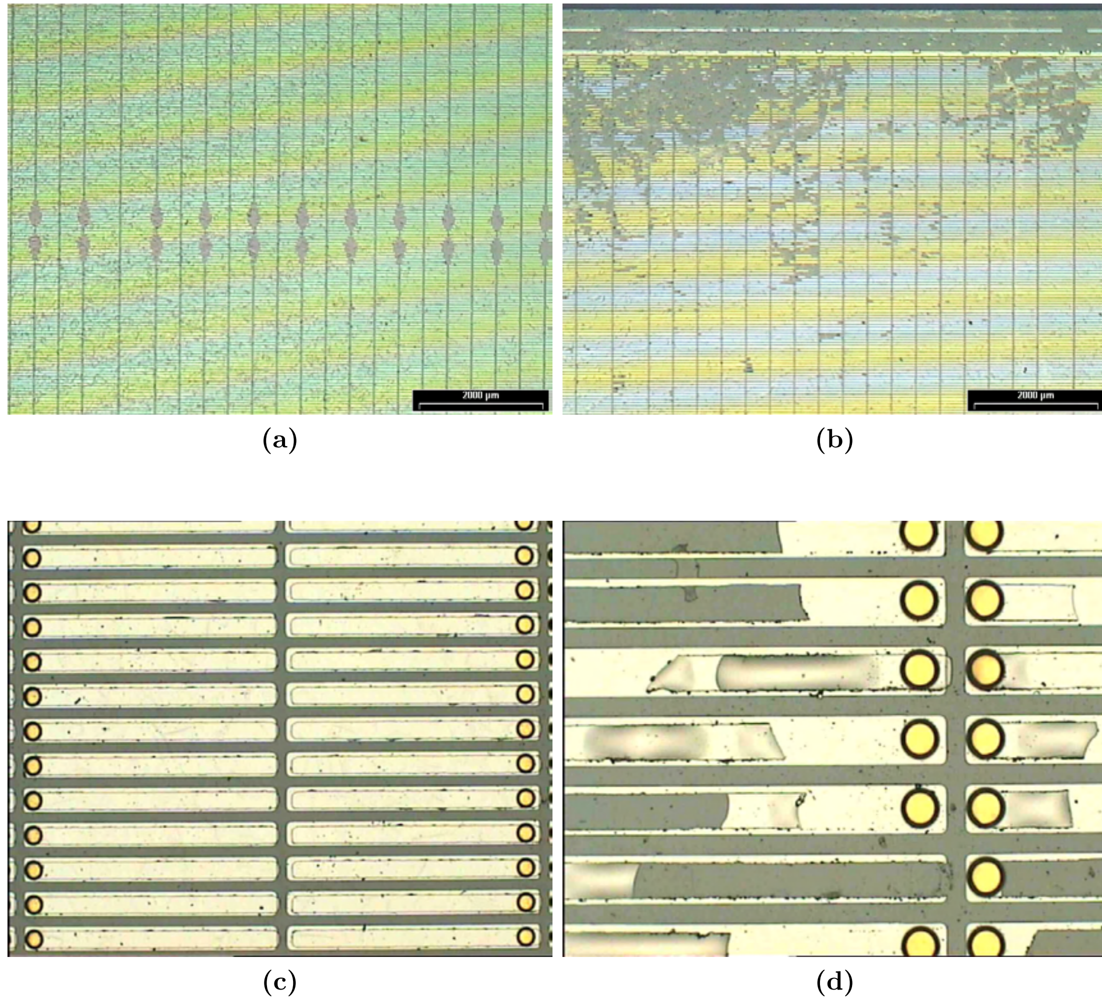

Figure 8.18: (a+b) Pixel metalization on the pCVD diamond module in (a) the center and (b) the corner region. (c+d) Under bump metalization for a region with previously (c) good and (d) bad pixel metalization. The under bump metalization at the yellow dots will mate with the solder bumps on the readout chip.

Setting up operation: After assembly all 16 chips of the module were functioning. While testing for bias voltages above 1000 V, however, a discharge occurred which killed one of the front-end chips. The back plane metalization, which stays at the biasing potential, has been carried without a guard ring structure for simplicity reasons. The guard ring structure would keep the applied potential away from the edges and thus reduce the chances for a discharge. In addition the used ATLAS flex hybrids are only specified for biasing up to 800 V.

The focus for the tuning of the device lay on the characterization of the charge collection properties. Therefore it was chosen to tune the device to the lowest threshold and lowest granular ToT settings at which the modules stayed operational. For the diamond module a target threshold of 1500 e (GDAC 5, TrimT 64) and a ToT response of 60 at an injected charge of 5000 e (IF 4, TrimF 3) could be reached. The mean threshold observed after tuning is (1477 ± 26) e (fig. 8.19(a)) with an electronics noise level of (133 ± 9) e (fig. 8.19(b)). As already seen for the single crystal device, the noise observed is comparable to the one of a sensorless chip.

It turned out, that a calibration of the ToT response especially for low charge values was required. For this low charge regime only calibration data using the C_{low} charge injection capacity were available. The calibration values for the charge injection circuit itself are available for each chip of the module from the standard wafer test procedures. The values are dispersed between 7.15 fF and 7.89 fF for the C_{low} capacity and between 0.883 mV/DAC and 0.959 mV/DAC for the voltage DAC. Figure 8.20(a) shows the ToT response of a typical pixel to the injected charges. Especially close to the threshold, the response deviates from a linear behavior. As the shape could not be fitted with a single standard calibration curve, the best result was obtained by a separation in two regions: One from 1500 e to 5000 e and the other from 5000 e to 10000 e. The first is being used to reconstruct the charges for ToT responses below 60, while the latter is being used for values above. In principle, the used calibration allows for a high charge resolution (1 ToT $\approx$ 125 e). The spectrum of injected charge values observed for a fixed ToT of 60 shows, however, a noise of 500 e (fig. 8.20(c)) which thus sets the limits on the charge resolution.

While γ-sources were already of limited use for the cross-calibration of the ToT calibration, the situation is even worse for poly-crystalline material. The limited charge collection distance inherent to poly-crystalline material makes the charge seen depended on the distance of the γ-conversion from the collecting electrode. This completely broadens out the peaks from calibration sources and make them useless for calibration purposes. Nevertheless, the pixel to pixel hit rate variations observed in a source test allows the identification of dead channels as they originate from missing bump connections, bad/missing pixel metalizations, dead electronics channels or a bad spots in the diamond substrate itself. Figure 8.21(a) shows the hitmap obtained with an ^{241}Am γ-source placed above the center of the sensor. The regions of the individual readout chips are visible due to the increased hit rates in the enlarged pixels, which are located in the area between two readout

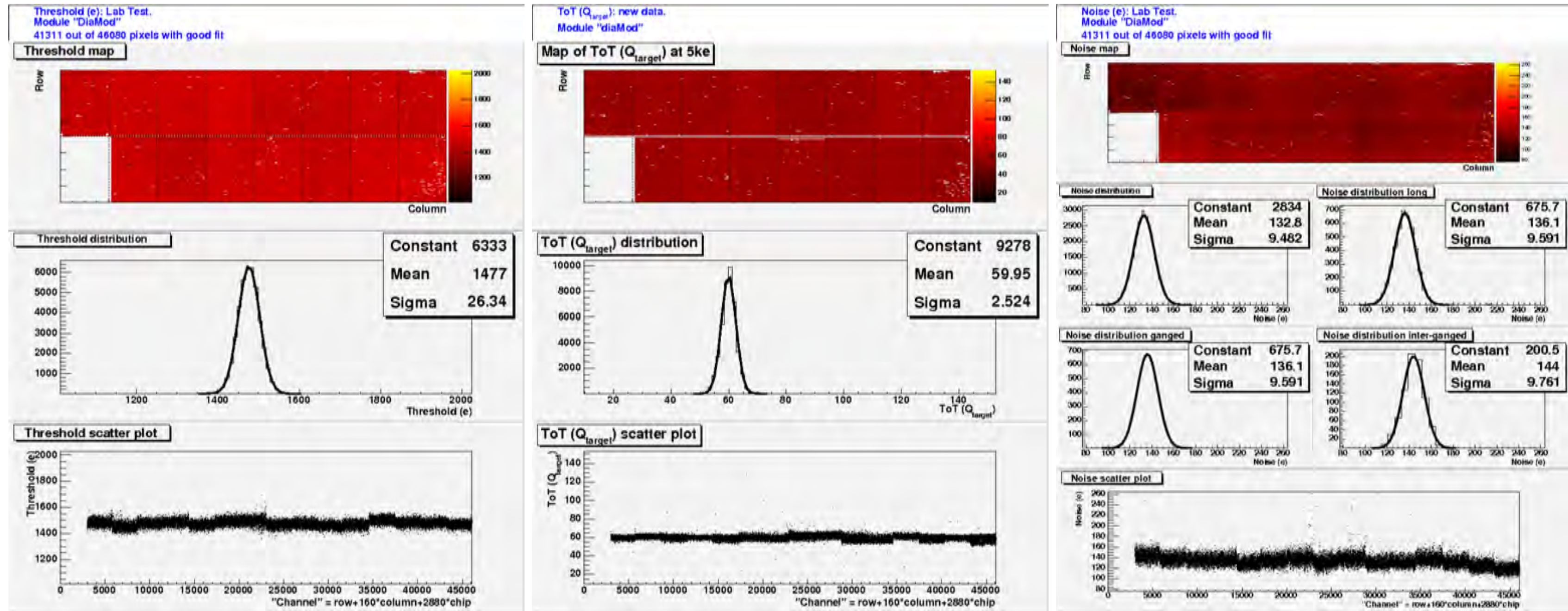

(a) Threshold **(b)** Mean TOT @5 ke **(c)** Noise

Figure 8.19: Maps showing the threshold, ToT@10 ke and noise values obtained with the tuning used for the measurements.

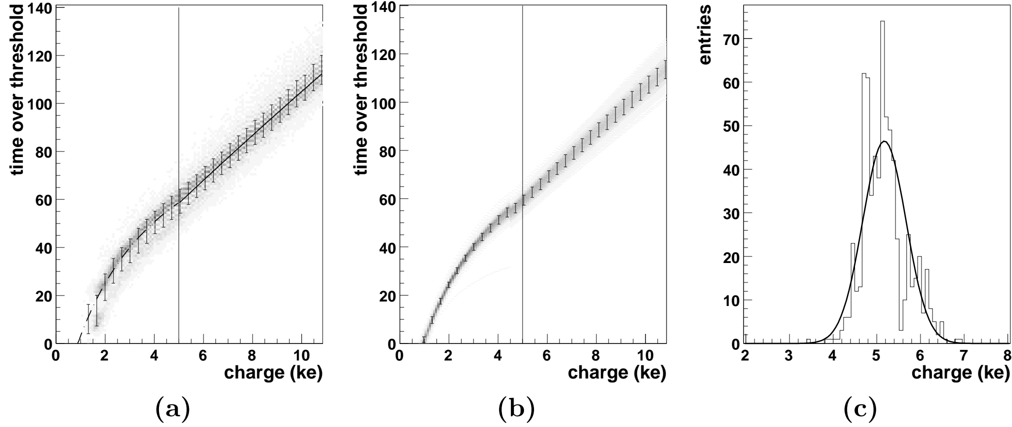

Figure 8.20: (a) ToT response to injected charges of fixed amount for one pixel. The shown curve is the calibration function used. It has been separately obtained for charge values below and above 5 ke (indicated by the vertical line). (b) The pixel individual charge calibration superimposed for all pixels of one chip. The bars illustrate the spread of the calibration functions. (c) Distribution of input charges of one selected pixel for a fixed ToT of 60. The fitted Gaussian has a mean of 5200 e and a sigma of 500 e.

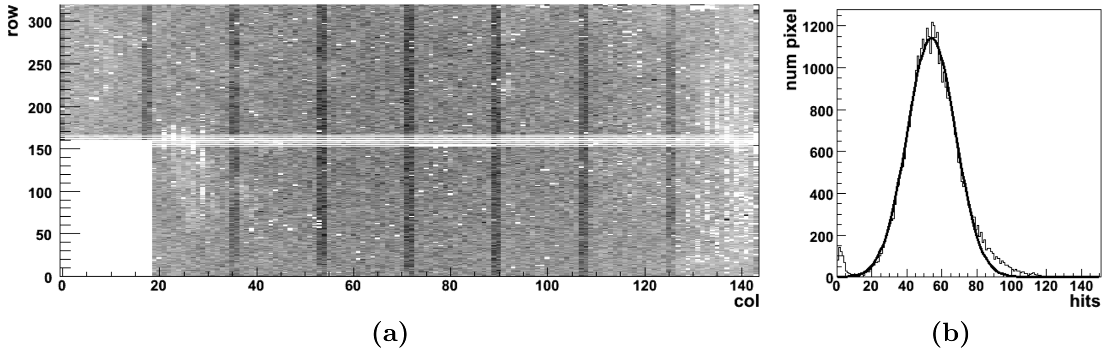

Figure 8.21: (a) hit map obtained by illumination with a ^{241}Am source. (b) distribution of hits seen in the individual pixels.

chips. While the illumination is quite homogeneous in the short sensor direction, the illumination profile falls off in the long sensor direction by about 40% due to the geometry of the source. The distribution of hits observed per pixel is shown in fig. 8.21(b). It follows a Gaussian shape, broadened by the illumination falloff and extended to higher values due to the larger pixels at the chip edges. The Gaussian has a mean of 54 hits and a sigma of 14 hits. Pixels with less than 12 hits (3σ below mean) have been masked out. Ignoring the disabled ganged and by the discharge destroyed channels, in total 97% out of 41964 pixels are working.

The 3% of dead channels is given by 653 pixels for which no valid tuning could be obtained and 628 pixels showing insufficient hits during the source test. As can be seen in fig. 8.21(a), most of the dead channels are located on the last two chips on the right side of the module and in a spot located in the center of the second column of readout chips.

Beam measurements: The module has been operated in a 4 GeV electron beam at the DESY testbeam facility with an applied bias voltage of 800 V. For the large area diamond module, the main focus was the operation of under realistic beam conditions rather than the detailed characterization of the diamond sensor properties. Those have been characterized with single chip devices [12, 24, 58]. The fact, that a 16-chip module with all[4] chips working can be operated in a beam, has to be regarded as a big success towards the feasibility of making a larger area pixel detector with using pCVD diamond as sensor material.

Figure 8.22 shows the residual distributions obtained along the two pixel dimensions respectively. Due to the large impact of multiple scattering on the 4 GeV electron beam, the hit prediction precision in the plane of the diamond module is in the order of 20 μm. This adds to the expected RMS for a 50 μm pixel pitch of 14.5 μm and is consistent with the observed RMS of 23 μm. For the long pixel

[4] The one missing chip was destroyed by a discharge as described previously. The diamond sensor itself worked well prior to the discharge. Actually, some data with this chip working is available.

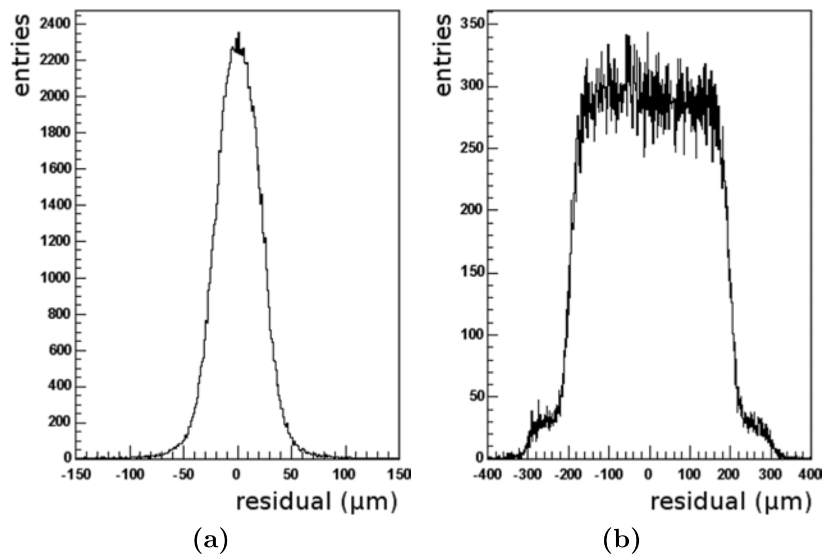

Figure 8.22: Residual distribution along (a), the short pixel and (b), the long pixel direction. In (b) the contribution from the 400 μm as well as the 600 μm long inter chip pixels is visible.

direction, the distribution contains contributions from the 400 µm long as well as from the 600 µm long inter chip pixels.

The charge distribution observed during the beam measurements is shown in fig. 8.23(a). The typical well known Landau shape distribution is not observed due to the influence of the limited charge carrier lifetime in pCVD diamond and due to charge sharing effects between adjacent pixel cells in combination with readout thresholds of the pixel electronics. To qualitatively verify this assumptions a minimal Monte Carlo simulations was carried out. The 800 µm thick diamond has been divided in 50 µm thick slices. For each slice, a charge deposit as expected from the corresponding Landau distribution (chap. 3) was chosen randomly and the charge loss due to the limited charge collection distance (carrier lifetime) was calculated in dependence of the distance of the slice to the readout electrode. The resulting total charge is then spread assuming a Gaussian shape profile across the adjacent pixels after choosing the center of the charge deposit randomly inside the region of a pixel cell. Finally the readout thresholds are applied and the charge measured in total summed up. For the threshold dispersion and noise 130 e have been assumed. Also the ToT to charge uncertainty of 500 has been considered (fig. 8.20(c)) . The 800 µm thick diamond material used for the module sensor is known to have a charge collection distance of more than 300 µm at bias voltages above 400 V (0.5 V/µm) as it becomes visible in fig. 8.24 [59]. One thus expects from the simulation for the module operated at 800 V bias a charge distribution as shown in fig. 8.23(c). For this plot, the ccd is set to 300 µm and the lateral charge spread chosen to be $\sigma = 7$ µm, which reflects the fraction of one hit to two hit clusters as observed with the single crystal assembly. The measured charge distribution of 8.23(a) can qualitatively only be reproduced by assuming a charge collection distance of 75 µm and a charge spread of 14 µm. This is shown in fig. 8.23(b).

One possible explanation would be trapped charges at the metal to bulk transition of the electrode metalization. This would result in an reduced electric field inside the bulk which in turn leads to a reduced charge collection and an increased lateral spread of the charge carriers as observed with the module sensor. The metalization of the presented modules is known to be problematic. To exclude this as origin of the observed effects, currently a new diamond module is in production with all processing steps done by IZM in one go.

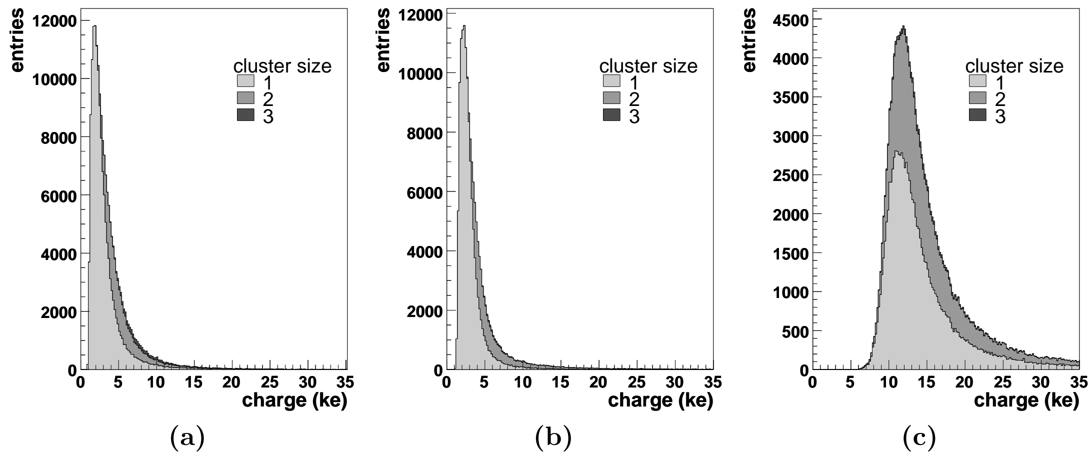

Figure 8.23: (a) Charge distribution observed in the diamond module with an applied bias voltage of 400V. The distribution is cut off at the low side because of the 1500 e readout threshold. (b+c) Charge distributions obtained by Monte Carlo simulation for diamond sensors with a charge collection distance ccd and lateral charge spread σ of (b) $ccd = 75\,\mu\text{m}$, $\sigma = 14\,\mu\text{m}$ and (c) $ccd = 300\,\mu\text{m}$, $\sigma = 7\,\mu\text{m}$.

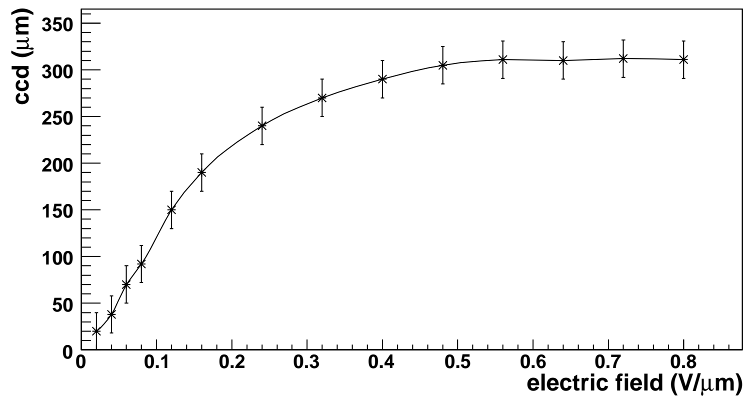

Figure 8.24: Charge collection vs. electrical field dependence of the pCVD diamond material used for the diamond module sensor[59].

9 3D-Silicon Pixel Sensors

3D sensors address the implications of radiation damage by a change of the electrode geometry. Instead of planar electrodes on top and bottom of the bulk, 3D sensors are characterized by cylindrical electrodes perpendicular to the surface and etched into the bulk material. Figure 9.1 illustrates the concept of the new electrode configuration. It has been proposed first by Parker and Kenney in 1997 [60].

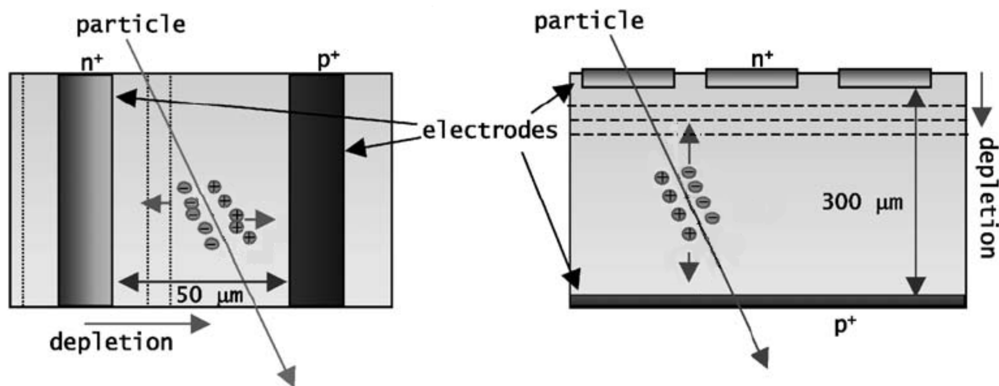

Figure 9.1: A 3D detector (left) compare with a standard planar detector (right). The same charge generated along the trace of a traversing ionizing particle is collected by a 3D detector over a much shorter length. This results in faster signals and a much lower depletion voltage. The dashed lines indicate the growth of the depletion zone with increase in bias voltage [61].

The 3D concept preserves the bulk thickness for charge generation while reducing the electrode spacing. Compared to planar detectors, the benefits regarding radiation damage are a shorter drift length for the charge carriers and a much decreased depletion voltages (see also chapter 4). An additional advantage is the orientation of the electrodes parallel to the particle tracks. For the generated charges this results in equal arrival times while in planar devices the collection of the generated charge is spread in time. 3D devices hence have a faster charge collection.

Beside cylindrical electrode pillars also electrode walls can be fabricated and used to form the edges of a device into an active electrode. 3D active-edge sensors can be fabricated which are sensitive to within a few microns of their physical dimensions. This is different to traditional planar silicon processing, where usually an insensitive “guard ring” structure of several 100 µm is used to control the voltage drop from the pixel potential to the edge [19].

Fabrication: The 3-dimensional structure is obtained by processing the n^+ and p^+ electrodes into the substrate bulk by combining VLSI[1] and MEMS[2] technologies [62]. First the holes and trenches for the electrodes are etched using *deep reacting ion etching* (DIRE). An example is shown in fig. 9.2. This is a repetitive combination of plasma etching and passivating. It allows the etching of truly vertical walled holes with a depth to width ratio of 15:1 and even more. Due to its complexity it is quite costly and with etch rates in the order of several µm/min slow compared to other processing steps. The etched holes are filled with doped silicon of amorphous type using slowly reacting gases, which homogeneously deposit material near the bottom as well as on the top of the etched holes. In the end, the electrodes are connected for readout by metal layers as in a usual semiconductor manufacturing processes.

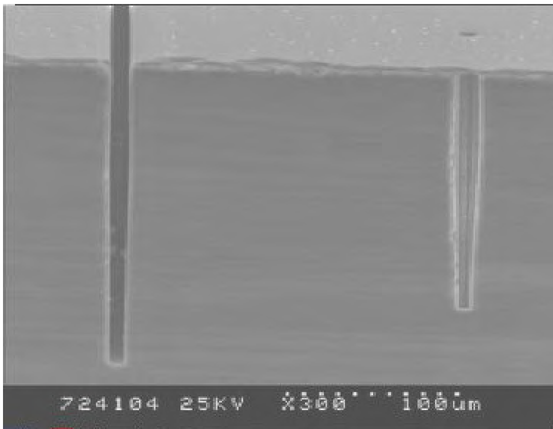

Figure 9.2: Picture of a 3D electrode etching study. The structure seen on the left is a trench for an active edge electrode. The right one is a hole for a cylindrical electrode [62].

3D pixel detectors: To adapt the 3D sensor concept to a conventional pixel layout, a sensor design as shown in fig. 9.3 for the ATLAS pixel geometry of 400 µm × 50 µm has been used. All the p^+-implants are electrically connected with each other and form the biasing electrode, while the n^+-implants form the pixel readout electrodes. To keep the p^+ to n^+ spacing small also in direction of the larger pixel dimension, several readout electrodes are combined in one pixel. The electrode geometry is determined by the desired depletion voltage, the desired maximum charge collection distance and the pixel size, but also by the limits of the fabrication technology.

For the ATLAS pixel geometry three different 3D sensor designs have been realized as shown in fig. 9.4(a-c). They contain either two (2E), three (3E) or four (4E) readout electrodes per pixel cell. This corresponds to n- to p-electrode spacings of 103 µm, 71 µm and 56 µm respectively.

A total of ten wafers, each containing 32x 3E, 6x 4E and 6x 2E sensors for use with a single FE-I3 readout chip, have been produced at the Stanford Nanofabrication Facility. The sensitive bulk thickness and electrode length for the fabricated

[1] Very Large Scale Integration
[2] Micro Electro Mechanical Systems

3D sensors has been measured to be $(208 \pm 5)\,\mu m$ [63]. The bulk material has a resistivity of $12\,k\Omega cm$ and the calculated depletion voltages are 20 V (2E), 8 V (3E) and 5 V (4E) [64].

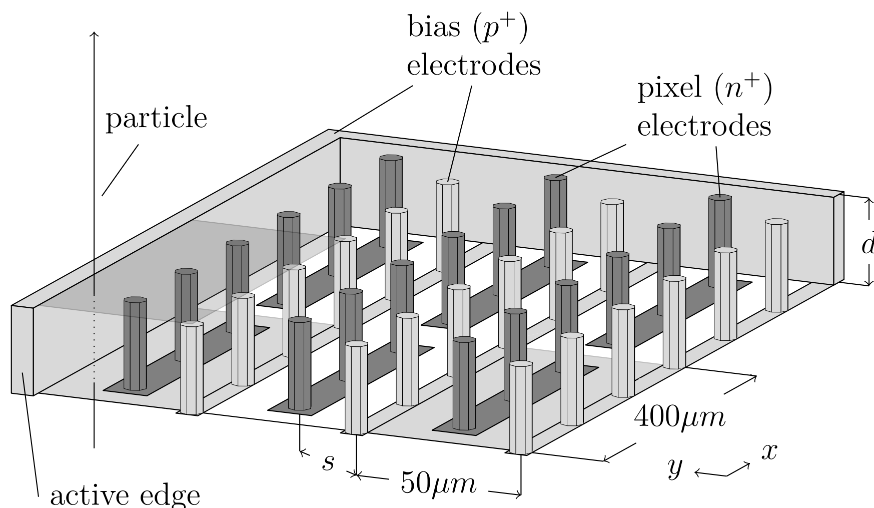

Figure 9.3: Schematic view of a ATLAS three electrode (3E) sensor illustrating the p-, n- and active-edge-electrode arrangement. The electrode spacing s is for the shown 3E structure 71 µm. The fabricated 3D sensors have a bulk thickness d of 208 ± 5 µm.

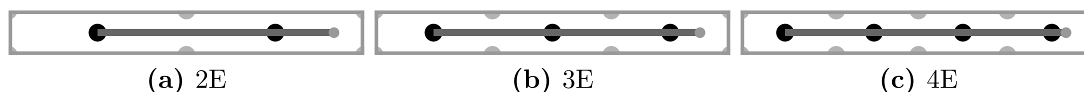

(a) 2E **(b)** 3E **(c)** 4E

Figure 9.4: The three different ATLAS 3D pixel cell layouts with an n- (black) to p-electrode (gray) spacing of 103 µm (2E), 71 µm (3E) and 56 µm (4E). The readout electrodes are linked together by a metal layer and connected via a bump bonded pad to the readout chip (small dot to the right).

9.1 3D single chip assemblies

The first lot of 16x 3E, 5x 4E and 4x 2E sensors bump bonded to a FE-I3 chip have been delivered to Bonn in August 2006. For a full test, each device has to be bonded to a single chip card (fig. 5.8 in chap. 5) to provide the connection to the test system.

The sensors arrived two weeks before the scheduled testbeam period. At the given time scale, only a limited number of devices could be assembled and tested before they had to be distributed between the members of the 3D collaboration. One of the structures (3E-R) was characterized in more detail and tested in an

additional testbeam effort in October 2006. Table 9.1 gives an overview about the available 3D devices.

Device	FE-I3	testbeam	note	working
2E-A	5-15A	2006-08	at CERN	✓
2E-B	4-15B		known bad sensor	×
2E-C	9-14B		at CERN	?
2E-E	9-15A		at CERN	?
4E-A	8-14B		known bad sensor	×
4E-B	8-14B	2006-08	at CERN	✓
4E-C	7-14B		at CERN	?
4E-D	7-14A		at CERN	?
4E-E	6-14B		at CERN	?
3E-A	6-14A		known bad sensor	×
3E-B	5-14B		sensor over current	×
3E-F	5-14A		sensor over current	×
3E-G	4-14B	2006-08	at CERN	✓
3E-J	3-14B		at CERN	?
3E-K	4-14A		at CERN	?
3E-N	10-13B		at CERN	?
3E-O	9-13B		at Bonn	✓
3E-P	9-13A		at Bonn, not assembled	?
3E-R	3-13B	2006-10	at Bonn	✓
3E-S	8-13A		sensor over current	×
3E-I	4-13B		known bad sensor	×
3E-H	7-13A		bump mask missalignment	×
3E-M	6-13B		probably bad sensor	?
3E-L	6-13A		probably bad sensor	?
3E-Q	5-13B		bump mask missalignment	×

Table 9.1: Overview of the flip chiped 3D devices build from the first wafer containing working FE-I3 compatible 3D sensor structures. All used front-end chips origin from wafer AFD524X. As note a short description or the whereabout of the device along the 3D collaboration is given.

Sensor current: To determine the effective bias voltage across the sensor, one has to correct for the bias resistor placed in series with the sensor ($R \approx 11.3\,\mathrm{k\Omega}$) and the input potential of the pixel amplifier (V_{pix}). In the case of the FE-I3 the input potential is related to the analog operating voltage and around 1.5 V. The biasing voltage is by design of the device negative and applied referenced to ground. The voltage across the sensor is then given by

$$-V_{sensor} = -V_{bias} - R \cdot I_{bias} + V_{pix}. \tag{9.1}$$

Figure 9.5 shows the current voltage characteristic of the assembled 3D device for the applied- and corresponding sensor voltage.

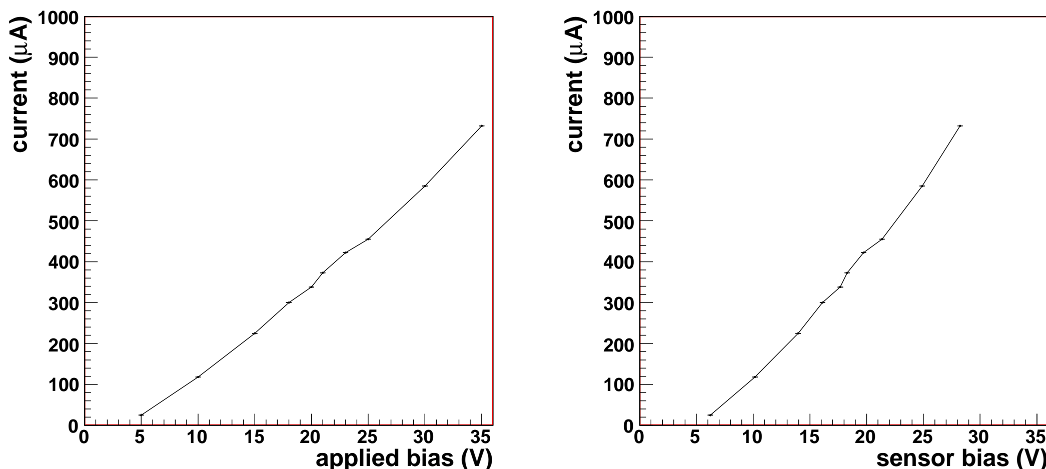

Figure 9.5: IV-characteristic of the 3D-3E-R structure. Applied bias (left) and effective bias across the sensor (right). See text for explanation.

The observed characteristic deviates strongly from the IV-curve expected from a reverse biased diode. First the current is much higher (118 μA at 10 V) and second it shows a more ohmic like behavior ($\sim$ 30 kΩ). This indicates already, that at least one of the 3D electrode pn-junctions shows a fabrication defect which appears above a certain voltage as an ohmic behaving short. The leakage currents can be measured with the means provided by the front-end chip itself. The result is shown in fig. 9.6. Here the few defect pixels can be clearly identified as they draw a leakage current wide outside of the dynamic range of the inbuilt measurement circuit. For several devices this high conducting kind of defects prohibited the depletion of the sensor.

The absolute accuracy of the measurement is very limited due to the implementation of the measurement circuitry in the chip [43]. The error is in the order of the measured value itself. For a usual 3D pixel one measures a mean leakage current of 2.8 nA. For normal ATLAS silicon sensor pixel one obtains for a similar measurement about 1.4 nA [43]. The exact value of the 3D pixel leakage cannot be obtained by this measurement, but by comparison with other measurements in [43] one can estimate it to be in the order of 1 nA.

Threshold and ToT tuning: For operation it was chosen to tune the device to a discriminator threshold of 3000 e (GDAC 16, TrimT 64) and a ToT value of 60 (IF 9, TrimF 16) at an injected charge of 20000 e. The tuning was done with the standard TurboDAQ method at an applied bias voltage of 20 V.

The resulting mean threshold is (3215 ± 210) e and for an injected charge of 20000 e the mean ToT response is (67 ± 3) ToT (fig. 9.7(a+b)). From the threshold

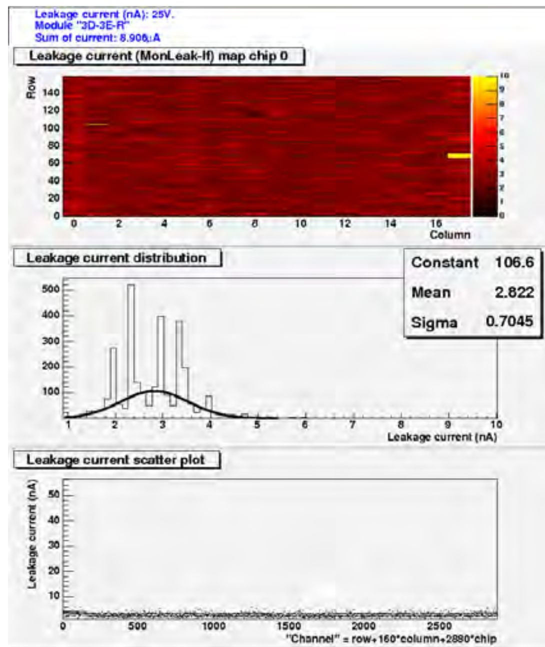

Figure 9.6: Pixel leakage current. The yellow spots in the upper plot are pixels showing a leakage current well above 100 nA. The scale is limited to 10 nA to keep the variations in the other pixels visible. The peaks visible in the leakage current distribution are due to digitization issues.

measurements also the noise of the electronics is determined (chap. 7.2). For a standard pixel cell it is (342 ± 16) e. The pixels on the left and right edges have a slightly different design and an active edge. This increases the capacity of the so called long pixels and the noise is (429 ± 21) e (fig. 9.7(c)).

ToT calibration: The ToT response of each individual pixel was calibrated with the inbuilt C_{high} charge injection. The result for a selected pixel is shown in fig. 9.8(a). The data are fitted with the three parametric ToT calibration function which is used to infer from the ToT response to the charge deposited in the sensor (chap. 7.2). While on average the fit perfectly describes the device response, the charge corresponding to a certain ToT value shows a reasonable spread. For a ToT of 55 the standard deviation of the corresponding charge distribution is about 1800 e at an mean of 20000 e (fig. 9.8(b)). The relative charge resolution is thus about 10%.

The calibration was cross checked with the 59.6 keV and 26.3 keV γ-lines from an ^{241}Am source. The corresponding charge deposits expected are 16500 e and 7300 e. The measured charges of 15500 e and 6700 e (fig. 9.9) indicate that the absolute ToT calibration uncertainty lies between $5 - 9\%$.

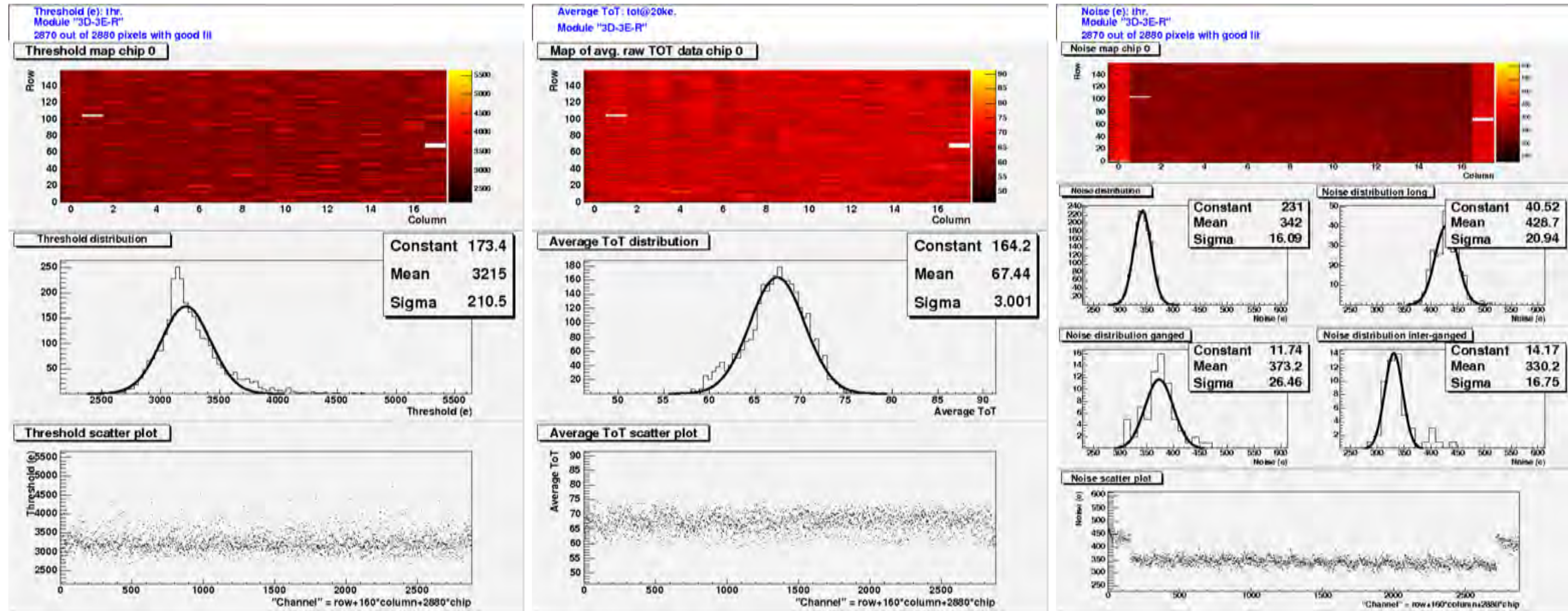

(a) Threshold **(b)** Mean TOT @20 ke **(c)** Noise

Figure 9.7: Threshold, ToT@20 ke and noise for the tuning used during the testbeam measurements.

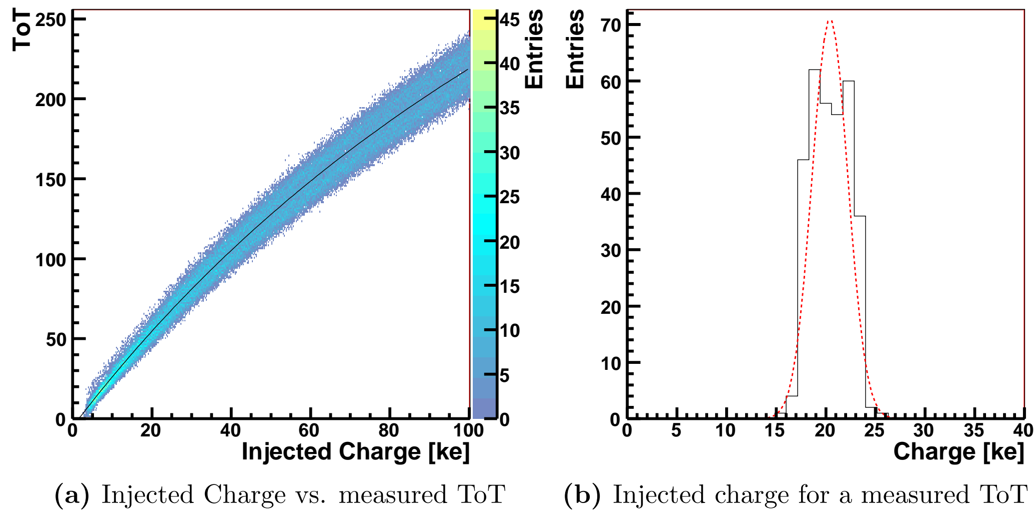

(a) Injected Charge vs. measured ToT **(b)** Injected charge for a measured ToT of 55

Figure 9.8: (a) ToT calibration for a single pixel (Col 8, Row 80). The solid line is fitted by the standard calibration function. (b) Shows the spread of the injecting charges with the same ToT of 55. The fitted Gaussian has a mean of 20400 e and a sigma of 1800 e.

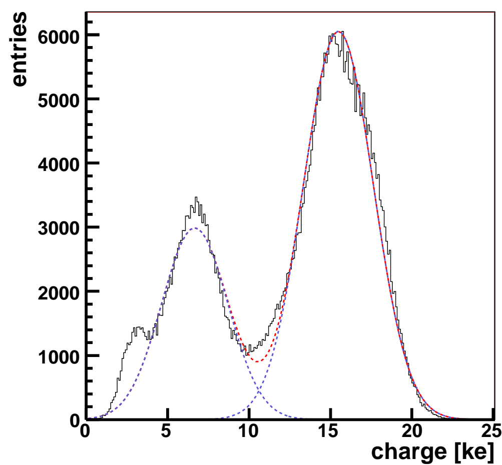

Figure 9.9: Spectrum of an ^{241}Am γ-source measured with the 3D-3E-R device. The charge deposits of the 59.6 keV and 26.3 keV γ-lines are given by the double Gauss fit to 15500 e with a sigma of 2100e and 6700 e with a sigma of 2000 e.

Testbeam measurements

The testbeam measurements focus on the characterization of the three electrode 3D-3E none active edge pixels (fig. 9.4(b)). It was not possible to obtain enough statistics to characterize the active edge pixels. The 3D-3E device has been tested at the CERN SPS in parallel to the scCVD diamond device discussed in the previous chapter (chap. 8). The there made statements about the setup and hit prediction precision are also valid for the 3D-3E-R device discussed here.

Hit prediction: The beam tests have been carried out in a 100 GeV beam of pions at the CERN SPS. To predict the hit position in the 3D device, the testbeam reference system described in chapter 6 has been used. Only tracks from events with a single hit in each telescope plane were selected for the characterization measurements. The precision obtained in the plane of the DUT is better than 5.3 μm. The beam divergence is measured to be less than 0.2 mrad. The uncertainty in the beam incidence angle with respect to the DUT plane is at most 1°.

Charge collection characteristics: The 3D-electrode geometry results in a sideward growth of the depletion zones starting from the p- towards the n-electrodes. The undepleted region of a sensor is located around the n-electrodes and effects only particles passing this region. This implies especially, that the Landau shape of the charge distribution persists. Only the undepleted fraction of the sensor shows a reduced charge collection. Charge collection inefficiencies of the same kind are also expected for the electrodes itself.

In fig. 9.10(a) the measured charge distribution with a Landau type shape is shown as obtained by operating the DUT with a bias voltage of 10 V. The 3D-3E structures are expected to be fully depleted at bias voltages of 8 V. From the fit, the values for peak, mean and FWHM for the fully depleted device are 15800 e, 19200 e and 6800 e, respectively, the latter being mostly due to Landau fluctuations. The population of entries at small charges on the left hand side of fig. 9.10(a) indicate the presence of regions with charge loss. The location of theses regions inside the pixel cell will be studied in more detail in the next section.

Figure 9.10(b) shows the hit efficiency, obtained by integrating all hits and misses over the area of a complete pixel cell, as a function of the applied bias voltage. The efficiency is almost unchanged even down to voltages of ~ 6 V. Data using even lower bias voltage were not taken during this test beam. The slight increase with bias voltage seen in fig. 9.10(b) can be likely be interpret as coming from effects due to the higher electric fields inside the sensor rather than being due to a change in the depletion volume.

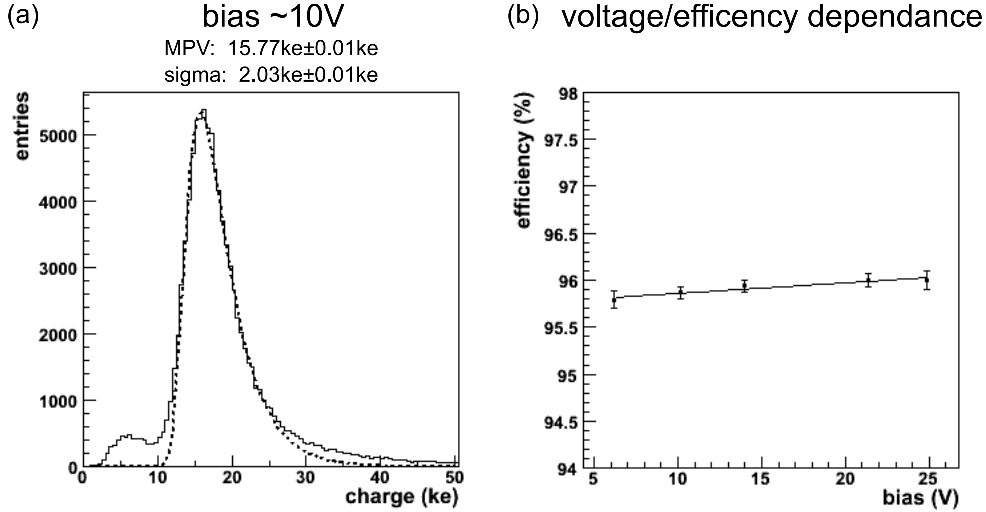

Figure 9.10: (a) Charge distribution of perpendicularly incident particles measured using a bias voltage of 10 V. The solid line is a Landau fit. The quoted errors on mean and sigma are obtained by the fit. The calibration uncertainty is known to be between 5% and 9%. (b) Hit efficiency as a function of applied bias voltage from 6.5 V to 31.5 V.

Hit efficiency: Hits identified in the 3D-device are considered to belong to the predicted hit if the seed position of the cluster is found in the predicted or in a neighboring pixel cell. Otherwise they are counted as misses. In order to investigate the spatial dependence of the hit efficiency, the sensors with three electrodes per pixel have been scanned with the beam to obtain a hit efficiency map. Scans with straight tracks (perpendicular incidence) and with tracks under an inclination angle of about 15° were carried out. For straight tracks, the obtained efficiency map is shown in fig. 9.11(a). Tracks from all illuminated pixels enter the efficiency map. The spot-resolution with which the map is drawn is given by the 2-dimensional bin size, smoothed by a Gaussian, folded with the telescope extrapolation error. All combined this corresponds to $\sim 6.5\,\mu\text{m}$ in both coordinates. The position of the 3D electrodes are clearly identified. The overall efficiency for perpendicularly incident tracks, using a threshold setting of 3000 e and obtained by integrating over the pixel area, corresponds to

$$\epsilon_{0^\circ} = 95.9\% \pm 0.1\% \qquad . \tag{9.2}$$

The respective cluster charge distribution from the two areas corresponding to low (black central dot in fig. 9.11(a) and high (ring between radii of 22 μm and 24 μm) hit efficiency, are shown separately in figs. 9.11(b) and 9.11(c), properly normalized by area. Note that in fig 9.11(b) the misses are placed in the first bin and entries even somewhat below the nominal threshold of 3000 e are possible due to the non-linearity of the ToT calibration at small charges. The charge

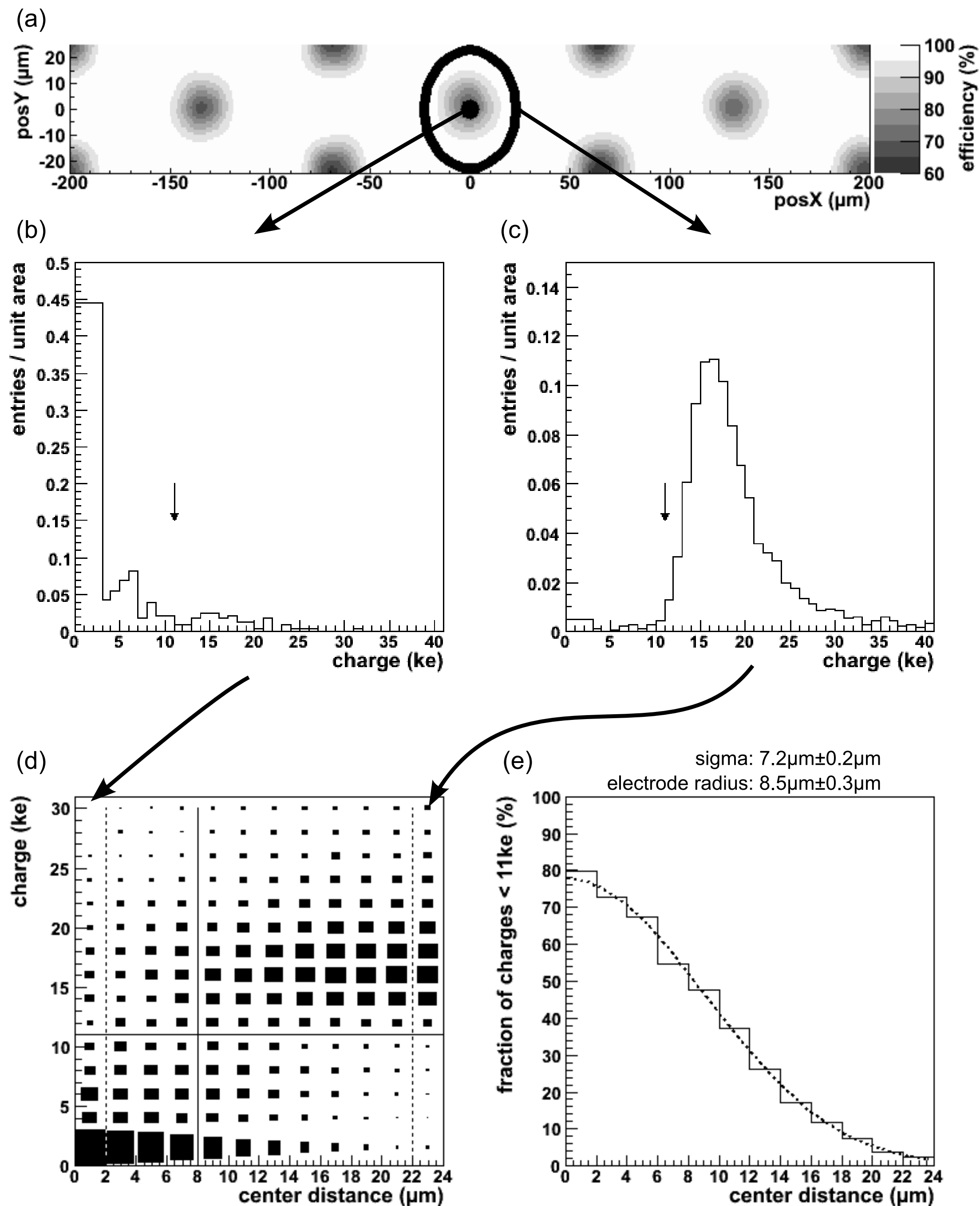

Figure 9.11: (a) Charge collection map over the area of one pixel ($50 \times 400\,\mu m^2$). The areas indicated by the black dot and the ring lead to charge distributions shown in (b) and (c) below, representing areas in and far away from the 3D electrodes, respectively. The arrows in (b) and (c) indicate the chosen separation selection for the two-dimensional histogram in (d) showing charge versus distance from the column center. The lowest and the highest x-bins in (d) correspond to the charge distributions in (b) and (c) as indicated. (e) Relative fraction of entries per area with a charge smaller that 11 ke. The superimposed curve is a fit (see text).

distribution for tracks entering far away from the column center (fig. 9.11(c)) shows the expected Landau shape with the lowest entries at about 10 ke. Charge entries below 11 ke are thus classified as being due to tracks hitting the region of the 3D electrode.

In order to assess the region of reduced efficiency in the 3D-electrodes, in fig. 9.11(d) is plotted in a 2-dimensional histogram the measured charge versus the distance ΔR from the nominal center of an electrode column. The solid lines separate regions above and below the low side of the Landau distribution (arrows in fig. 9.11(b) and 9.11(c), as well as above and below the nominal column etch radius (histogram bin starting at 8 µm). In an ideal world this plot would give a discrete charge output (a horizontal line) as a function of ΔR. This ideal picture in reality is smeared by (i) the track extrapolation resolution of about 5 µm, (ii) the Landau distribution of deposited energy in the sensor, (iii) δ-electrons being mostly emitted at $\sim 90°$ to the tracks and traveling into regions of more/less efficient charge collection, and (iv) the electronics thresholds of ~ 3000 e existing for every pixel. Figure 9.11(d) clearly identifies two regions, one with large collected charge at distances larger than about 8 µm from the electrode center (upper right), and one with small charge at small distances, corresponding to the column region (bottom left). Figure 9.11(e), finally, displays the relative fraction of entries in rings around the electrode with a charge smaller that 11 ke, as a function of the distance from the electrode center. The superimposed curve represents a fit of a flat distribution with electrode radius r folded by a Gaussian. In agreement with a simple simulation one finds a column radius of r = (8.5 ± 0.3) µm, in agreement with the width of the nominal etching radius of 8.5 µm. The Gaussian σ is found to be (7.2 ± 0.2) µm, i.e. wider than the contribution from the telescope resolution (~ 5 µm) alone. Part of this is due to the beam's $\lesssim 1°$ inclination to the DUT plane, resulting in a 4 µm space displacement over the depth, but also indicates that the efficiency inside the column is not a step function. The additional spreading can be assumed to originate from effects like charge diffusion or other mechanisms of signal induction for tracks entering the undepleted column regions.

The mean charge of hits belonging to the region outside of the electrode is about $20 - 25$ ke. Hits assigned to the electrode center, on the contrary, show a mean charge below 5 ke. Thus, with some uncertainty and caution introduced by the existing pixel thresholds of ~ 3 ke, the charge collection efficiency inside the 3D-electrode is estimated to be in the order of at most 25%. If, alternatively, one assumes 0% efficiency inside the electrode and 100% outside, the *effective column radius* is calculated from eq. 9.2 to be 6.5 µm.

In a pixel tracking detector, the pixel modules are usually tilted in the azimuthal direction to optimize charge sharing between neighboring readout cells. For 3D sensors this produces the extra beneficial effect that tracks originating from the interaction point would not run exactly parallel through the center of the 3D electrodes. In fig. 9.12 Landau distributions for perpendicular tracks and for tracks under an inclination angle of 15° are compared. As expected, for inclined tracks in fig. 9.12(b) the entries with small charge on the left of fig. 9.12(a) disappear.

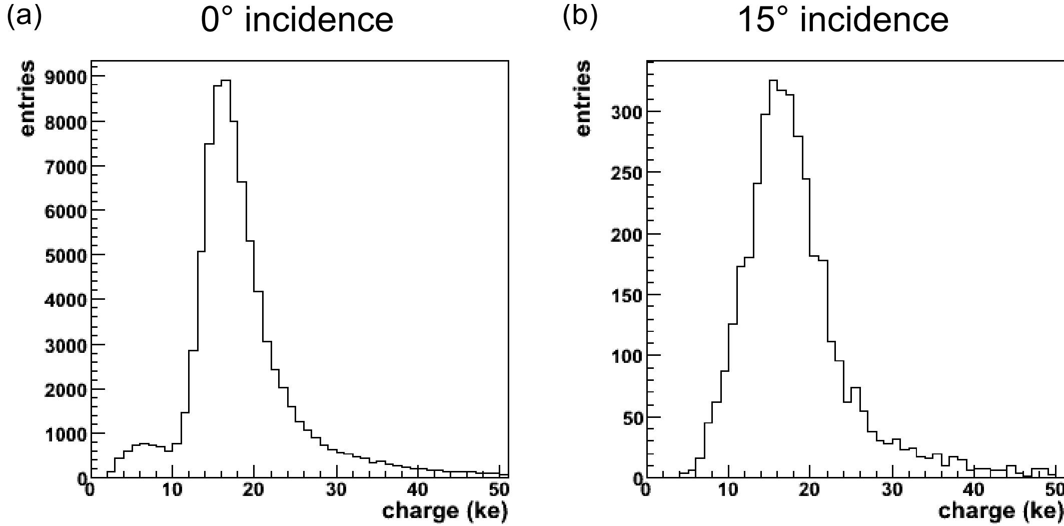

Figure 9.12: Measured distributions of cluster charge for tracks under different inclination angles: (a) 0° angle of incidence, (b) 15° angle of incidence.

The width of the Landau distribution now broadens by about 20% and shows the lowest detected charge at about 5 ke. While this is beneficial for track detection at collider detectors where tracks always impinge the detector under an angle, the Landau broadening with entries as low as 5 ke does not constitute a comfortable distance to the hit detection threshold of 3 ke , in particular when a decrease of the signal charge due to radiation must be expected. The hit efficiency for 15° inclined tracks is measured to be

$$\epsilon_{15^\circ} = 99.9\% \pm 0.1\% \qquad .$$

Spatial resolution: The spatial resolution is obtained by plotting the difference between the track position predicted by the telescope on the plane of the DUT (the 3D pixel sensor) and the reconstructed hit of the DUT device. Figure 9.13 shows this distribution for normal incidence of tracks for both directions of the pixel. X corresponds to the direction of the long pixel side (400 µm), Y corresponds to the short direction (50 µm). For the hit reconstruction first only the digital information is used, i.e. the pixel with the largest signal above threshold collected in a cone around the extrapolated track position is taken as the hit pixel and its center is assumed to be the reconstructed position. The digital resolutions of pixel pitch divided by $\sqrt{12}$ in both directions, i.e. 14.4 µm and 114.5 µm are smeared by a Gaussian spread in the order of 5 µm in y and 6 µm in x, which is attributed to the resolution of the track extrapolation, the detector noise ($\sim$ 380 e) and the charge sharing behavior of the pixel cells. The structure visible especially in fig. 9.13(b), results from position dependent response efficiencies which were subject to the investigations in the above section. The charge sharing in the 3D

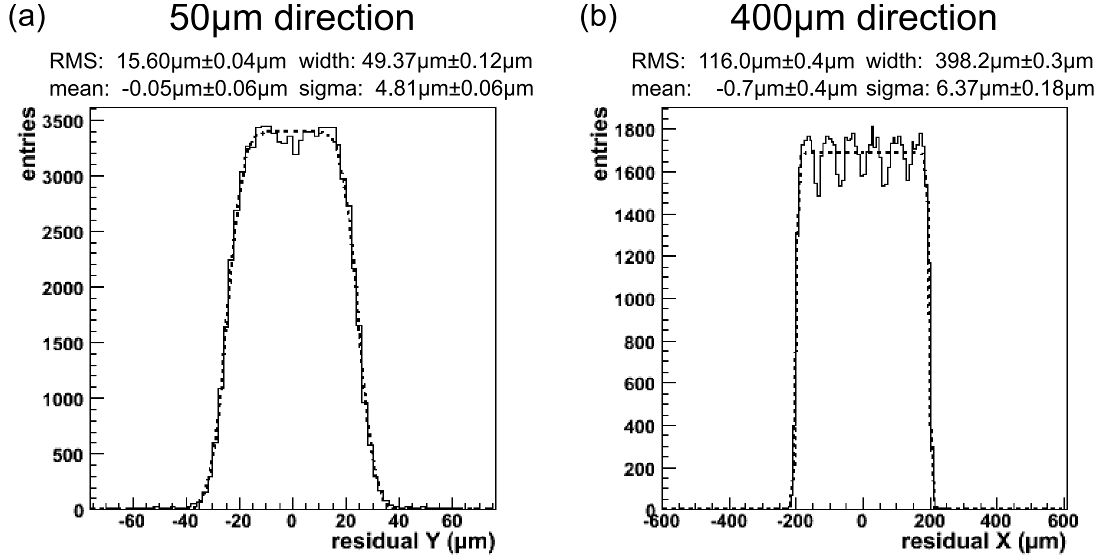

Figure 9.13: Spatial resolution of the 3D pixel device measured with respect to the reference telescope. Only digital information is used, without interpolation using charge sharing. Plotted is the difference between the telescope space point and the measured space point. (a) resolution in the 50 μm direction, (b) resolution in the 400 μm direction. The distributions were fitted with a rectangular function convoluted by an Gaussian distribution. The stated width and sigma and their errors are the values obtained by the fit.

sensor is restricted to a very narrow region of about 4 μm (threshold dependent) at the edge of a pixel. In addition, the charge sharing is not homogeneous along the pixel edge (fig. 9.14(c)). The improvement by using a charge-weighting algorithm (e.g. the so-called η-algorithm [65]) compared to a purely digital readout is therefore limited for normally incident tracks. In real vertex detectors charge sharing is usually purposely introduced by tilting the detectors to improve spatial resolution through charge interpolation [4].

Charge sharing: The sharing of charge between pixel cells as a function of the impact point of the track is studied by plotting the mean value of the cluster size distribution, where a cluster is a number of nearby hits above threshold. Also the fraction of charge appearing in the pixel with the largest charge of the cluster (seed pixel) is of interest. These quantities are displayed as pixel maps in fig. 9.14. The plots show most clearly the overall expected behavior. On average the cluster size increases for inclined tracks. Correspondingly the seed charge fraction decreases, modulated by the position of the 3D electrodes and the resulting influence on the charge collection efficiency.

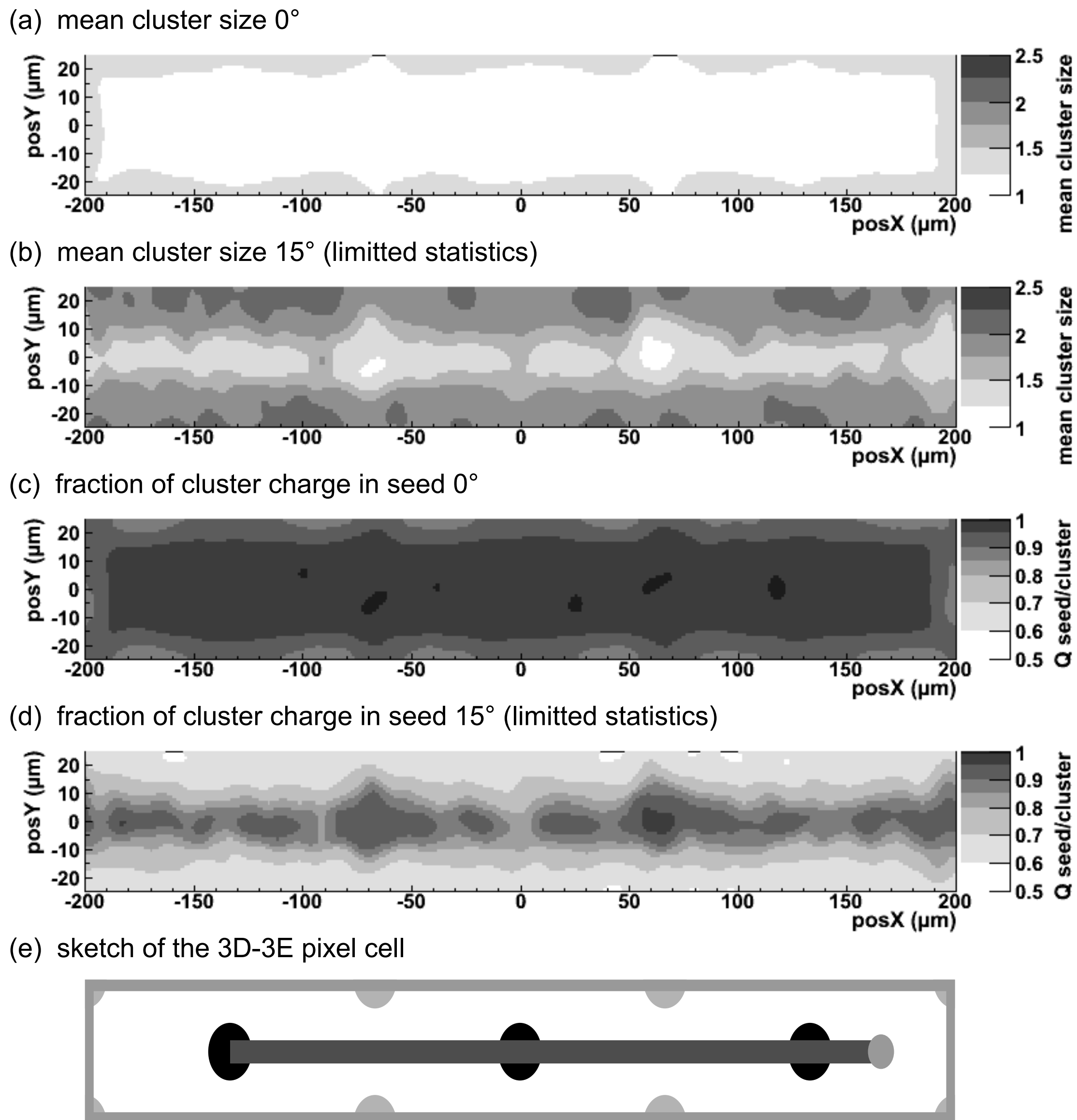

Figure 9.14: Maps of (a),(b) the mean value of the hit-cluster size distribution, and (c),(d) the fraction of the charge of a hit-cluster seen in the pixel with the largest signal (seed pixel). (e) is a sketch of the pixel cell for comparison. The maps are for normally incident tracks (a)+(c) and for inclined tracks (b)+(d), 15° inclination, respectively. Some of the structures visible in (b)+(d) are due to limited statistics.

10 Summary

In future hadron colliders like the Super LHC, the detectors close to the interaction point will have to tolerate particle fluxes larger than $10^{16}\,\mathrm{cm}^{-2}$ 1 MeV neutron equivalent. These radiation levels are beyond the limits of state-of-the-art detector concepts. Research is ongoing to develop detectors which can cope with the requirements for the innermost layer of a potential sLHC tracker upgrade. Currently three sensor concepts are in discussion: planar sensors based on radiation hardened silicon, 3D-silicon sensors utilizing an improved electrode geometry and sensors using a diamond substrate material. For non-irradiated prototypes of the latter two, the characteristics and detector responses to high energy particles have been studied in this thesis.

In the first part of this thesis (chap. 3-5), the theoretical background of charge generation and readout has been compiled and the requirements and implications for radiation tolerant detectors have been discussed. Special care was taken to obtain an accurate prediction of the charge distribution from the transition of high energy particles. In the second part (chap. 6-7) the test environment (lab and testbeam) and the methods used for the characterization of the detectors have been described. The testbeam reference system has been studied in detail to allow for an accurate position prediction within an uncertainty of $4-5\,\mu\mathrm{m}$ in the plane of the device under test. In the last part (chap. 8-9), the characterization measurements of the studied devices have been presented. For the readout electronics the current ATLAS pixel readout chip FE-I3 was used. The devices were assembled using the same bumping and flip-chip technology used during the production of the current ATLAS pixel detector. Characterization measurements were carried out in the laboratory as well as in a high energy particle beam.

Two diamond devices have been studied. The one, a single crystal diamond of about $1\,\mathrm{cm}^2$ was assembled as a single chip device. The first time ever, a scCVD diamond pixel detector has been characterized for high energy particle detection. Full charge collection over the sensor thickness of 395 μm and - for sufficiently large bias voltages of 200 V - no evidence for charge trapping and polarization fields were observed. The measured charge distribution is a narrow Landau distribution as expected from the high density of the material. The observed most probable signal charge is 13100 e with a full width at half maximum of 4000 e. The operation of the device was characterized by low threshold settings (1700 e) and by low noise values (130 e). Single crystal diamond has been found to be free of effects previously observed by trapped charges along the grain boundaries of poly-crystalline material. Especially no lateral polarization fields were observed influencing the space point reconstruction. The spatial resolution obtained by using the digital

hit information is consistent with the expectations. Exploiting charge sharing in the short pixel direction an intrinsic resolution of $8.9 \pm 0.1\,\mu$m was measured.

Further, a diamond module was built to demonstrate the feasibility of a diamond detector in a size reasonable for a real detector design. The sensor was made from poly-crystalline diamond and has a size of about $6 \times 2\,\text{cm}^2$. The device was operated in the laboratory as well as in a 4 GeV electron beam. The experience obtained from the first time realization of a large area diamond sensor has shown deficiencies in the fabrication process. They are addressed during the currently ongoing production of a new pCVD diamond module.

Several single chip devices with different 3D active silicon sensor layouts were assembled and tested in the laboratory. One structure with three 3D electrodes within the area of one pixel ($50 \times 400\,\mu$m) was characterized in detail in a high energy particle beam. For incident tracks normal to the detector surface hit detection efficiencies of $95.9\% \pm 0.1\%$ were obtained. The inefficiencies are proven to be due to the presence of the columnar 3D electrodes. The observed charge distribution outside of the electrode regions corresponds to the expectations for a 208 μm thick silicon detector. The measured most probable charge of the distribution is found to be 15800 e with a full width at half maximum of 6800 e. For inclined tracks of 15° the hit detection efficiency approaches 100% in combination with a broadening of the charge distribution by 20%.

For tracking detectors in a real high energy physics experiment many constraints have to be respected, like the overall cost, cooling, reliability, radiation tolerance, material contribution (radiation length) and complexity, which may even render the actual hit detection performance of the sensors second order. Regarding this, 3D-silicon as well as the diamond sensors have their pros and cons.

The 3D concept addresses the main concerns of irradiated silicon, namely the reduced charge collection and the increase of the depletion voltage. The 3D-electrode structure in addition allows the fabrication of sensors which are sensitive up to their physical dimensions. Driving the electrodes into the bulk, however, influences the homogeneity of the charge collection and introduces charge loss at the position of the electrodes. How far this has consequences for a tracking detector has to be studied in detail.

Single crystal diamond sensors are at present only available in sizes of about $1\,\text{cm}^2$ and not in large quantities. For the large area pCVD diamond sensors the results of the new production have to be awaited before drawing a final conclusion regarding their applicability. Nevertheless, the results obtained with CVD diamond sensors are very promising. The scCVD sensor shows a higher signal to noise performance than the silicon devices and this can even be improved by adjusting the electronics to the low leakage currents and pixel capacitances of diamond sensors. The charge sharing behavior observed allows for a precise hit position reconstruction. In addition the excellent thermal conductivity and the possibility to operate diamond after irradiation without excessive cooling can be advantageously used to reduce the overall radiation length of a full detector system.

The ultimate test for all considered sensor options is, however, the characterization of the devices after irradiation to the expected radiation dose. These tests are currently carried out or are in preparation.

Bibliography

[1] Homepage of the lhc. `http://lhc.web.cern.ch/lhc/`. [Online; accessed Dec-2007].

[2] ATLAS-Collaboration. Detector and physics performance technical design report. *CERN/LHCC/99-14/15*, 1999.

[3] The ATLAS Collaboration, G. Aad, et al. The atlas experiment at the cern large hadron collider. *Journal of Instrumentation*, 3(08):S08003, 2008.

[4] The ATLAS Pixel Collaboration, G. Aad, M. Ackers, F.A. Alberti, M. Aleppo, G. Alimonti, et al. Atlas pixel detector electronics and sensors. *Journal of Instrumentation*, 3(07):P07007, 2008.

[5] Atlas photo archive. `http://atlas.ch/atlas_photos/selected-photos/`. [Online; accessed Dec-2007].

[6] W.M. Yao et al. Review of Particle Physics. *Journal of Physics G*, 33:1+, 2006.

[7] H. Bichsel. Straggling in thin silicon detectors. *Rev. Mod. Phys.*, 60(3):663–699, 1988.

[8] L.D. Landau. *J. Exp. Phys. (USSR)*, 8:201+, 1944.

[9] D.H. Wilkinson. Ionization energy loss by charged particles, part ii: Effects of atomic structure. *Nucl. Inst. and Meth. A*, 401:263–274, 1997.

[10] C. Amsler (Particle Data Group) et al. *Physics Letters B*, 667, 2008.

[11] M.J. Berger, J.H. Hubbell, S.M. Seltzer, J. Chang, J.S. Coursey, R. Sukumar, and D.S. Zucker. Xcom: Photon cross section database (version 1.3). `http://physics.nist.gov/xcom`, 1987. [Online; accessed Jan-2008].

[12] M. Keil. *Pixeldetectoren aus Silizium und CVD-Diamant zum Teilchennachweis in ATLAS bei LHC*. PhD thesis, Bonn University, Nussallee 12, D-53115 Bonn, Germany, Oktober 2001.

[13] S.M. Sze. *Physics of Semiconductors (2nd edition)*. Wiley, 1981.

[14] H. Spieler. *Semiconductor Detector Systems*. Oxford University Press, New York, USA, 2005.

[15] V. Radeka. Low-noise techniques in detectors. *Annual Review of Nuclear and Particle Science*, 38(1):217–277, 1988.

[16] S. Ramo. *Proc. IRE*, 27:584–585, 1939.

[17] T. Rohe. *Planung, Bau und Test des Sensor-Bausteins für einen hybriden Silizium-Pixel-Detektor zum Einsatz unter den extremen Strahlenbelastungen am LHC*. PhD thesis, Ludwig-Maximilian-Universität, Munich, Germany, 1999.

[18] A. Cerdeira and M. Estrada. Analytical expressions for the calculation of pixel detector capacitances. *IEEE Trans. on Nucl. Sc.*, 44:63–66, 1997.

[19] L. Rossi, P. Fischer, T. Rohe, and N. Wermes. *Pixel Detectors: From Fundamentals to Applications*. Springer Verlag, Berlin Heidelberg, Germany, 2006.

[20] elementsix, cvd diamond e-shop catalog. `http://www.e6cvd.com/`. [Online; accessed Sep-2008].

[21] R. C. Alig, S. Bloom, and C. W. Struck. Scattering by ionization and phonon emission in semiconductors. *Phys. Rev. B*, 22(12):5565–5582, Dec 1980.

[22] R. Casanova Alig. Scattering by ionization and phonon emission in semiconductors. ii. monte carlo calculations. *Phys. Rev. B*, 27(2):968–977, Jan 1983.

[23] D. Meier. *Diamond Detectors for Particle Detection and Tracking*. PhD thesis, Universität Heidelberg, Heidelberg Germany, 1999.

[24] T. Lari, A. Oh, N. Wermes, H. Kagan, M. Keil, and W. Trischuk. Characterization and modeling of non-uniform charge collection in cvd diamond pixel detectors. *Nucl. Inst. and Meth. A*, 537:581–593, 2005.

[25] I. Peric and N. Wermes. personal communication, 2007.

[26] D. Bortoletto. `http://wwwhephy.oeaw.ac.at/p3w/cms_tracker/gallery/15.html`. Vertex 2005 [Online; accessed Dec-2007].

[27] S. Baranov, M. Bosman, I. Dawson, V. Hedberg, A. Nisati, and M. Shupe. Estimation of radiation background, impact on detectors, activation and shielding optimization in atlas. *CERN-ATL-GEN-2005-001*, 2005.

[28] H. Sadrozinski. Atlas - slhc upgrade activities. In *11th RD50 Workshop*, 2007.

[29] A. Vasilescu and G. Lindström. Displacement damage in silicon. `http://sesam.desy.de/members/gunnar/Si-dfuncs.html`. [Online; accessed Jan-2008].

[30] E. Burke. Energy dependence of proton-induced displacement damage in silicon. *IEEE Trans. on Nucl. Sc.*, 33:1276–1281, 1986.

[31] G. Lindström et al. Radiation hard silicon detectors developments by the rd48 (rose) collaboration. *Nucl. Inst. and Meth. A*, 466:308–326, 2001.

[32] M. Moll, E. Fretwurst, and G. Lindström. Leakage current of hadron irradiated silicon detectors - material dependence. *Nucl. Inst. and Meth. A*, 425:87–93, 1999.

[33] M. Moll. *Radiation Damage in Silicon Particle Detectors: microscopic defects and macroscopic properties.* PhD thesis, Universität Hamburg, Hamburg, Germany, 1999.

[34] M. Bruzzi and M. Moll. Rd50 status report 2006: Radiation hard semiconductor devices for very high luminosity colliders. *CERN-LHCC-2007-005*, 2007.

[35] M. Bruinsma, P. Burchat, A.J. Edwards, H. Kagan, R. Kass, D. Kirkby, and B.A. Petersen. Cvd diamonds in the babar radiation monitoring system. *Nucl. Phys. B*, 150:164–167, 2006.

[36] RD42 collaboration. Development of diamond tracking detectors for high luminosity experiments at lhc. *CERN-LHCC-2008-005*, 2008.

[37] R. Wunstorf. *Systematische Untersuchungen zur Strahlenresistenz von Silizium Detectoren für die Verwendung in Hochenergiephysik-Experimenten.* PhD thesis, Universität Hamburg, Hamburg, Germany, 1992.

[38] F. Hügging. *Der ATLAS Pixelsensor – Der state-of-the-art Pixelsensor für teilchenphysikalische Anwendungen mit extrem hohen Strahlungsfeldern.* PhD thesis, Technische Universität Dortmund, Dortmund, Germany, 2001.

[39] Rd50 collaboration `http://rd50.web.cern.ch/rd50`.

[40] S.I. Parker, C.J. Kenney, and J. Segal. 3d: A new architecture for solid state radiation detectors. *Nucl. Inst. and Meth. A*, 395:328–343, 1997.

[41] H. Kagan. Diamond radiation detectors may be forever! *Nucl. Inst. and Meth. A*, 546:222–227, 2005.

[42] RD42 collaboration. Development of diamond tracking detectors for high luminosity experiments at lhc. *CERN-LHCC-2006-010*, 2006.

[43] J. Grosse-Knetter. *Vertex Measurement at a Hadron Collider – The ATLAS Pixel Detector.* Habilitation, Universität Bonn, Bonn, Germany, 2008.

[44] J. Wolf. Pbsn60 solder bumping by electroplating. In *Pixel 2000 Conference, Genova, Italy*, 2000.

[45] I. Peric, L. Blanquart, G. Comes, P. Denes, K. Einsweiler, P. Fischer, E. Mandelli, and G. Meddeler. The fei3 readout chip for the atlas pixel detector. *Nucl. Inst. and Meth. A*, 565:178–187, 2006.

[46] J. Weingarten. *System Test and Noise Performance Studies at The ATLAS Pixel Detector*. PhD thesis, Universität Bonn, Bonn, Germany, 2007.

[47] K. Einsweiler. Atlas on-detector electronics architecture. Technical report, Lawrence Berkeley National Laboratory, 2003. internal note.

[48] E. Belau, R. Klanner, G. Lutz, E. Neugebauer, H.J. Seebrunner, A. Wylie, T. Bohringer, L. Hubbeling, P. Weilhammer, J. Kemmer, U. Kotz, and M. Riebsell. Charge collection in silicon strip detectors. *Nucl. Inst. and Meth. A*, 214:253, 1983.

[49] J.J. Velthuis. *Radiation hardness of the ZEUS MVD frontend chip and Strangeness production in ep scattering at HERA*. PhD thesis, NIKHEF, Amsterdam, The Netherlands, April 2003.

[50] V. Blobel and E. Lohrmann. *Statistische und numerische Methoden der Datenanalyse*. Teubner Verlag, Stuttgart Leipzig, Germany, 1998.

[51] J.C. Nash. *Compact Numerical Methods for Computers: Linear Algebra and Function Minimisation*. Taylor & Francis, London, UK, 2 edition, 1 1990.

[52] J. Treis et al. A modular PC based silicon microstrip beam telescope with high speed data acquisition. *Nucl. Instrum. Meth.*, A490:112–123, 2002.

[53] J. Treis. Bonn atlas telescope. Manual, Bonn University, 2002.

[54] J. Treis. *Development an operation of a novel PC-based high speed beam telescope for particle tracking using double sided silicon microstrip detectors*. PhD thesis, Bonn University, Nussallee 12, D-53115 Bonn, Germany, August 2002.

[55] J. Weingarten. *Multi-Chip-Modul-Entwicklung für den ATLAS-Pixeldetector*. PhD thesis, Universität Bonn, Bonn, Germany, 2004.

[56] M. Paterno. Calculating efficiencies and their uncertainties. *D0-Note*, 2861, 1996.

[57] T. Ullrich and Z. Xu. Treatment of errors in efficiency calculations. *arXiv*, 2007.

[58] RD42 collaboration. Development of diamond tracking detectors for high luminosity experiments at lhc. *CERN-LHCC-2002-010*, 2006.

[59] RD42 collaboration. Development of diamond tracking detectors for high luminosity experiments at lhc. *CERN-LHCC-2007-002*, 2007.

[60] S.I. Parker, C.J. Kenney, and J. Segal. 3d – a proposed new architecture for solid-state radiation detectors. *Nucl. Inst. and Meth. A*, 395:328–343, 1997.

[61] C. Da Via, G. Anelli, J. Hasi, P. Jarron, C. Kenney, A. Kok, S. Parker, E. Perozziello, and S.J. Watts. Advances in silicon detectors for particle tracking in extreme radiation environments. *Nucl. Inst. and Meth. A*, 509:86–91, 2001.

[62] C.J. Kenney, S.I. Parker, J. Segal, and C. Storment. Silicon detectors with 3d electrode arrays; fabrication and initial test reults. *IEEE Trans. on Nucl. Sc.*, 48(4):1224–1236, 1999.

[63] C. Da Via. personal communication by e-mail, Jun. 2008.

[64] C. Da Via. Status of 3d active edge silicon sensors. Cern Pixel Meeting, Sep. 2006.

[65] E. Belau et al. *Nucl. Inst. and Meth.*, 565:253–260, 1983.

Acknowledgements

During this thesis I faced the good, the bad as well as the ugly times. Looking back I'm glad I got them all. The good ones I simply enjoyed, the bad ones remembered me to take nothing as granted and the ugly learned me that it is mostly up to oneself to make the best out of each situation. So I want to use this opportunity to express my gratitude to all of the people contributing either way. In fact, this thesis would not be what it is and would not have been possible without the support by all the people I was able to work with during the years. Special thanks go to:

- Prof. Wermes for giving me the chance to work on this thesis and especially for the support and the discussions at the end to get it finally written.
- Prof. Harris Kagan for introducing me to the testbeam analysis, the hours, days and years of fruitful discussions and the remarkable BBQ's at CERN.
- Jaap Velthuis for keeping me motivated during the endless feeling hours of writing analysis code and for taking the pain of proofreading.
- Robert Kohrs and Lars Reuen for the time spend together in and outside the testbeam areas of CERN and DESY to get things done, handled and celebrated.
- Andreas Eyring for sharing the office, the chatting, laughing and the ability to talk plain language and getting the same kind of answers.
- All my present and former collegues at the SiLab who made the work a pleasure and allow me to remember good times. I want to thank all of you and especially Johannes Fink, Manuel Koch, Jens Weingarten and Tobias Stockmanns.
- My girlfriend Sandra Mesenholl for her support during the years of the PhD and the patience in dealing with my work caused erratic mood swings, especially during the last year.
- H. Spieler for pointing me to despair.com

  > "Success is a journey, not a destination. So stop running."
  > despair.com